universität wien

MASTERARBEIT / MASTER'S THESIS

Titel der Masterarbeit / Title of the Master's Thesis

"Towards 6D Coherent Scattering Cooling of Aspherical Nanoparticles"

verfasst von / submitted by

Lorenz Hummer, BSc

angestrebter akademischer Grad / in partial fulfilment of the requirements for the degree of

Master of Science (MSc)

Wien, 2023 / Vienna, 2023

Studienkennzahl lt. Studienblatt / degree programme code as it appears on the student record sheet:	A 066 876
Studienrichtung lt. Studienblatt / degree programme as it appears on the student record sheet:	Masterstudium Physik
Betreut von / Supervisor:	Univ.-Prof. Dr. Markus Arndt

Acknowledgements

I would like to thank everyone who has contributed to this work in a variety of ways, specifically

- **Eva** and **Peter**, my parents, for exciting my curiosity from my early days, for supporting my choices in life and for empowering me when I was questioning them. I would never have made it to this point without your unconditional trust in my abilities and, regardless of where this road might take me, I will forever be thankful for the opportunities you have opened up for me.

- **Evelyn**, my girlfriend, for giving me a new and bright perspective in life and a reason to try my best every day. The prospect of shaping our joint future is the single greatest motivation to continue on my path, may it be ever so rocky. Thank you for the countless times you have lifted me up, for your sincere empathy and for giving me the unequivocal assurance that I will never have to fight on my own.

- **Markus Arndt**, my supervisor, not only for his widely renowned wisdom and his eagerness to share it, but, even more importantly, for his contagious passion, for taking a genuine interest in the well-being of our group, for never turning his back on us when were facing difficulties and for providing valuable and enduring mentorship both on a scientific and a personal level.
  Many years have passed since then, but I still vividly remember the time when you introduced me to the fascinating world of atomic physics in your introductory lecture. That may have been the largest number of PowerPoint slides that I've ever had to study, but in hindsight, they were also the most impactful ones in regard to my professional aspirations.

- **Stephan Troyer**, my lab partner, for diligently proofreading this thesis, for his admirable creativity that is manifest in the design of the experiment, for always keeping a level head when we were struggling, for being patient with me as I was only slowly getting a grasp of the overwhelming multitude of challenges that the daily routine in the lab has to offer and, above all, for being a fantastic teacher who would always take the time to explain or discuss every major and minor issue that came up along the way. I can only express my sincere respect to you and wish you all the best for your future!

- the rest of the nanoparticle team, **Nafia Rahaman**, **Stefan Schrems** and in particular **Florian Fechtel** for their commitment to the pursuit of our common goals, for their tremendous amount of work invested and for the fruitful exchanges of ideas.

- the whole **QNP group** and the **administrative staff** for creating a wonderful work environment, for never refusing to lend a helping hand and for making me feel comfortable from the first day onwards.

- **Uroš Delić** as well as **Ben Stickler** and **Henning Rudolph** for their pioneering work on the experimental and theoretical side, respectively, and for repeatedly providing much appreciated guidance.

Abstract

The present thesis seeks to summarize the theoretical fundamentals of cooling optically levitated nanoparticles in all degrees of freedom, comprising both translational and rotational motion. In preparation to further studies, we also treat interactions with the environment, which give rise to heating and ultimately to decoherence. We explain the experimental steps undertaken so far and describe our current setup as well as envisioned modifications, which we are planning to implement in order to create a versatile and reliable platform for the investigation of rotational quantum phenomena.
A particle that is optically trapped inside a tightly focused laser beam behaves, to a first approximation, like a harmonic oscillator and hence features quantized energy levels. Successful cooling will thus allow us to approach the ground state of energy as a well-defined quantum state. This serves as a prerequisite towards the demonstration of matter-wave interference, which is one of the central predictions of quantum physics, in mesoscopic systems and also holds promise of finding application in ultrasensitive force and torque sensing techniques.
To that end, we are planning to apply the method of coherent scattering cooling, which exploits the optomechanical interaction between the levitated particle and the two polarization modes of an optical resonator. In more concrete terms, a suitable choice of detuning between the wavelength of the laser and the resonance of the cavity causes an enhancement of the inelastic scattering of blue-shifted photons, which carry away mechanical energy of the particle.
As first steps towards our goals, we determine the linewidth of our resonator, which constitutes one of the central parameters governing the cooling efficiency, stabilize the laser frequency with respect to the cavity resonance, detect particles with a diameter of 100 nanometers using both a scattering fiber inside the vacuum chamber and balanced detectors in backscattering, demonstrate loading of the trap in low vacuum using laser-induced acoustic desorption and measure the power spectral density of the particle motion in preparation to parametric feedback cooling and the transition to high vacuum.

Zusammenfassung

In der vorliegenden Arbeit fassen wir die theoretischen Grundlagen der Kühlung optisch levitierter Nanoteilchen in allen Freiheitsgraden sowohl der Translation als auch der Rotation zusammen und gehen dabei in Vorbereitung auf weiterführende Untersuchungen auch auf jene Umwelteinflüsse ein, welche der Dämpfung ihrer Bewegung entgegenwirken bzw. in weiterer Folge zu Dekohärenz führen. Darüber hinaus erklären wir die zu diesem Zweck bereits unternommenen experimentellen Schritte und beschreiben den derzeitigen Aufbau bzw. anvisierte Modifikationen, mit denen wir planen, eine vielseitige und zuverlässige Plattform für die Beobachtung rotationsbezogener Quantenphänomene zu schaffen.

Da sich ein Teilchen in einer von einem stark fokussierten Laserstrahl erzeugten optischen Falle in erster Näherung wie ein harmonischer Oszillator verhält, dessen Energieniveaus quantisiert sind, wird die erfolgreiche Kühlung eine Annäherung an einen wohldefinierten quantenmechanischen Zustand, den energetischen Grundzustand, ermöglichen. Dies soll als erster Schritt dienen, um in Zukunft das Phänomen der Interferenz von Materiewellen als eine der zentralen Vorhersagen der Quantenphysik in mesoskopischen Systemen zu demonstrieren und kann zudem Anwendung in hochsensitiven Kraft- und Drehmomentsensoren finden.

Hierfür planen wir die Methode der kohärenten Streukühlung anzuwenden, welche sich die optomechanische Interaktion zwischen dem levitierten Teilchen und den beiden Polarisationsmoden eines optischen Resonators zunutze macht. Konkret bewirkt eine geeignete Verstimmung der Wellenlänge des Lasers gegenüber der Resonanzfrequenz des Resonators eine Verstärkung der inelastischen Streuung höherenergetischer Photonen, welche die Bewegungsenergie des mechanischen Oszillators aufnehmen und schlussendlich dissipieren.

Als erste Schritte in Hinblick auf unsere Ziele ermitteln wir die Linienbreite unseres Resonators, welche einen für die Kühleffizienz wesentlichen Parameter darstellt, stabilisieren die Frequenz des Lasers mithilfe der Pound-Drever-Hall-Technik in Bezug auf die Resonanz des Resonators, detektieren Teilchen mit einem Durchmesser von 100 Nanometern sowohl mithilfe einer Streufaser im Inneren der Vakuumkammer als auch in Rückstreuung durch symmetrische Detektion, demonstrieren das Laden der Falle in Grobvakuum mittels laser-induzierter akustischer Desorption und messen die spektrale Leistungsdichte der Teilchenbewegung in Vorbereitung auf parametrische Kühlung und den Übergang in den Hochvakuumbereich.

Preface

It is hard not to be mesmerized by quantum physics: Not only has it sparked some of the most famous (and perhaps also most intense) disputes in the physics community and continues to do so – at least when it comes to contemplating the various interpretations of quantum mechanics –, but it has also continuously stood the test of a century-long search for inconsistencies in its theoretical framework. And yet, though it is extremely powerful, it is also subject to a multitude of misconceptions, ranging from minor fallacies that arguably nobody is immune to, all the way to complete misappropriation in the field of mysticism [1]. While it is unfortunate that such a beautiful theory has been put out of context by people who lack even the most basic understanding of it, it is hard to deny that the apparently counterintuitive features quantum systems display – most notably their ability to appear in superposition states and to feature nonlocality – stimulates imagination and may evoke association with supernatural behavior in the layman's mind.

Obviously, it is not true that the quantum world is accessible only through a high-tech physics lab. We witness its implications when we switch on a fluorescent lamp, navigate with GPS or stick a note onto the fridge with a magnet. Despite this fact, it is probably not a fallacious assumption that our lifelong experience of macroscopic objects behaving according to the classical laws of physics has made a decisive contribution to the mystification of what is a mathematically consistent theory (which, of course, does not preclude the existence of possible generalizations). It does hence not come as a surprise that the challenging task of bridging this divide by demonstrating quantum phenomena with mesoscopic states, both in the sense of comprising a "large" number of individual entities and individual objects with "high" mass, has drawn the attention of many research groups in the past decade. Experiments range from matter-wave interferometry with macromolecules [2, 3] to both interferometric [4] and non-interferometric [5–7] tests focusing on localization models as a possible extension to quantum theory that would explain the transition to classical behavior at the macroscopic level.

I, too, used to be to some extent dissatisfied with the ostensible contradiction between what I learned during my classes and what I observed during the (notably short) periods in-between. When Markus gave me the chance to work on an experiment that may at some point contribute towards resolving this imbalance and challenging the common notion of quantum physics pertaining merely to "tiny stuff", while at the same time holding the promise of providing a basis for novel ultrasensitive sensing techniques, I simply listened to my gut feeling and agreed to set off on what turned out to be an exceptionally rewarding journey in a field that had been completely foreign to me...

Contents

Chapter 1

Introduction

Levitated nano- to micrometer-sized particles have emerged as a promising testbed for the investigation of quantum phenomena at mesoscopic scales [8–12]. Above all, they can be extremely well isolated from the environment in the sense that their oscillations inside the confining potential can be preserved for a large number of periods as quantified by the mechanical *quality factor*. This fact constitutes a crucial prerequisite for limiting the adverse impact of decoherence. Experimentally, quality factors of up to 10^{11} have already been achieved [13]. Moreover, nanoparticles exhibit exceptionally low zero-point motion due to their large mass, which implies that the wave function corresponding to the lowest energy state is well-localized in space.
There are several means by which a particle can be kept afloat against gravity in the absence of any nearby surfaces, e.g. by electrical [14], magnetic [15] or even acoustic [16] forces. Which method is the most pertinent in a given setting strongly depends on the properties and size ranges of the particles under investigation, the required degree of control as well as geometric constraints and the type of surrounding medium. Optical levitation is particularly intriguing as it does not demand the presence of any fields other than that of the laser, does not pose any restrictions on charge states and allows for high trapping frequencies. The latter point in particular renders particles trapped by light an ideal platform to uncover the "quantum world" in comparatively massive structures.

As a preliminary step towards that objective, the system needs to be prepared in a well-defined quantum state. The motional ground state is a natural choice to that end, since it arises as the limit of a thermal state when the temperature approaches zero. Even though the interaction with the environment prevents the particle from reaching that state exactly, mean occupation numbers within the quantum regime [17, 18] and even below unity [19, 20] have already been achieved in one or more dimensions and using various techniques. Still, the ro-translational ground state has remained elusive to date.
The final aim of our project is to close this gap and to demonstrate 6D cooling of a levitated nanoparticle. While there remain several experimental challenges that we have yet to overcome, this thesis seeks to provide an overview of the theoretical framework, our current setup, the experimental steps undertaken so far and the modifications that we are planning to implement.

The fact that cooling the motion of nanoparticles is still an ongoing challenge while laser cooling techniques for atoms and molecules, cf. e.g. refs. [21–24], have been well-established for several decades may appear odd at first glance. However, the absence of individually addressable transitions between energy levels in particles comprised of billions of atoms precludes the applicability of the more traditional methods to the systems of our interest.

In a different sense, the (from an atomic point of view) enormous size of our particles is also a virtue as it facilitates the observation of their motion in real time. This fact may be exploited to counteract displacements from the particle's equilibrium position by applying a suitable feedback, either in the form of *parametric feedback* [25] or *cold damping*.

Like the name suggests, the latter approach relies on the exertion of a force that is proportional to the particle's velocity, which can be achieved with the help of electrodes [26] or, more recently, by periodically varying the trap position [27]. Parametric feedback cooling, on the other hand, employs a modulation of the laser power in response to the particle's displacement in such a way that the latter experiences a stronger restoring force as it moves away from the center. An analogous approach may be adopted electrically in combination with an electrodynamic trap [14].
Feedback cooling is eventually limited by the photon recoil imparted to the particle at high laser intensities and low pressures [28]. Low intensities, on the other hand, reduce the detection efficiency, which is especially problematic for smaller particles as the Rayleigh scattering intensity scales with the sixth power of their size.
Parametric feedback cooling will serve us as a pre-cooling method to keep the particle trapped at intermediate pressures. We will briefly discuss the scheme and how we are going to employ it in further detail in sec. 4.1.5.

Cavity-based cooling schemes provide an alternative way of removing energy from a nanomechanical oscillator. One may, for example, resort to a *Sisyphus-type cooling* technique [29]. Remindful of the mythological figure's futile attempts to roll a rock onto a mountaintop, the basic idea behind this method is to make the particle lose more kinetic energy as it "climbs up" the optical potential hill of the standing light wave inside the driven cavity than it gains when it falls back to the minimum.
To see how this works, note that the presence of the dielectric effectively increases the optical path length as long as the particle is located close to an antinode. Taking into account the delayed response by the resonator, a wise choice of the detuning of the driving field with respect to the cavity resonance causes the intracavity intensity and thus the steepness of the optical potential to assume its largest value when the particle moves away from the minimum, while the potential flattens as the particle approaches an antinode. Despite being originally introduced as a novel atom cooling technique [30, 31], it has been noted from the beginning that it is equally well-suited for more complex systems. Indeed, the method has already been applied to control the rotation of levitated nanorods [32]. The main drawback of this technique is the fact that pumping the cavity introduces phase noise from the laser, which, as we will concretize in sec. 3.4.2, limits the attainable minimum occupation number.

We consequently choose the *coherent scattering* approach [33], whereby the cavity is not driven externally, but merely by the light that the dielectric scatters from the trapping beam. In all brevity, an appropriate detuning of the cavity with respect to the trapping field enhances the scattering of *Anti-Stokes photons*, which carry away energy that has previously been stored in the particle's mechanical motion. A detailed account of the theoretical aspects is given in sec. 2.
This method features several attractive advantages associated with the low cavity population [34], most notably the suppression of phase noise and the ability to detect the particle's motion in a clean way without any contribution from non-interacting photons. Coherent scattering has already been successfully applied to cool the translational degrees of freedom (close to) to the ground state [35, 36].
The aforementioned working principle holds under the assumption that one is operating within the *sideband-resolved regime*, i.e. that the cavity decay rate is smaller than the mechanical resonance frequency. While this criterion is met in our experiment as we will see in sec. 4.2.2, it is worth mentioning that it can be hard to attain. In particular, this is the case in combination with small mode volumes as realized in microscopic resonators [37] or when the oscillation frequency is small. While cavity-assisted cooling schemes in the sideband-unresolved regime have been suggested, they require the presence of an auxiliary mechanical mode [38] or the introduction of squeezed light into the cavity [39].

Once their preparation has been demonstrated, ro-translationally cold nanoparticles would open up the path to explore a novel type of quantum interference [10], which is targeted at the orientational degrees of freedom and finds experimental appeal as it avoids the need for a grating and allows for shorter free-fall times. Extending the setup to host multiple particles also seems feasible, paving the way towards preparing and observing entanglement in nanomechanical oscillators [40, 41].

The thesis is organized as follows: In sec. 2, we outline the theoretical framework of the coherent scattering technique in both the translational and orientational degrees of freedom. In sec. 3, we analyze the main sources of decoherence and heating and hint at possible countermeasures. In sec. 4, we present our current setup and the experimental steps undertaken so far. In sec. 5, we summarize a few of the existing proposals on potential applications of levitated nanoparticles, which, in part, rely on the ability to prepare them close to their motional ground state. Finally, we suggest in sec. 6 several modifications and extensions to our setup, which we are planning to implement in the near future.

Chapter 2

Theoretical Aspects

In this section, we provide a concise account of the motion of an optically levitated particle placed inside an empty cavity and explain under which circumstances we expect cooling to take place. We start by reviewing the notion of "motional temperature" of a single-particle system like ours. We then write down its Hamiltonian and the relevant equations of motion. Finally, we solve these equations in Fourier space to obtain an expression for the effective damping that causes the particle to dissipate mechanical energy.
In sec. 2.2, we consider only the center-of-mass degrees of freedom and turn to the more general description including rotations in sec. 2.3. We assume the reader to be familiar with the concepts of electromagnetic field quantization [42] as well as with the basics of cavity physics and Gaussian beams [43].

2.1 The Langevin Equation and the Definition of Motional Temperature

We will first elaborate on what we mean by "cooling" a single particle and how we aim to extract information on its motional state. To that end, we start from the *Langevin equation*, which is the equation of motion for a particle subjected to a fluctuating external force $F_{\text{ext}}(t)$. More specifically, the position z of a classical one-dimensional damped harmonic oscillator with mass m, natural frequency Ω_0 and damping rate γ evolves in time as

$$\ddot{z}(t) + \gamma\dot{z}(t) + \Omega_0^2 z(t) = \frac{F_{\text{ext}}(t)}{m}. \tag{2.1}$$

By Fourier transforming eq. (2.1), we obtain the relation

$$\tilde{z}(\Omega) = \tilde{\chi}(\Omega)\frac{\tilde{F}_{\text{ext}}(\Omega)}{m}, \tag{2.2}$$

where

$$\tilde{\chi}(\Omega) = \frac{1}{\Omega_0^2 - \Omega^2 + i\gamma\Omega} \tag{2.3}$$

is called the *mechanical susceptibility*. Applying the convolution theorem to eq. (2.2) yields a more intuitive interpretation of $\chi(t)$ as the system's response function,

$$z(t) = \frac{1}{m}\int_{-\infty}^{\infty} \mathrm{d}t'\, \chi(t-t')F_{\text{ext}}(t'), \tag{2.4}$$

which determines how the dynamical variable reacts to an impulsive force applied at some earlier time $t' < t$.

We now define the autocorrelation function (ACF) $R_{\xi\xi}$ of an arbitrary (complex) variable $\xi(t)$ as

$$R_{\xi\xi}(\tau) = \lim_{T\to\infty} \frac{1}{T} \int_{-T/2}^{T/2} \mathrm{d}t\, \xi(t)\xi^*(t+\tau). \tag{2.5}$$

and invoke the *Wiener-Khinchin theorem*, which states that the power spectral density (PSD) $S_{\xi\xi}(\Omega)$ of that variable is equal to the Fourier transform of its ACF provided that the process is a wide-sense stationary stochastic one, i.e. a process for which the product $\xi(t)\xi^*(t+\tau)$ depends only on the time shift τ [44]. The PSD quantifies the power contained in a signal per unit frequency, where "power" is to be understood in a broader sense as the strength of a signal regardless of whether it actually corresponds to a physical energy. We are thus left with

$$S_{\xi\xi}(\Omega) = \int_{-\infty}^{\infty} \mathrm{d}\tau\, R_{\xi\xi}(\tau) e^{i\Omega\tau}. \tag{2.6}$$

As can be seen immediately from eq. (2.5), the ACF of the z-coordinate evaluated at $\tau = 0$ is simply the expectation value of z^2. On the other hand, we can convert this to an integral over the PSD by virtue of eq. (2.6),

$$\langle z^2 \rangle = R_{zz}(0) = \frac{1}{2\pi} \int_{-\infty}^{\infty} \mathrm{d}\Omega\, S_{zz}(\Omega). \tag{2.7}$$

The particle being in contact with a thermal reservoir, its energy will fluctuate over time. We may, however, still employ the equipartition theorem to find that the mean squared displacement $\langle z^2 \rangle$ is directly linked to the kinetic temperature T[1] by the relation

$$\frac{1}{2} m\Omega_0^2 \langle z^2 \rangle = \frac{1}{2} k_B T. \tag{2.8}$$

This implies that the temperature of our system is proportional to the area underneath the PSD,

$$T = \frac{m\Omega_0^2}{2\pi k_B} \int_{-\infty}^{\infty} \mathrm{d}\Omega\, S_{zz}(\Omega). \tag{2.9}$$

We will now explain how the stochastic forces, which may correspond to collisions with background gas, recoil of photons or any other type of noise, are connected to $S_{zz}(\Omega)$. We defer a more detailed treatment of the different noise sources to sec. 3.4 and keep the discussion general for now.

Without loss of generality, we can evaluate eq. (2.5) at $t = 0$ to find the autocorrelation function as long as the statistical properties of the respective variable do not change in time. It is then a simple exercise to demonstrate that [45]

$$S_{\xi\xi}(\Omega) = \int_{-\infty}^{\infty} \mathrm{d}\tau\, \langle \xi(t)\xi^*(t+\tau) \rangle_{t=0}\, e^{i\Omega\tau} = \int_{-\infty}^{\infty} \mathrm{d}\Omega'\, \langle \tilde{\xi}(\Omega')\tilde{\xi}^*(-\Omega) \rangle. \tag{2.10}$$

We may then use eq. (2.2) to find that the motional PSD $S_{zz}(\Omega)$ is related to the Fourier transform of the stochastic external force by

$$S_{zz}(\Omega) = \int_{-\infty}^{\infty} \mathrm{d}\Omega'\, \frac{\langle \tilde{F}_{\mathrm{ext}}(\Omega)\tilde{F}_{\mathrm{ext}}(\Omega') \rangle}{m^2} \tilde{\chi}(\Omega)\tilde{\chi}^*(\Omega'), \tag{2.11}$$

where we have taken into account that $z(t)$ is real.

[1] At this point, we should emphasize that we can take eq. (2.8) as a definition for T, which is not related to the particle's internal temperature.

If we are dealing with a white noise process, which is characterized by a flat frequency spectrum, the PSD of the z-coordinate has a Lorentzian shape,

$$S_{zz}(\Omega) \propto \frac{1}{(\Omega_0^2 - \Omega^2)^2 + \Omega^2\gamma^2}. \tag{2.12}$$

The proportionality factor, which we do not need to specify for the time being, is linked to the damping rate γ by virtue of the *fluctuation-dissipation theorem*.
So far, we have assumed all observables to be classical. A quantum treatment reveals [45] that unlike in the previous case $S_{\hat{\xi}\hat{\xi}}(\Omega) \neq S_{\hat{\xi}\hat{\xi}}(-\Omega)$ in general. This has a crucial consequence when computing the probability for a transition to occur between the discrete energy levels of a quantum harmonic oscillator under the influence of an external perturbation. Indeed, the corresponding rate in the upwards direction is proportional to $S_{FF}(-\Omega)$, while the reverse rate is proportional to $S_{FF}(\Omega)$. We refer the reader to ref. [45] for a detailed derivation and state only the result that the temperature of a harmonic oscillator in a steady state (which need not necessarily correspond to the thermal equilibrium) is given by

$$T = \frac{\hbar\Omega}{k_B}\left[\ln\left(\frac{S_{FF}(\Omega)}{S_{FF}(-\Omega)}\right)\right]^{-1}. \tag{2.13}$$

2.2 Coherent Scattering Cooling of the Center-of-Mass Motion

2.2.1 Optomechanical Hamiltonian of an Isotropic Dielectric

Describing the time evolution of any quantum system first requires us to find its Hamiltonian. In our case, it must account for the relevant electric fields, the particle motion and the particle-field interaction. We will now review the individual contributions and note that the total field in our case is just the sum of the intracavity field $\mathbf{E}_{\text{cav}}(\mathbf{r})$ and the strong, coherent trapping field $\mathbf{E}_{\text{tw}}(\mathbf{r})$,

$$\mathbf{E}(\mathbf{r}) = \mathbf{E}_{\text{cav}}(\mathbf{r}) + \mathbf{E}_{\text{tw}}(\mathbf{r}). \tag{2.14}$$

Field Hamiltonian

In accordance with the standard procedure of electromagnetic field quantization [42], we may define operators $\hat{a}$ ($\hat{a}^\dagger$), termed *annihilation* (*creation*) operators, which lower (raise) the photon number associated with a particular mode by one. Given a number state $|n\rangle_{\mathbf{k}s}$ containing a definite number of n photons in the mode of wave vector $\mathbf{k}$ and polarization s, their action may be defined by the equations

$$\hat{a}_{\mathbf{k}s}|n\rangle_{\mathbf{k}s} = \sqrt{n}|n-1\rangle_{\mathbf{k}s} \tag{2.15a}$$
$$\hat{a}^\dagger_{\mathbf{k}s}|n\rangle_{\mathbf{k}s} = \sqrt{n+1}|n+1\rangle_{\mathbf{k}s}. \tag{2.15b}$$

As derived for example in ref. [42], the electric field operator may be written in terms of $\hat{a}$ and $\hat{a}^\dagger$ as

$$\hat{\mathbf{E}}_{\mathbf{k}s}(\mathbf{r},t) = i\sqrt{\frac{\hbar\omega_{\mathbf{k}}}{2\epsilon_0 V_{\text{m}}}}\boldsymbol{\epsilon}_{\mathbf{k}s}\left(\hat{a}_{\mathbf{k}s}f(\mathbf{r})e^{-i\omega_{\mathbf{k}}t} - \text{h.c.}\right), \tag{2.16}$$

where h.c. denotes the Hermitian conjugate, V_{m} is the quantization volume, $\boldsymbol{\epsilon}$ the polarization direction, $\omega_{\mathbf{k}} = c|\mathbf{k}|$ the frequency of the light field and $f(\mathbf{r})$ the spatial mode function, which

must satisfy the Helmholtz equation

$$\left(\Delta + k^2\right) f(\mathbf{r}) = 0 \tag{2.17}$$

under appropriate boundary conditions. We defer a discussion of the specific shape of $f(\mathbf{r})$ to later. For now, we merely note that approximating the trapping field as coherent[2] allows us to treat its field Hamiltonian as constant and neglect it henceforth as it does not affect the dynamics. We are thus left with the intracavity field, the Hamiltonian of which can be shown to read [47]

$$\hat{H}_{\text{field}} = \hbar\omega_{\text{cav}} \left(\hat{a}^\dagger \hat{a} + \frac{1}{2}\right). \tag{2.18}$$

The last term is the *zero-point energy*, which also adds an irrelevant offset and is thus of no further relevance. Eq. (2.18) is valid for a single mode. When more modes are relevant (as will be the case in 6D cooling, see sec. 2.3), the Hamiltonian is just the sum of the respective single-mode expressions.

Particle Hamiltonian

A dielectric particle, which we assume to be linear and (for now) isotropic, acquires a dipole moment $\mathbf{d}$,

$$\mathbf{d} = \alpha \mathbf{E}, \tag{2.19}$$

when subjected to an external electric field. The proportionality constant α is the *polarizability*, which is related to the refractive index n via the Clausius-Mossotti relation [48],

$$\alpha = 3\epsilon_0 V \frac{n^2 - 1}{n^2 + 2}, \tag{2.20}$$

where V is the particle volume. The dipole moment possesses a potential energy inside the external field, which is given by [49]

$$U_{\text{dip}}(\mathbf{r}, t) = -\frac{1}{2}\alpha |\mathbf{E}(\mathbf{r}, t)|^2. \tag{2.21}$$

By virtue of eq. (2.14), the total Hamiltonian features a term pertaining to the trapping field $\propto |\mathbf{E}_{\text{tw}}|^2$, one to account for the cavity mode $\propto |\hat{\mathbf{E}}_{\text{cav}}|^2$ and another one corresponding to the cross term $\propto \hat{\mathbf{E}}_{\text{cav}} \mathbf{E}^*_{\text{tw}} + \hat{\mathbf{E}}^\dagger_{\text{cav}} \mathbf{E}_{\text{tw}}$, where we quantized the cavity field as prescribed by eq. (2.16). The first contribution differs from the latter two (which we will treat later) in that we can neglect the particle's backaction on the trapping field. It hence gives rise to a stationary potential for the particle motion.
We idealize the mode profile of the trapping field as Gaussian[3] with the propagation direction coinciding with the x-axis,

$$f_{\text{tw}}(\mathbf{r}) = \sqrt{\frac{W_{y0} W_{z0}}{W_y(x) W_z(x)}}\, e^{-\frac{(y-y_0)^2}{W_y(x)^2} - \frac{(z-z_0)^2}{W_z(x)^2}}\, e^{i[k(x-x_0) + \phi(\mathbf{r}-\mathbf{r}_0)]}. \tag{2.22}$$

Here, $\mathbf{r}_0 \equiv (x_0, y_0, z_0)$ and $\phi(\mathbf{r})$ is a position-dependent phase,

$$\phi(\mathbf{r}) = \frac{1}{2} kx \left(\frac{y^2}{x^2 + x_{yR}^2} + \frac{z^2}{x^2 + x_{zR}^2}\right) - \frac{1}{2}\arctan\left(\frac{x}{x_{yR}}\right) - \frac{1}{2}\arctan\left(\frac{x}{x_{zR}}\right). \tag{2.23}$$

[2] A compelling argument for why this is justified is presented in ref. [46].
[3] In practice, additional mode cleaning steps may prove necessary for this assumption to hold.

We also allowed for an elliptical beam shape in anticipation of the requirements for simultaneous cooling in all ro-translational degrees of freedom. Here, $W_{y(z)}(x)$ denote the half-axes, $W_{y0(z0)}$ the corresponding waists and $x_{yR(zR)}$ the associated *Rayleigh lengths*

$$x_{yR(zR)} = \frac{\pi W_{y0(z0)}^2}{\lambda}, \tag{2.24}$$

where λ is the wavelength of the beam.
A dielectric particle with a refractive index larger than unity behaves as a high-field seeker inside a light field and is thus attracted to the point of highest intensity, i.e. to the maximum of $|f_{\text{tw}}(\mathbf{r})|^2$ in our case.[4] When the beam is focused tightly enough, the restoring forces along all axes are sufficient to keep the particle trapped. We defer a detailed account of the experimental requirements to realize such an *optical tweezer* to sec. 4.1.2 and for now just assume that the oscillation amplitude is sufficiently small to allow a harmonic approximation of the trapping potential

$$U_{\text{tw}}(\mathbf{r}) = -\frac{1}{2}\alpha|\mathbf{E}_{\text{tw}}(\mathbf{r})|^2. \tag{2.25}$$

In this case, the basic quantization rules for the harmonic oscillator (see e.g. ref. [47]) apply. We denote the associated (phononic) annihilation and creation operators for degree of freedom $j \in \{x, y, z\}$ by $\hat{b}_j$ and $\hat{b}_j^\dagger$, respectively. At a given tweezer beam power P_{tw}, the corresponding trapping frequencies Ω_j read

$$\Omega_x = \frac{2\lambda}{\pi}\sqrt{\frac{\alpha P_{\text{tw}}}{\pi c\epsilon_0 m W_{y0} W_{z0}}\left(\frac{1}{W_{y0}^4} + \frac{1}{W_{z0}^4}\right)} \tag{2.26a}$$

$$\Omega_y = \frac{2}{W_{y0}}\sqrt{\frac{2\alpha P_{\text{tw}}}{\pi c\epsilon_0 m W_{y0} W_{z0}}} \tag{2.26b}$$

$$\Omega_z = \frac{2}{W_{z0}}\sqrt{\frac{2\alpha P_{\text{tw}}}{\pi c\epsilon_0 m W_{y0} W_{z0}}}. \tag{2.26c}$$

The mechanical Hamiltonian is then given by

$$\hat{H}_{\text{mech}} = \hbar \sum_{j\in\{x,y,z\}} \Omega_j \hat{b}_j^\dagger \hat{b}_j. \tag{2.27}$$

Importantly, the components of the position and momentum vectors may be expressed in terms of $\hat{b}_j$ and $\hat{b}_j^\dagger$ as [47]

$$\hat{j} = j_{\text{zpf}}\left(\hat{b}_j^\dagger + \hat{b}_j\right) \tag{2.28}$$

and

$$\hat{p}_j = im\Omega_j j_{\text{zpf}}\left(\hat{b}_j^\dagger - \hat{b}_j\right), \tag{2.29}$$

respectively, with the *zero-point fluctuation*

$$j_{\text{zpf}} = \sqrt{\frac{\hbar}{2m\Omega_j}}. \tag{2.30}$$

[4] As we will clarify in sec. 4.1.2, the equilibrium position of the particle does not coincide exactly with this maximum due to the impact of radiation pressure.

Interaction Hamiltonian

We now turn to the discussion of the interaction with the cavity field. Its mode function $f_{\text{cav}}(\mathbf{r})$ exhibits the same form as eq. (2.22) in the radial directions, but axially the reflection at the cavity mirrors generates a standing light wave with a sinusoidal amplitude pattern. Taking the cavity axis as the z-axis and placing the origin of our coordinate system into the center of the cavity we obtain

$$f_{\text{cav}}(\mathbf{r}) = \frac{w_0}{w(z)} \cos(kz) e^{-\frac{x^2+y^2}{w(z)^2}}, \tag{2.31}$$

where we neglected the phase shift, eq. (2.23), which does not contribute significantly close to the center in view of the cavity waist being much larger than that of the tweezer. The quantization volume that we have encountered in eq. (2.16) is the cavity mode volume V_{cav},

$$V_{\text{cav}} = \int_{-\infty}^{\infty} \mathrm{d}x \int_{-\infty}^{\infty} \mathrm{d}y \int_{-L/2}^{L/2} \mathrm{d}z \, |f_{\text{cav}}(\mathbf{r})|^2 = \frac{\pi}{4} L w_0^2 \tag{2.32}$$

with L denoting the length of the cavity.
For sufficiently small displacements, we may then expand $|f_{\text{cav}}(\mathbf{r})|^2$ in all translational degrees of freedom around the particle position (x_0, y_0, z_0),

$$\begin{aligned} |f_{\text{cav}}(x_0+\Delta x, y_0+\Delta y, z_0+\Delta z)|^2 \approx e^{-2\frac{x_0^2+y_0^2}{w(z_0)^2}} \Bigg[\cos^2(kz_0) \Bigg(1 - \frac{4x_0}{w(z_0)^2} \Delta x \\ - \frac{4y_0}{w(z_0)^2} \Delta y \Bigg) - k \Delta z \sin(2kz_0) \Bigg], \end{aligned} \tag{2.33}$$

where we assumed the beam radius to remain approximately constant and we retained only the terms linear in Δx, Δy and Δz. We then define

$$U_0 = \frac{\alpha \hbar \omega_{\text{cav}}}{4 \epsilon_0 V_{\text{cav}}} \tag{2.34}$$

and insert eq. (2.33) into eq. (2.21), which, upon applying the rotating wave approximation [50] and neglecting the fast-oscillating terms proportional to $\hat{a}\hat{a}$ and $\hat{a}^\dagger \hat{a}^\dagger$, yields the optomechanical interaction terms

$$\hat{H}_{\text{cav}}^{(0)} = -U_0 e^{-2\frac{x_0^2+y_0^2}{w(z_0)^2}} \cos^2(kz_0) \hat{a}^\dagger \hat{a} \tag{2.35a}$$

$$\hat{H}_{\text{cav}}^{(z)} = k U_0 z_{\text{zpf}} e^{-2\frac{x_0^2+y_0^2}{w(z_0)^2}} \sin(2kz_0) \hat{a}^\dagger \hat{a} \left(\hat{b}_z + \hat{b}_z^\dagger \right) \tag{2.35b}$$

$$\hat{H}_{\text{cav}}^{(x)} = U_0 x_{\text{zpf}} e^{-2\frac{x_0^2+y_0^2}{w(z_0)^2}} \frac{4x_0}{w(z_0)^2} \cos^2(kz_0) \hat{a}^\dagger \hat{a} \left(\hat{b}_x + \hat{b}_x^\dagger \right) \tag{2.35c}$$

$$\hat{H}_{\text{cav}}^{(y)} = U_0 y_{\text{zpf}} e^{-2\frac{x_0^2+y_0^2}{w(z_0)^2}} \frac{4y_0}{w(z_0)^2} \cos^2(kz_0) \hat{a}^\dagger \hat{a} \left(\hat{b}_y + \hat{b}_y^\dagger \right). \tag{2.35d}$$

From eq. (2.35), it is evident that the strongest interaction with the x- and y-motion takes place at the antinodes of the standing light wave, while the z-motion couples most strongly half-way between a node and an antinode.
Let us now focus on the interference term proportional to $\hat{\mathbf{E}}_{\text{cav}}^\dagger(\mathbf{r}) \mathbf{E}_{\text{tw}}(\mathbf{r}) + \hat{\mathbf{E}}_{\text{cav}}(\mathbf{r}) \mathbf{E}_{\text{tw}}^*(\mathbf{r})$. We have already said that it is safe to neglect fluctuations in the electric field of the trapping beam and we may hence replace the corresponding operator $\hat{\mathbf{E}}_{\text{tw}}$ by its mean value,

$$\mathbf{E}_{\text{tw}}(\mathbf{r}, t) = \langle \hat{\mathbf{E}}_{\text{tw}}(\mathbf{r}, \mathbf{t}) \rangle = i |\tilde{\alpha}_0| \sqrt{\frac{\hbar \omega_{\text{tw}}}{2 \epsilon_0 V_{\text{tw}}}} \boldsymbol{\epsilon}_{\text{tw}} \left(f_{\text{tw}}(\mathbf{r}) e^{i(\phi - \omega_{\text{tw}} t)} - f_{\text{tw}}^*(\mathbf{r}) e^{-i(\phi - \omega_{\text{tw}} t)} \right), \tag{2.36}$$

where $\tilde{\alpha}_0 = |\tilde{\alpha}_0|e^{i\phi}$ is the (complex) coherent amplitude of the trapping field and the tilde has been added to avoid confusion with the polarizability. The coherent amplitude and the quantization volume of the trapping field V_{tw} are of no further importance and we merely note that E_{tw}, which we define as

$$E_{\text{tw}} = |\tilde{\alpha}_0|\sqrt{\frac{2\hbar\omega_{\text{tw}}}{\epsilon_0 V_{\text{tw}}}}, \tag{2.37}$$

is related to the classical intensity I_{tw} by the familiar relation $I_{\text{tw}} = \frac{1}{2}c\epsilon_0 E_{\text{tw}}^2$.
We can now again make use of the rotating wave approximation and retain only terms oscillating at the difference frequency of the cavity and trapping modes. A suitable choice of the phase leaves us with

$$\hat{\mathbf{E}}_{\text{cav}}(\mathbf{r},t)\mathbf{E}^*_{\text{tw}}(\mathbf{r},t) + \text{h.c.} = \sqrt{\frac{\hbar\omega_{\text{cav}}}{2\epsilon_0 V_{\text{cav}}}} E_{\text{tw}}\,\text{Re}(\boldsymbol{\epsilon}^*_{\text{cav}}\cdot\boldsymbol{\epsilon}_{\text{tw}})\left(\hat{a} f_{\text{cav}}(\mathbf{r}) f^*_{\text{tw}}(\mathbf{r}) e^{-i(\omega_{\text{cav}}-\omega_{\text{tw}})t} + \text{h.c.}\right). \tag{2.38}$$

Another Taylor expansion to first order around $\mathbf{r} = \mathbf{r_0}$ in combination with eq. (2.21) yields the interaction terms

$$\hat{H}^{(0)}_{\text{cav-tw}} = -\frac{1}{2}\alpha\sqrt{\frac{\hbar\omega_{\text{cav}}}{2\epsilon_0 V_{\text{cav}}}} E_{\text{tw}}\,\text{Re}(\boldsymbol{\epsilon}^*_{\text{cav}}\cdot\boldsymbol{\epsilon}_{\text{tw}}) e^{-\frac{x_0^2+y_0^2}{w(z_0)^2}}\cos(kz_0)\left(\hat{a}e^{-i(\omega_{\text{cav}}-\omega_{\text{tw}})t} + \text{h.c.}\right) \tag{2.39a}$$

$$\hat{H}^{(z)}_{\text{cav-tw}} = \frac{1}{2}\alpha\sqrt{\frac{\hbar\omega_{\text{cav}}}{2\epsilon_0 V_{\text{cav}}}} E_{\text{tw}} k z_{\text{zpf}}\,\text{Re}(\boldsymbol{\epsilon}^*_{\text{cav}}\cdot\boldsymbol{\epsilon}_{\text{tw}}) e^{-\frac{x_0^2+y_0^2}{w(z_0)^2}}\sin(kz_0)\left(\hat{a}e^{-i(\omega_{\text{cav}}-\omega_{\text{tw}})t} + \text{h.c.}\right)\left(\hat{b}_z + \hat{b}_z^\dagger\right) \tag{2.39b}$$

$$\begin{aligned}\hat{H}^{(x)}_{\text{cav-tw}} = {} & \frac{1}{2}\alpha\sqrt{\frac{\hbar\omega_{\text{cav}}}{2\epsilon_0 V_{\text{cav}}}} E_{\text{tw}} x_{\text{zpf}}\,\text{Re}(\boldsymbol{\epsilon}^*_{\text{cav}}\cdot\boldsymbol{\epsilon}_{\text{tw}}) e^{-\frac{x_0^2+y_0^2}{w(z_0)^2}}\cos(kz_0) \\ & \cdot\left[\left(\frac{2x_0}{w(z_0)^2} + i\left(\frac{1}{2x_{zR}} + \frac{1}{2x_{yR}} - k\right)\right)\hat{a}e^{-i(\omega_{\text{cav}}-\omega_{\text{tw}})t} + \text{h.c.}\right]\left(\hat{b}_x + \hat{b}_x^\dagger\right)\end{aligned} \tag{2.39c}$$

$$\begin{aligned}\hat{H}^{(y)}_{\text{cav-tw}} = {} & \frac{1}{2}\alpha\sqrt{\frac{\hbar\omega_{\text{cav}}}{2\epsilon_0 V_{\text{cav}}}} E_{\text{tw}} y_{\text{zpf}}\,\text{Re}(\boldsymbol{\epsilon}^*_{\text{cav}}\cdot\boldsymbol{\epsilon}_{\text{tw}}) e^{-\frac{x_0^2+y_0^2}{w(z_0)^2}}\frac{2y_0}{w(z_0)^2}\cos(kz_0) \\ & \cdot\left(\hat{a}e^{-i(\omega_{\text{cav}}-\omega_{\text{tw}})t} + \text{h.c.}\right)\left(\hat{b}_y + \hat{b}_y^\dagger\right).\end{aligned} \tag{2.39d}$$

We have now derived all terms of the optomechanical Hamiltonian for the translational degrees of freedom.

2.2.2 Coherent Scattering into the Cavity Mode

We have already mentioned in sec. 1 that one particularly elegant feature of the coherent scattering technique is the absence of external cavity driving. Still, the dielectric particle scatters some of the light from the trapping field in the direction of the mirrors. We will now investigate how this affects the cavity parameters and the particle-field dynamics.
In view of the fact that our particle is significantly smaller than the wavelength of the incident light, $r/\lambda \lesssim 1/10$ (and the same is true for the modified wavelength inside the medium λ/n [51]), we may employ Rayleigh's theory of scattering.[5] We can then assume the dielectric to behave like an oscillating dipole, which radiates according to the well-known dipole radiation pattern [48]

$$\frac{\mathrm{d}P_{\text{tot}}}{\mathrm{d}\Omega} = \frac{c}{32\pi^2\epsilon_0}k^4 d^2\sin^2\theta, \tag{2.40}$$

[5] If the particle is too large for the Rayleigh approximation to be applicable but its refractive index differs only by a small amount from that of the surrounding medium, the somewhat weaker Rayleigh-Gans criterion may still hold [51].

where θ is the angle between the dipole axis and the direction of observation, $\mathrm{d}\Omega = \sin\theta\,\mathrm{d}\phi\,\mathrm{d}\theta$ denotes the solid angle element and the absolute value of the dipole moment d is related to P_{tw} by

$$d = 2\alpha\sqrt{\frac{P_{\mathrm{tw}}}{\pi c\epsilon_0 W_{y0} W_{z0}}}. \tag{2.41}$$

Integrating eq. (2.40) over the entire solid angle yields the total scattered power

$$P_{\mathrm{tot}} = \frac{c}{12\pi\epsilon_0} k^4 d^2. \tag{2.42}$$

Let us first treat the case of homogeneous spherical particles and defer a discussion of the anisotropic case to sec. 2.3. We may then take the polarizability to be a scalar quantity, which means that the dipole axis coincides with the polarization direction of the incident light wave. According to eq. (2.40), we maximize scattering into the cavity mode by choosing the polarization axis to be orthogonal to the cavity axis ($\theta = \pi/2$).
The scattered light is subsequently reflected many times by the cavity mirrors. This gives rise to constructive interference and thus to a substantial enhancement of the intracavity intensity provided that the modes are matched, i.e. that the spatial profile of the radiated field has a sufficient overlap with the cavity mode as quantified by the overlap integral [34]

$$\eta = \frac{1}{E_{\mathrm{tw}}\sqrt{\frac{\pi w_0^2}{2}}} \frac{\int \mathrm{d}A\, \mathbf{E}^*_{\mathrm{rad}}(\mathbf{r}) \mathbf{E}^{00}_{\mathrm{cav}}(\mathbf{r})}{\sqrt{\int \mathrm{d}A\, |\mathbf{E}^{00}_{\mathrm{cav}}(\mathbf{r})|^2}}. \tag{2.43}$$

In the above equation, $\mathbf{E}_{\mathrm{rad}}$ is the total radiated field [48],

$$\mathbf{E}_{\mathrm{rad}}(\mathbf{r}) = \frac{k^2}{4\pi\epsilon_0} \frac{e^{-ikr}}{r} \alpha \left(\mathbf{n} \times \mathbf{E}_{\mathrm{tw}}(\mathbf{r}_0)\right) \times \mathbf{n}, \tag{2.44}$$

where $\mathbf{n}$ is the direction of observation and $\mathbf{E}^{00}_{\mathrm{cav}}(\mathbf{r})$ is the (Gaussian) TEM_{00}-mode of the cavity, which (just like the scattered spherical wave) does not include the retroreflected part. The overlap is normalized to the incident rather than to the radiated power to account for the finite scattering probability and is evaluated in the plane perpendicular to the cavity axis in the far-field ($z \gg \lambda$). The exact position does not matter, because in this regime the radius of curvature of the scattered spherical wave and the TEM_{00}-mode of the cavity exhibit the same linear scaling with distance. It is shown in ref. [34] that under the assumption of orthogonal polarization we get

$$\eta_{\mathrm{max}} = \frac{k\alpha}{\epsilon_0 \pi w_0^2}. \tag{2.45}$$

Provided that the particle is isotropic, the amplitudes of the fields scattered towards the left and the right mirror are equal and given by [34]

$$E_{\mathrm{mirr}} = i\eta E_{\mathrm{tw}}. \tag{2.46}$$

Denoting by R_1 and R_2 the reflectivities of the mirrors, E_{mirr} reduces by a factor of $\sqrt{R_1 R_2}$ after each round trip. In the following, we will always assume that $R_1 = R_2 \equiv R$.
Considering that the left- and right-travelling fields differ only by a phase of $e^{2ik\Delta z}$ and under the condition that the resonance condition is fulfilled, i.e. $\omega_{\mathrm{cav}} = \omega_{\mathrm{tw}}$, we obtain for the intracavity field amplitude the expression

$$E_{\mathrm{cav}} = E_{\mathrm{mirr}} \sum_{n=0}^{\infty} R^n \left(1 + e^{2ik\Delta z}\right) = E_{\mathrm{mirr}} \frac{1 + e^{2ik\Delta z}}{1 - R} \approx E_{\mathrm{mirr}} \frac{\mathcal{F}}{\pi} \left(1 + e^{2ik\Delta z}\right), \tag{2.47}$$

where

$$\mathcal{F} = \frac{\pi\sqrt{R}}{1-R} \approx \frac{\pi}{1-R}. \tag{2.48}$$

is the cavity's *finesse*.
Let us now examine the case in which the resonance frequency of the cavity and the frequency of the trapping beam differ by the *detuning* $\Delta = \omega_{\text{cav}} - \omega_{\text{tw}}$. After each round trip, the field then acquires a phase of $e^{-i\Delta\tau} = e^{-i\Delta/\Delta\nu_{\text{FSR}}}$, where the cavity's *free spectral range*

$$\Delta\nu_{\text{FSR}} = \frac{c}{2L} \tag{2.49}$$

is the separation between two adjacent resonance frequencies. In that case, we have

$$\begin{aligned} E_{\text{cav}} &= E_{\text{mirr}} \sum_{n=0}^{\infty} \left(Re^{-i\Delta/\Delta\nu_{\text{FSR}}}\right)^n \left(1 + e^{2ik\Delta z}\right) = E_{\text{mirr}} \frac{1 + e^{2ik\Delta z}}{1 - Re^{-i\Delta/\Delta\nu_{\text{FSR}}}} \\ &\approx E_{\text{mirr}} \frac{1 + e^{2ik\Delta z}}{1 - R + i\frac{\Delta}{\Delta\nu_{\text{FSR}}}} = E_{\text{mirr}} \Delta\nu_{\text{FSR}} \frac{1 + e^{2ik\Delta z}}{\frac{\kappa}{2} + i\Delta}, \end{aligned} \tag{2.50}$$

where the approximation is justified as long as $\Delta \ll \Delta\nu_{\text{FSR}}$ and $R \approx 1$. We have also introduced the cavity decay rate

$$\kappa = 2\pi \frac{\Delta\nu_{\text{FSR}}}{\mathcal{F}}. \tag{2.51}$$

The intracavity power consequently reads

$$P_{\text{cav}} = 4P_{\text{mirr}} \Delta\nu_{\text{FSR}}^2 \frac{\cos^2(k\Delta z)}{\left(\frac{\kappa}{2}\right)^2 + \Delta^2}. \tag{2.52}$$

The above equation is not yet entirely appropriate to describe our system as it does not account for the scattering of the intracavity field by the nanoparticle or the modification of the detuning that its presence stipulates. The latter appears in the equation of motion for the mode operator, which we discuss in the subsequent chapter. The intracavity scattering, on the other hand, yields an additional contribution κ_{scatt} to the "bare" decay rate that we defined in eq. (2.51).
While we did not consider the coupling to the free-space modes in the Hamiltonian, we may still find the latter correction heuristically noting that a photon travelling back and forth between the cavity mirrors encounters the scattering center at a frequency of twice the free spectral range and that the scattering probability is simply the fraction of the incident power that is scattered into free space. We then get [34]

$$\kappa_{\text{scatt}} = 2\pi \cdot \frac{4}{3} \Delta\nu_{\text{FSR}} |\eta|^2 k^2 w_0^2 |f_{\text{cav}}(\mathbf{r})|^2 \tag{2.53}$$

and the effective decay rate is given by

$$\kappa_{\text{eff}} = \kappa + \kappa_{\text{scatt}}. \tag{2.54}$$

2.2.3 Translational Equations of Motion and Cooling

We are now ready to discuss the exact mechanism by which coherent scattering of tweezer light into the empty cavity mode is capable of dampening the motion of a nanomechanical oscillator. We will give a brief conceptual outline before working out the mathematical foundations.

While an optical cavity in principle permits a countably infinite number of resonance frequencies, their comparably large separation $\Delta\nu_{\text{FSR}} \gg \Delta, \kappa$ allows us to focus on a single mode and neglect

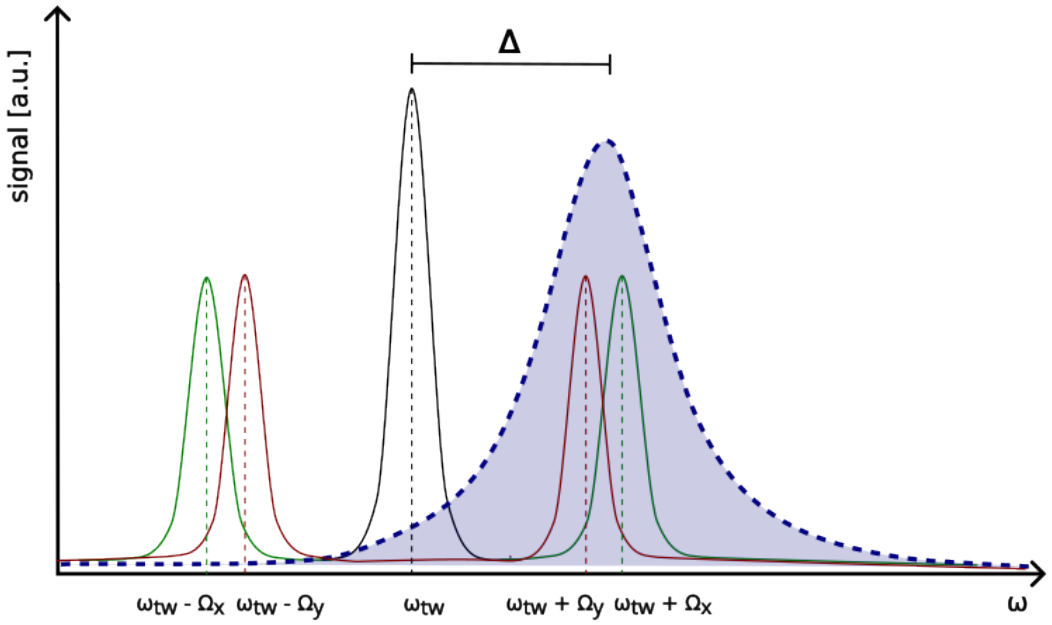

Figure 2.1: Conditions required for coherent scattering cooling as explained in the main text. When the detuning Δ between the frequency of the trapping laser ω_{tw} and the cavity resonance is chosen appropriately, the transfer function of the latter (shaded in blue) comprises all frequency peaks, thus enhancing the scattering of Anti-Stokes photons and leading to cooling in all degrees of freedom. Here, only two peaks are displayed corresponding to the motion along y (red) and along x (green) for the sake of clarity.

all the others. The number of possible states of the light field in our frequency range of interest is hence constant, but the *density* of states follows a Lorentzian curve, which is peaked at the resonance frequency and has a width that corresponds to the decay rate.
According to Fermi's Golden Rule, the transition probability is proportional to exactly this density of (final) states. A transfer function that is sharply peaked at a specific frequency may thus significantly enhance the probability of energy being transferred from the mechanical into the optical mode. This is analogous to the Purcell effect [52], which originally refers to the enhancement or suppression of spontaneous emission by an atom inside an optical resonator, but is straightforwardly generalized to scattering of light by a mesoscopic particle [53].
In order to observe a cooling effect, the scattering of photons that are more energetic than those of the incident field must be enhanced. In this way, mechanical energy is carried away and eventually dissipated. We thus require blue detuning of the cavity, i.e. $\Delta > 0$, and operation within the *sideband-resolved* regime, where $\kappa < \Omega_j$. This mechanism avoids the need of addressing individual transitions as is the case in conventional laser cooling. The above conditions are illustrated in fig. 2.1.
Ideally, the detuning should be exactly equal to the mechanical frequency. However, since the trapping frequencies pertaining to the various degrees of freedom differ, multidimensional cooling requires a certain compromise to be made. This is also true regarding the position of the particle inside the cavity mode, since – as we have seen in sec. 2.2.1 – the optomechanical couplings along the different axes attain their maximum at distinct phases inside the standing light wave.

For the sake of conciseness, we focus on the motion along the z-axis in the following quantitative treatment i.e. we set $\Delta x = \Delta y = 0$, and defer a more general discussion to sec. 2.3. In addition,

we place the particle onto the cavity axis such that $x_0 = y_0 = 0$. Let us also define the constants

$$g_0 = k z_{\text{zpf}} \frac{U_0}{\hbar} \tag{2.55}$$

and

$$E_{\text{d}} = \frac{\alpha}{2\hbar}\sqrt{\frac{\hbar\omega_{\text{cav}}}{2\epsilon_0 V_{\text{cav}}}} E_{\text{tw}}. \tag{2.56}$$

We then transform the optomechanical Hamiltonian,

$$\hat{H} = \hat{H}_{\text{field}} + \hat{H}_{\text{mech}} + \hat{H}_{\text{cav}} + \hat{H}_{\text{cav-tw}}, \tag{2.57}$$

where the individual contributions have been, respectively, defined in eqs. (2.18), (2.27), (2.35) and (2.39), to a frame of reference rotating at the frequency of the trapping beam ω_{tw}. This is accomplished by the unitary transformation $\hat{U} = e^{-i\omega_{\text{tw}}\hat{a}^\dagger\hat{a}t}$. The new Hamiltonian is given by

$$\begin{aligned}\hat{H}' = \hat{U}^\dagger\hat{H}\hat{U} - i\hbar\hat{U}^\dagger\dot{\hat{U}} = \hbar\Bigg[\Delta - \frac{U_0}{\hbar}\cos^2(kz_0) + g_0\sin(2kz_0)\left(\hat{b}_z + \hat{b}_z^\dagger\right)\Bigg]\hat{a}^\dagger\hat{a} \\ + \hbar\Omega_z\hat{b}_z^\dagger\hat{b}_z - \hbar E_{\text{d}}\,\text{Re}(\boldsymbol{\epsilon}_{\text{cav}}^*\cdot\boldsymbol{\epsilon}_{\text{tw}})\Bigg[\cos(kz_0) \\ - kz_{\text{zpf}}\sin(kz_0)\left(\hat{b}_z + \hat{b}_z^\dagger\right)\Bigg]\left(\hat{a}e^{-i\omega_{\text{cav}}t} + \hat{a}^\dagger e^{i\omega_{\text{cav}}t}\right).\end{aligned} \tag{2.58}$$

As one can infer from eq. (2.58), g_0 quantifies the coupling between the cavity field and the mechanical mode, while E_{d} is to be interpreted as the rate at which coherent scattering drives the cavity.

The latter process displaces the quantum state of the cavity field in phase space. Equivalently, we may leave the state invariant and instead transform the mode operator according to $\hat{a} \to \hat{a} + \tilde{\alpha}$ [34], which is accomplished by the unitary transformation $\hat{D}^\dagger(\tilde{\alpha})\hat{a}\hat{D}(\tilde{\alpha})$, where $\hat{D}(\tilde{\alpha}) = e^{\tilde{\alpha}\hat{a}^\dagger - \tilde{\alpha}^*\hat{a}}$. We may hence expand

$$\hat{a}^\dagger\hat{a} \mapsto \left(\hat{a}^\dagger + \tilde{\alpha}^*\right)\left(\hat{a} + \tilde{\alpha}\right) = \hat{a}^\dagger\hat{a} + \hat{a}^\dagger\tilde{\alpha} + \hat{a}\tilde{\alpha}^* + |\tilde{\alpha}|^2. \tag{2.59}$$

Using eqs. (2.45), (2.46), (2.50) and (2.56), it is a simple exercise to show that the amplitude of the coherently driven intracavity field is given by the expression

$$\tilde{\alpha} = \frac{iE_{\text{d}}}{\frac{\kappa}{2} + i\Delta}e^{ik\Delta z}\,\text{Re}(\boldsymbol{\epsilon}_{\text{cav}}^*\cdot\boldsymbol{\epsilon}_{\text{tw}})\cos(k\Delta z) \approx \frac{iE_{\text{d}}}{\frac{\kappa}{2} + i\Delta}e^{ikz_0}\,\text{Re}(\boldsymbol{\epsilon}_{\text{cav}}^*\cdot\boldsymbol{\epsilon}_{\text{tw}})\cos(kz_0). \tag{2.60}$$

The modulus square of eq. (2.60) has an intuitive interpretation as the mean number of photons $\langle n\rangle_{\text{p}}$ in the coherent field,

$$|\tilde{\alpha}|^2 = \langle n\rangle_{\text{p}} = \frac{E_{\text{d}}^2}{\left(\frac{\kappa}{2}\right)^2 + \Delta^2}\left[\text{Re}(\boldsymbol{\epsilon}_{\text{cav}}^*\cdot\boldsymbol{\epsilon}_{\text{tw}})\right]^2\cos^2(kz_0). \tag{2.61}$$

Upon incorporation of the coherent drive, the (final) optomechanical Hamiltonian reads

$$\begin{aligned}\hat{H}_{\text{opt}} = \hbar &\left[\Delta - \frac{U_0}{\hbar}\cos^2(kz_0) + g_0\sin(2kz_0)\left(\hat{b}_z + \hat{b}_z^\dagger\right)\right]\left(\hat{a}^\dagger\hat{a} + \hat{a}^\dagger\tilde{\alpha} + \hat{a}\tilde{\alpha}^*\right) + \hbar\Omega_z\hat{b}_z^\dagger\hat{b}_z \\ &+ \hbar g_0\sin(2kz_0)|\tilde{\alpha}|^2\left(\hat{b}_z + \hat{b}_z^\dagger\right) - \hbar E_\mathrm{d}\,\mathrm{Re}(\boldsymbol{\epsilon}_{\text{cav}}^*\cdot\boldsymbol{\epsilon}_{\text{tw}})\cos(kz_0)\Big[(\hat{a}+\tilde{\alpha})\,e^{-i\omega_{\text{cav}}t} \\ &+ \left(\hat{a}^\dagger + \tilde{\alpha}^*\right)e^{i\omega_{\text{cav}}t}\Big] + \hbar E_\mathrm{d}kz_{\text{zpf}}\,\mathrm{Re}(\boldsymbol{\epsilon}_{\text{cav}}^*\cdot\boldsymbol{\epsilon}_{\text{tw}})\sin(kz_0)\Big[(\hat{a}+\tilde{\alpha})\,e^{-i\omega_{\text{cav}}t} \\ &+ \left(\hat{a}^\dagger + \tilde{\alpha}^*\right)e^{i\omega_{\text{cav}}t}\Big]\left(\hat{b}_z + \hat{b}_z^\dagger\right),\end{aligned} \tag{2.62}$$

where we have once again discarded irrelevant constant terms.

Now that we have written down $\hat{H}_{\text{opt}}$, we can apply Heisenberg's equation of motion, which for an arbitrary, not explicitly time-dependent operator $\hat{A}$ reads [47]

$$\frac{\mathrm{d}\hat{A}}{\mathrm{d}t} = -\frac{i}{\hbar}\left[\hat{A}, \hat{H}_{\text{opt}}\right]. \tag{2.63}$$

Evaluating eq. (2.63) at $t = 0$ and using the commutation relations

$$\left[\hat{a}_i, \hat{a}_j^\dagger\right] = \left[\hat{b}_i, \hat{b}_j^\dagger\right] = \delta_{ij} \tag{2.64a}$$

$$\left[\hat{a}_i, \hat{b}_j\right] = \left[\hat{a}_i^\dagger, \hat{b}_j\right] = 0, \tag{2.64b}$$

we find for the transformed mode operator and the position operator

$$\begin{aligned}\dot{\hat{a}} =& -i\left[\Delta - \frac{U_0}{\hbar}\cos^2(kz_0) + g_0\sin(2kz_0)\left(\hat{b}_z + \hat{b}_z^\dagger\right)\right]\hat{a} \\ &- iE_\mathrm{d}kz_{\text{zpf}}\,\mathrm{Re}(\boldsymbol{\epsilon}_{\text{cav}}^*\cdot\boldsymbol{\epsilon}_{\text{tw}})\sin(kz_0)\left(\hat{b}_z + \hat{b}_z^\dagger\right) - ig_0\tilde{\alpha}\sin(2kz_0)\left(\hat{b}_z + \hat{b}_z^\dagger\right) - \frac{\kappa_{\text{eff}}}{2}\hat{a} \qquad (2.65a) \\ =& -\left(i\Delta_{\text{eff}} + \frac{\kappa_{\text{eff}}}{2}\right)\hat{a} - i\left[E_\mathrm{d}k\,\mathrm{Re}(\boldsymbol{\epsilon}_{\text{cav}}^*\cdot\boldsymbol{\epsilon}_{\text{tw}})\sin(kz_0) + \frac{g_0}{z_{\text{zpf}}}\tilde{\alpha}\sin(2kz_0)\right]\hat{z} \\ \dot{\hat{z}} =& \frac{\hat{p}_z}{m}, \qquad (2.65b)\end{aligned}$$

where we have artificially added the decay term.[6] From eq. (2.65a), we can also identify the effective detuning

$$\Delta_{\text{eff}} = \Delta - \frac{U_0}{\hbar}\cos^2(kz_0) + \frac{g_0}{z_{\text{zpf}}}\sin(2kz_0)\hat{z} \approx \Delta - \frac{U_0}{\hbar}\cos^2(kz_0). \tag{2.66}$$

The last approximation accounts for the fact that the mean displacement is much smaller than the wavelength, which means that $g_0 z/z_{\text{zpf}} \ll U_0/\hbar$, cf. eq. (2.55). In combination with eqs. (2.28)

[6] A rigorous derivation based on the coupling of the system with an external heat bath is presented in ref. [54].

and (2.29), eq. (2.65) yields the equation of motion for the z-coordinate,

$$\begin{aligned}\ddot{\hat{z}} =& -\Gamma\dot{\hat{z}} - \Omega_z^2\hat{z} - \hbar\frac{E_\mathrm{d}k}{m}\,\mathrm{Re}(\boldsymbol{\epsilon}_\mathrm{cav}^*\cdot\boldsymbol{\epsilon}_\mathrm{tw})\sin(kz_0)\left(\hat{a}^\dagger+\tilde{\alpha}+\hat{a}+\tilde{\alpha}^*\right)\\ &-\hbar\frac{g_0}{mz_\mathrm{zpf}}\sin(2kz_0)\left(\hat{a}^\dagger\hat{a}+\tilde{\alpha}\hat{a}^\dagger+\tilde{\alpha}^*\hat{a}+|\tilde{\alpha}|^2\right)+\frac{F_\mathrm{ext}(t)}{m}\\ \approx& -\Gamma\dot{\hat{z}} - \Omega_z^2\hat{z} - \hbar\frac{E_\mathrm{d}k}{m}\,\mathrm{Re}(\boldsymbol{\epsilon}_\mathrm{cav}^*\cdot\boldsymbol{\epsilon}_\mathrm{tw})\sin(kz_0)\left(\hat{a}^\dagger+\hat{a}\right)\\ &-\hbar\frac{g_0}{mz_\mathrm{zpf}}\sin(2kz_0)\left(\tilde{\alpha}\hat{a}^\dagger+\tilde{\alpha}^*\hat{a}\right)\ -2\hbar\frac{E_\mathrm{d}k}{m}\,\mathrm{Re}(\boldsymbol{\epsilon}_\mathrm{cav}^*\cdot\boldsymbol{\epsilon}_\mathrm{tw})\mathrm{Re}(\tilde{\alpha})\sin(kz_0)\\ &-\hbar\frac{g_0}{mz_\mathrm{zpf}}|\tilde{\alpha}|^2\sin(2kz_0)+\frac{F_\mathrm{ext}(t)}{m},\end{aligned} \tag{2.67}$$

which features a mechanical damping Γ to account for the effect of collisions with background gas and an associated fluctuating force $F_\mathrm{ext}(t)$ as explained in sec. 2.1. Eq. (2.67) reveals that there are two distinct types of coupling: one that is proportional to the square root of the photon number inside the cavity, referred to as *dispersive* coupling, and one that depends only on the drive rate E_d. Interestingly, those two couplings exhibit a vastly different spatial variation. The latter is maximal at a node of the cavity mode, where the intracavity intensity vanishes.
While both types of coupling can give rise to cooling as we will demonstrate shortly, an unpopulated cavity allows us to benefit from the complete elimination of phase noise. Still, we need to estimate the maximal coupling that we can attain. We restrict ourselves to the resolved-sideband limit, where $\kappa \ll \Omega_z$, such that a suitably chosen detuning allows us to approximate $\sqrt{(\kappa/2)^2+\Delta^2} \approx \Omega_z$. In that case, the ratio of the maximal coupling strengths is given by

$$\frac{\max g_\text{cav-tw}}{\max g_\text{disp}} = \frac{E_\mathrm{d}kz_\mathrm{zpf}}{\frac{g_0E_\mathrm{d}}{\sqrt{(\kappa/2)^2+\Delta^2}}} \approx \frac{\Omega_z kz_\mathrm{zpf}}{g_0} = \frac{4\epsilon_0\Omega_z V_\mathrm{cav}}{\alpha\omega_\mathrm{cav}}. \tag{2.68}$$

We expect the coupling from the interference field to dominate over the dispersive coupling for our current cavity parameters. As we aim to reduce the cavity's mode volume in order to increase E_d, however, this ratio may eventually be reversed. Finding the ideal placement of the particle is thus a delicate matter, which additionally requires a profound assessment of the degree to which phase noise poses a problem at the relevant frequencies. We treat this question in further detail in sec. 3.4.2. We can also identify two kinds of constant forces $\propto \hbar E_\mathrm{d}k\,\mathrm{Re}(\tilde{\alpha})\mathrm{Re}(\boldsymbol{\epsilon}_\mathrm{cav}^*\cdot\boldsymbol{\epsilon}_\mathrm{tw})$ and $\propto \hbar(g_0/z_\mathrm{zpf})|\tilde{\alpha}|^2$, which vanish when the particle is placed in a node.

We can now finally evaluate the Fourier transform of eqs. (2.65a) and (2.67). This will allow us to find the mechanical susceptibility in analogy to eq. (2.3) and hence the PSD of our mechanical oscillator, which is related to its temperature by eq. (2.9). We obtain

$$\hat{\tilde{a}}(\Omega) = -i\tilde{\chi}_a(\Omega)\left[E_\mathrm{d}k\,\mathrm{Re}(\boldsymbol{\epsilon}_\mathrm{cav}^*\cdot\boldsymbol{\epsilon}_\mathrm{tw})\sin(kz_0)+\frac{g_0}{z_\mathrm{zpf}}\tilde{\alpha}\sin(2kz_0)\right]\hat{\tilde{z}}(\Omega) \tag{2.69a}$$

$$
\begin{aligned}
\frac{\hat{\tilde{z}}(\Omega)}{\tilde{\chi}_z(\Omega)} =& -\hbar\frac{E_\mathrm{d}k}{m}\,\mathrm{Re}(\boldsymbol{\epsilon}^*_\mathrm{cav}\cdot\boldsymbol{\epsilon}_\mathrm{tw})\sin(kz_0)\left(\hat{\tilde{a}}^\dagger(\Omega)+\hat{\tilde{a}}(\Omega)\right)\\
&-\hbar\frac{g_0}{mz_\mathrm{zpf}}\sin(2kz_0)\left(\tilde{\alpha}\hat{\tilde{a}}^\dagger(\Omega)+\tilde{\alpha}^*\hat{\tilde{a}}(\Omega)\right)+\frac{\tilde{F}_\mathrm{tot}(\Omega)}{m}\\
=& -\frac{\hbar}{m}\Bigg[(i\tilde{\chi}^*_a(-\Omega)-i\tilde{\chi}_a(\Omega))\Bigg(E_\mathrm{d}^2k^2\sin^2(kz_0)\mathrm{Re}(\boldsymbol{\epsilon}^*_\mathrm{cav}\cdot\boldsymbol{\epsilon}_\mathrm{tw})^2\\
&+\left(\frac{g_0}{z_\mathrm{zpf}}\right)^2|\tilde{\alpha}|^2\sin^2(2kz_0)\\
&+\frac{2E_\mathrm{d}kg_0}{z_\mathrm{zpf}}\sin(kz_0)\sin(2kz_0)\,\mathrm{Re}(\boldsymbol{\epsilon}^*_\mathrm{cav}\cdot\boldsymbol{\epsilon}_\mathrm{tw})\mathrm{Re}(\tilde{\alpha})\Bigg)\Bigg]\hat{\tilde{z}}(\Omega)+\frac{\tilde{F}_\mathrm{tot}(\Omega)}{m}\\
=& -\frac{\hbar}{m}\left(i\tilde{\chi}^*_a(-\Omega)-i\tilde{\chi}_a(\Omega)\right)\\
&\cdot\left|E_\mathrm{d}k\sin(kz_0)\,\mathrm{Re}(\boldsymbol{\epsilon}^*_\mathrm{cav}\cdot\boldsymbol{\epsilon}_\mathrm{tw})+\frac{g_0}{z_\mathrm{zpf}}\tilde{\alpha}\sin(2kz_0)\right|^2\hat{\tilde{z}}(\Omega)+\frac{\tilde{F}_\mathrm{tot}(\Omega)}{m},
\end{aligned}
\tag{2.69b}
$$

where we absorbed the constant forces into the total force $\tilde{F}_\mathrm{tot}$ and defined

$$
\tilde{\chi}_a(\Omega)=\frac{1}{\frac{\kappa_\mathrm{eff}}{2}+i(\Delta_\mathrm{eff}-\Omega)} \tag{2.70}
$$

$$
\tilde{\chi}_z(\Omega)=\frac{1}{\Omega_z^2-\Omega^2-i\Omega\Gamma}. \tag{2.71}
$$

We also made use of the fact that $\tilde{\chi}_{a^\dagger}(\Omega)=\tilde{\chi}^*_a(-\Omega)$ as one can easily check by writing down the equation of motion for $\hat{a}^\dagger$ in analogy to eq. (2.65a). Inserting those expressions into eq. (2.69b), we find that

$$
\tilde{z}(\Omega)=\tilde{\chi}'(\Omega)\frac{\tilde{F}_\mathrm{tot}(\Omega)}{m}, \tag{2.72}
$$

where

$$
\begin{aligned}
\tilde{\chi}'^{-1}(\Omega) &= \Omega_z^2-\Omega^2-i\Omega\Gamma-\frac{\hbar}{m}\frac{2\Delta_\mathrm{eff}\left|E_\mathrm{d}k\sin(kz_0)\,\mathrm{Re}(\boldsymbol{\epsilon}^*_\mathrm{cav}\cdot\boldsymbol{\epsilon}_\mathrm{tw})+\frac{g_0}{z_\mathrm{zpf}}\tilde{\alpha}\sin(2kz_0)\right|^2}{\left(\frac{\kappa_\mathrm{eff}}{2}\right)^2+(\Delta_\mathrm{eff}+\Omega)(\Delta_\mathrm{eff}-\Omega)+i\frac{\kappa_\mathrm{eff}}{2}\left[(\Delta_\mathrm{eff}-\Omega)-(\Delta_\mathrm{eff}+\Omega)\right]}\\
&= \Omega_z^2-\Omega^2-i\Omega\Gamma-\frac{\hbar}{m}\frac{2\Delta_\mathrm{eff}\left|E_\mathrm{d}k\sin(kz_0)\,\mathrm{Re}(\boldsymbol{\epsilon}^*_\mathrm{cav}\cdot\boldsymbol{\epsilon}_\mathrm{tw})+\frac{g_0}{z_\mathrm{zpf}}\tilde{\alpha}\sin(2kz_0)\right|^2\left[\left(\frac{\kappa_\mathrm{eff}}{2}\right)^2+\Delta_\mathrm{eff}^2-\Omega^2+i\kappa_\mathrm{eff}\Omega\right]}{\left[\left(\frac{\kappa_\mathrm{eff}}{2}\right)^2+(\Delta_\mathrm{eff}+\Omega)^2\right]\left[\left(\frac{\kappa_\mathrm{eff}}{2}\right)^2+(\Delta_\mathrm{eff}-\Omega)^2\right]}\\
&= \Omega_z^2-\Omega^2-i\Omega\Gamma-\frac{4\Omega_z\Delta_\mathrm{eff}\left|E_\mathrm{d}kz_\mathrm{zpf}\sin(kz_0)\,\mathrm{Re}(\boldsymbol{\epsilon}^*_\mathrm{cav}\cdot\boldsymbol{\epsilon}_\mathrm{tw})+g_0\tilde{\alpha}\sin(2kz_0)\right|^2\left[\left(\frac{\kappa_\mathrm{eff}}{2}\right)^2+\Delta_\mathrm{eff}^2-\Omega^2+i\kappa_\mathrm{eff}\Omega\right]}{\left[\left(\frac{\kappa_\mathrm{eff}}{2}\right)^2+(\Delta_\mathrm{eff}+\Omega)^2\right]\left[\left(\frac{\kappa_\mathrm{eff}}{2}\right)^2+(\Delta_\mathrm{eff}-\Omega)^2\right]}.
\end{aligned}
\tag{2.73}
$$

From eq. (2.73), we can identify an effective mechanical susceptibility with a modified damping Γ_eff,

$$
\Gamma_\mathrm{eff}=\Gamma+\frac{4\Omega_z\Delta_\mathrm{eff}\kappa_\mathrm{eff}\left|E_\mathrm{d}kz_\mathrm{zpf}\sin(kz_0)\,\mathrm{Re}(\boldsymbol{\epsilon}^*_\mathrm{cav}\cdot\boldsymbol{\epsilon}_\mathrm{tw})+g_0\tilde{\alpha}\sin(2kz_0)\right|^2}{\left[\left(\frac{\kappa_\mathrm{eff}}{2}\right)^2+(\Delta_\mathrm{eff}+\Omega)^2\right]\left[\left(\frac{\kappa_\mathrm{eff}}{2}\right)^2+(\Delta_\mathrm{eff}-\Omega)^2\right]}. \tag{2.74}
$$

We hence obtain for the final effective temperature

$$
T_\mathrm{eff}=T\frac{\Gamma}{\Gamma_\mathrm{eff}}, \tag{2.75}
$$

which, by virtue of eq. (2.8), translates to an average phononic occupation number

$$
\langle n\rangle=\frac{\langle z^2\rangle}{z_\mathrm{zpf}^2}=\frac{k_BT}{m\Omega_z^2z_\mathrm{zpf}^2}\frac{\Gamma}{\Gamma_\mathrm{eff}}. \tag{2.76}
$$

Additionally, we should point out that eq. (2.73) also contains an effective mechanical frequency

$$\Omega_{z,\mathrm{eff}} = \sqrt{\Omega_z^2 - \frac{4\Omega_z \Delta_{\mathrm{eff}} \left| E_\mathrm{d} k z_{\mathrm{zpf}} \sin(kz_0) \,\mathrm{Re}(\boldsymbol{\epsilon}_{\mathrm{cav}}^* \cdot \boldsymbol{\epsilon}_{\mathrm{tw}}) + g_0 \tilde{\alpha} \sin(2kz_0) \right|^2 \left[\left(\frac{\kappa_{\mathrm{eff}}}{2}\right)^2 + \Delta_{\mathrm{eff}}^2 - \Omega^2 \right]}{\left[\left(\frac{\kappa_{\mathrm{eff}}}{2}\right)^2 + (\Delta_{\mathrm{eff}} + \Omega)^2 \right] \left[\left(\frac{\kappa_{\mathrm{eff}}}{2}\right)^2 + (\Delta_{\mathrm{eff}} - \Omega)^2 \right]}}. \tag{2.77}$$

The damping of the motion along the x- and y-axis follows along the same lines. For the sake of completeness, we only state the respective equations of motion:

$$\begin{aligned} \ddot{\hat{x}} = &- \Gamma \dot{\hat{x}} - \Omega_x^2 \hat{x} - \frac{\hbar E_\mathrm{d}}{m} \mathrm{Re}(\boldsymbol{\epsilon}_{\mathrm{cav}}^* \cdot \boldsymbol{\epsilon}_{\mathrm{tw}}) \cos(kz_0) \left[i \left(\frac{1}{2x_{zR}} + \frac{1}{2x_{yR}} - k \right) (\hat{a} + \tilde{\alpha}) + \mathrm{h.c.} \right] \\ &+ \frac{F_{\mathrm{ext}}^{(x)}}{m} \end{aligned} \tag{2.78a}$$

$$\ddot{\hat{y}} = - \Gamma \dot{\hat{y}} - \Omega_y^2 \hat{y} + \frac{F_{\mathrm{ext}}^{(y)}}{m}. \tag{2.78b}$$

Eq. (2.78) reveals that the x-motion couples to the phase of the trapping beam. The y-motion does not couple directly to the optical mode. However, cooling is still possible provided that $\Omega_y \neq \Omega_z$ [34]. According to eqs. (2.26b) and (2.26c), this requires an elliptical beam shape of the tweezer, $W_{y0} \neq W_{z0}$.

2.3 Coherent Scattering Cooling of the Spatio-orientational Degrees of Freedom

Thus far, we have only considered cooling of the translational motion. We now extend the discussion to elucidate how coherent scattering allows to address all spatio-orientational degrees of freedom of an anisotropic particle simultaneously. More precisely, our particles are assumed to be elliptically shaped and to feature a uniform material composition. Just like in sec. 2.2, we will see that an appropriately chosen detuning of the cavity mode with respect to the laser field in combination with a suitable positioning along the cavity axis causes the particle to dissipate mechanical energy.
We will first review the interaction of an anisotropic particle with an external electric field, which will enable us to determine the Hamiltonian of the total system. We will then outline the steps to solve the resulting equations of motion and identify the effective damping rate that is responsible for the cooling effect.

2.3.1 Orientational Degrees of Freedom and Rotational Dynamics

Since we now need to account for the spatial extent of our particle, we must first define a *body-fixed* frame of reference that is co-moving with the particle and allows us to unambiguously specify its orientation. We choose its axes to coincide with the principal axes of the ellipsoid and refer to this particular option as the *principal axis frame*. This choice of coordinate system is shown in fig. 2.2.
The body's orientation is then fixed by three angles $\Omega = (\alpha, \beta, \gamma)$, termed *Euler angles*, which describe the rotation that transfers the space-fixed into the body-fixed frame of reference. The choice of these angles is not unique and we will in the following adopt the x-y'-x'' convention as displayed in fig. 2.3. In this case, the angles correspond to a rotation of the space-fixed frame by α around the x-axis, followed by a rotation by β around the y'-axis of the new coordinate system (x', y', z') that results from the first rotation and eventually a rotation by γ around the x'' axis of the final coordinate system (x'', y'', z'').

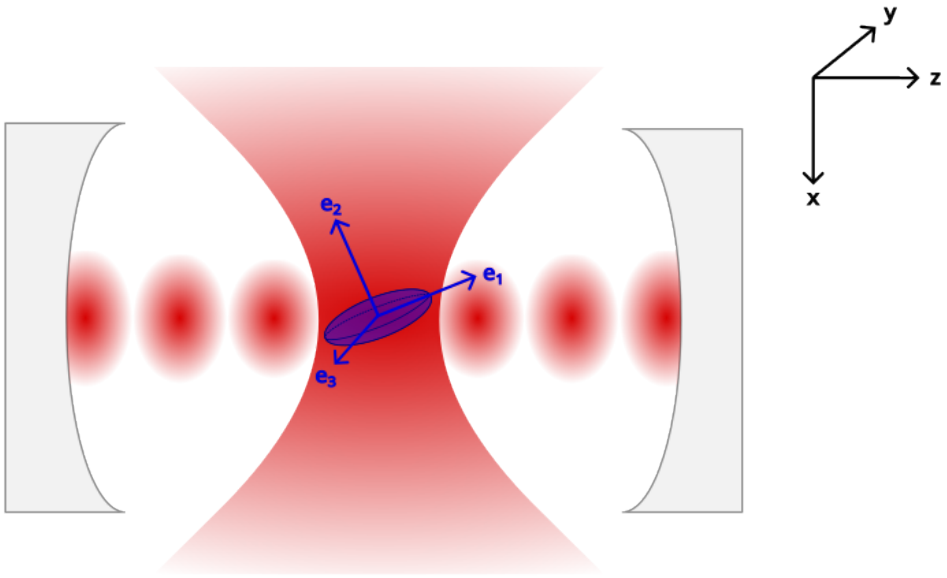

Figure 2.2: Coherent scattering of an optically levitated ellipsoidal particle inside a cavity. The principal axis frame is chosen as the body-fixed frame of reference in such a way that the polarizabilities along the body-fixed axes obey $\alpha_1 \geq \alpha_2 \geq \alpha_3$.

When subjected to an external electric field, the response of an anisotropic particle depends on its orientation. It is then no longer adequate to treat the polarizability as a scalar quantity. Instead, it must be described by a tensor, which is diagonal in the principal axis frame,

$$\boldsymbol{\alpha} = \mathrm{diag}(\alpha_1, \alpha_2, \alpha_3). \tag{2.79}$$

Without loss of generality, we can choose the axes in such a way that $\alpha_1 \geq \alpha_2 \geq \alpha_3$.
Assuming an elliptical particle with half-axes a_1, a_2 and a_3, the elements of the polarizability tensor differ by *depolarization factors* L_j [51], which read

$$\frac{V\epsilon_0}{\alpha_j} = \frac{1}{n^2 - 1} + L_j, \tag{2.80}$$

where

$$L_1 = \frac{a_1 a_2 a_3}{2} \int_0^\infty \frac{\mathrm{d}s}{(s + a_1^2)^{3/2}\sqrt{(s + a_2^2)(s + a_3^2)}} \tag{2.81}$$

and the others follow by cyclic permutation of the indices.
We may transform $\boldsymbol{\alpha}$ from the principal axis to the space-fixed frame according to

$$\boldsymbol{\alpha}(\Omega) = \boldsymbol{R}(\Omega)\boldsymbol{\alpha}\boldsymbol{R}^T(\Omega), \tag{2.82}$$

where the rotation matrix $\boldsymbol{R}(\Omega)$ is given by the product

$$\begin{aligned}\boldsymbol{R}(\Omega) &= \boldsymbol{R}_x(\alpha)\boldsymbol{R}_y(\beta)\boldsymbol{R}_x(\gamma) \\ &= \begin{pmatrix} \cos(\beta) & \sin(\beta)\sin(\gamma) & \sin(\beta)\cos(\gamma) \\ \sin(\alpha)\sin(\beta) & \cos(\alpha)\cos(\gamma) - \sin(\alpha)\cos(\beta)\sin(\gamma) & -\sin(\alpha)\cos(\beta)\cos(\gamma) - \cos(\alpha)\sin(\gamma) \\ -\cos(\alpha)\sin(\beta) & \cos(\alpha)\cos(\beta)\sin(\gamma) + \sin(\alpha)\cos(\gamma) & \cos(\alpha)\cos(\beta)\cos(\gamma) - \sin(\alpha)\sin(\gamma) \end{pmatrix}.\end{aligned} \tag{2.83}$$

We can convince ourselves of the correct order of the matrices by keeping in mind that they correspond to rotations of the space-fixed frame. If we want to compute the dipole moment in the space-fixed frame according to $\mathbf{d} = \boldsymbol{\alpha}(\Omega)\mathbf{E}$, we must hence first perform an inverse rotation of the electric field vector to obtain its components in the principal axis frame, then apply the diagonal polarizability tensor and finally rotate back to the original frame.

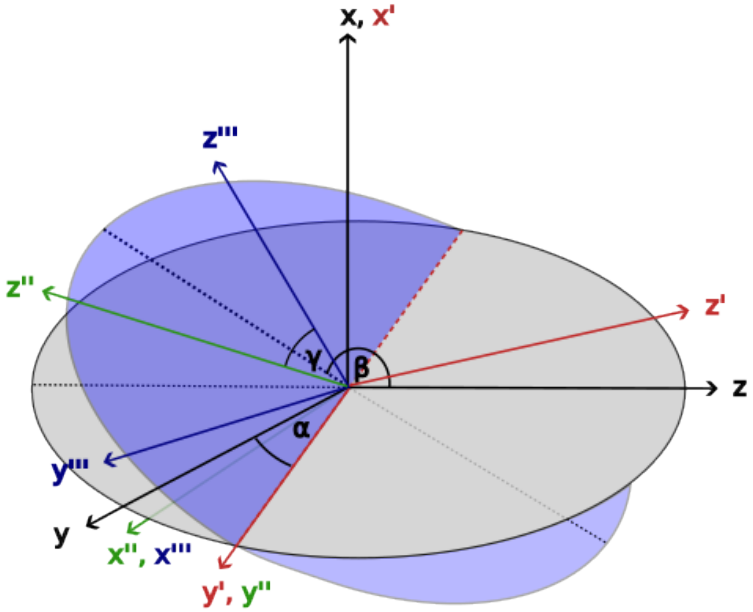

Figure 2.3: The Euler angles in x-y'-x'' convention. A rotation around the x-axis by an angle α is followed by a rotation of β around the y'-axis of the new coordinate system that results from the first transformation and finally by a rotation of γ around the x''-axis.

In analogy to eq. (2.21) for the isotropic case, the optical potential now reads [55]

$$U_{\text{dip}}(\mathbf{r},t) = -\frac{1}{2}\mathbf{E}^*(\mathbf{r},t)\cdot\boldsymbol{\alpha}(\Omega)\mathbf{E}(\mathbf{r},t). \tag{2.84}$$

When exposed to a light field, the interaction of the induced dipole moment with the electric field does hence not only give rise to a conservative optical force, the time-average of which is given by [55]

$$\langle\mathbf{F}_{\text{dip}}\rangle = \sum_{i\in\{x,y,z\}}\langle d_i(t)\cdot\nabla E_i(t)\rangle, \tag{2.85}$$

where d_i and E_i denote the real parts of the components of the dipole moment and the electric field, respectively, but also a conservative torque

$$\langle\mathbf{N}_{\text{dip}}\rangle = \langle\mathbf{d}\times\mathbf{E}\rangle. \tag{2.86}$$

Like in sec. 2.2, $\mathbf{E}(\mathbf{r})$ is just the sum of the intracavity field and trapping field. The torque also features a self-induced contribution from the scattered field, which only becomes relevant when the external torque is (close to) zero [56]. In addition, the laser exerts non-conservative radiation pressure and torque, which we can neglect for the moment, but will become important when we discuss particle trapping in sec. 4.1.2.

Eq. (2.86) states that the torque induced by a linearly polarized light field tends to align the axis of the largest polarizability with the polarization axis. As an example, a dielectric experiences zero torque at $\Omega_{\text{min}} = (0,0,\frac{\pi}{4})$ when the laser beam is polarized in the direction $\boldsymbol{\epsilon}_{\text{lin}} = \frac{1}{\sqrt{2}}(0,1,1)^T$. In the case of circular polarization, $\boldsymbol{\epsilon}_{\text{circ}} = \frac{1}{\sqrt{2}}(0,1,i)^T$, the particle always experiences a torque directed along the tweezer axis, which will cause it to spin in the plane of polarization until it reaches a steady-state angular frequency due to the damping forces that act against the continued acceleration.

As we will see in sec. 2.3.2, addressing the rotational degrees of freedom requires elliptical polarization of the trapping beam [55], which can be interpreted as a superposition of horizontal and vertical polarization with a constant phase difference. Assuming the latter to be equal to $\pi/2$, the polarization vector may be written as $\boldsymbol{\epsilon}_{\text{ell}} = (0,\cos\phi, i\sin\phi)^T$, where $\phi\in[0,\pi/4)$ is called the *ellipticity parameter*.

2.3.2 Optomechanical Hamiltonian of an Anisotropic Dielectric

Like in sec. 2.2.1, the optomechanical Hamiltonian that we are looking for contains terms pertaining to the bare fields, the particle motion and the particle-field interaction. The only differences to the previous treatment are the tensor form of the polarizability, the presence of the angular degrees of freedom and the fact that we now need to take both orthogonal polarization modes of the cavity field into account, which, for simplicity, we assume to be degenerate in frequency.[7]

Field Hamiltonian

Let us first write down the field term. Making again the approximation that the free spectral range of the cavity is large enough for only one resonance frequency to be relevant to the dynamics, we obtain an expression for the cavity field that is completely analogous to eq. (2.16),

$$\hat{\mathbf{E}}_{\text{cav}}(\mathbf{r},t) = i\sqrt{\frac{\hbar\omega_{\text{cav}}}{2\epsilon_0 V_{\text{cav}}}} \sum_{j\in\{1,2\}} \boldsymbol{\epsilon}_j \left(\hat{a}_j f_{\text{cav}}(\mathbf{r}) e^{-i\omega_{\text{cav}}t} - \hat{a}_j^\dagger f_{\text{cav}}^*(\mathbf{r}) e^{i\omega_{\text{cav}}t}\right), \tag{2.87}$$

where the indices refer to the two polarization directions. As we did before, we then switch to a frame of reference rotating at the frequency of the drive laser. The field Hamiltonian thus becomes

$$\hat{H}_{\text{field}} = \hbar\Delta \left(\hat{a}_1^\dagger \hat{a}_1 + \hat{a}_2^\dagger \hat{a}_2\right). \tag{2.88}$$

Particle Hamiltonian

It is well-known from classical mechanics that we may use generalized coordinates and their conjugate momenta to treat all degrees of freedom on the same footing. Specifically, we obtain the conjugate momenta p_q from system's Lagrangian $\mathcal{L}$ according to

$$p_q = \frac{\partial \mathcal{L}}{\partial \dot{q}}, \tag{2.89}$$

where $q \in \{x, y, z, \alpha, \beta, \gamma\}$. The Hamiltonian then takes the form

$$H = \sum_q p_q \dot{q} - \mathcal{L}. \tag{2.90}$$

Under free evolution, the potential vanishes and the Lagrangian is simply the sum of the linear kinetic and the rotational energy. The former yields the familiar expression $\mathbf{p}^2/(2m)$, while the rotational energy depends on orientation and is given by

$$E_{\text{rot}}(\Omega) = \frac{1}{2}\mathbf{L}\cdot\boldsymbol{I}^{-1}(\Omega)\mathbf{L}, \tag{2.91}$$

with $\mathbf{L}$ denoting the angular momentum and

$$\boldsymbol{I}(\Omega) = \boldsymbol{R}(\Omega)\boldsymbol{I}\boldsymbol{R}^T(\Omega) \tag{2.92}$$

the moment of inertia tensor in the space-fixed frame of reference. Just like the polarizability tensor, $\boldsymbol{I} = \text{diag}(I_1, I_2, I_3)$ is diagonal in the principal axis frame and [55]

$$I_k = \frac{1}{5}m(a_l^2 + a_m^2), \quad k \neq l \neq m. \tag{2.93}$$

[7] In practice, care must be taken due to possible birefringence of the mirrors [34].

By virtue of eq. (2.90), we need to express the rotational energy, eq. (2.91), in terms of the time derivatives of the Euler angles. These are related to the angular velocities ω_1, ω_2 and ω_3 in the principal axis frame by the transformation [57]

$$\begin{pmatrix}\omega_1\\ \omega_2\\ \omega_3\end{pmatrix} = \begin{pmatrix}\cos\beta & 0 & 1\\ \sin\beta\cos\gamma & -\sin\gamma & 0\\ \sin\beta\sin\gamma & \cos\gamma & 0\end{pmatrix}\begin{pmatrix}\dot\alpha\\ \dot\beta\\ \dot\gamma\end{pmatrix} \equiv \boldsymbol{A}\begin{pmatrix}\dot\alpha\\ \dot\beta\\ \dot\gamma\end{pmatrix} \tag{2.94}$$

as can be seen by adding up the projections of the angular time derivatives onto the respective axes of the body-centered frame [57] and comparing with fig. 2.3. Converting to the space-fixed frame, we consequently get

$$\begin{aligned}
E_{\text{rot}}(\Omega) &= \frac{1}{2}\begin{pmatrix}L_x & L_y & L_z\end{pmatrix}\boldsymbol{I}^{-1}(\Omega)\begin{pmatrix}L_x\\ L_y\\ L_z\end{pmatrix}\\
&= \frac{1}{2}\begin{pmatrix}\dot\alpha & \dot\beta & \dot\gamma\end{pmatrix}\boldsymbol{A}^T(\Omega)\boldsymbol{R}^T(\Omega)\boldsymbol{I}(\Omega)\boldsymbol{R}(\Omega)\boldsymbol{A}(\Omega)\begin{pmatrix}\dot\alpha\\ \dot\beta\\ \dot\gamma\end{pmatrix}\\
&= \frac{1}{2}\begin{pmatrix}\dot\alpha & \dot\beta & \dot\gamma\end{pmatrix}\boldsymbol{A}^T(\Omega)\boldsymbol{I}\boldsymbol{A}(\Omega)\begin{pmatrix}\dot\alpha\\ \dot\beta\\ \dot\gamma\end{pmatrix}\\
&= \frac{1}{2}\begin{pmatrix}\dot\alpha & \dot\beta & \dot\gamma\end{pmatrix}\begin{pmatrix}\sin^2\beta(I_2\cos^2\gamma+I_3\sin^2\gamma)+I_1\cos^2\beta & (I_3-I_2)\sin\beta\sin\gamma\cos\gamma & I_1\cos\beta\\ (I_3-I_2)\sin\beta\sin\gamma\cos\gamma & I_2\sin^2\gamma+I_3\cos^2\gamma & 0\\ I_1\cos\beta & 0 & I_1\end{pmatrix}\begin{pmatrix}\dot\alpha\\ \dot\beta\\ \dot\gamma\end{pmatrix}\\
&\equiv \frac{1}{2}\begin{pmatrix}\dot\alpha & \dot\beta & \dot\gamma\end{pmatrix}\mathbf{B}(\Omega)\begin{pmatrix}\dot\alpha\\ \dot\beta\\ \dot\gamma\end{pmatrix}.
\end{aligned} \tag{2.95}$$

Using eq. (2.89), it is then a simple exercise to compute the respective conjugate momenta as

$$\begin{aligned}
p_\alpha &= \dot\alpha\left[\sin^2\beta\left(I_2\cos^2\gamma + I_3\sin^2\gamma\right) + I_1\cos^2\beta\right] + \dot\beta(I_3 - I_2)\sin\beta\sin\gamma\cos\gamma\\
&\quad + \dot\gamma I_1\cos\beta
\end{aligned} \tag{2.96a}$$

$$p_\beta = \dot\alpha(I_3 - I_2)\sin\beta\sin\gamma\cos\gamma + \dot\beta(I_2\sin^2\gamma + I_3\cos^2\gamma) \tag{2.96b}$$

$$p_\gamma = I_1(\dot\alpha\cos\beta + \dot\gamma) \tag{2.96c}$$

or, in a more compact form,

$$\begin{pmatrix}p_\alpha\\ p_\beta\\ p_\gamma\end{pmatrix} = \boldsymbol{B}(\Omega)\begin{pmatrix}\dot\alpha\\ \dot\beta\\ \dot\gamma\end{pmatrix}. \tag{2.97}$$

We may now promote the conjugate momenta to operators, multiply eq. (2.97) from the left with $\boldsymbol{B}^{-1}(\Omega)$ and insert the result into eq. (2.95) to obtain the expression for the free-rotation Hamiltonian,

$$\begin{aligned}
\hat H_{\text{rot}} &= \frac{1}{2}\begin{pmatrix}\hat p_\alpha & \hat p_\beta & \hat p_\gamma\end{pmatrix}\boldsymbol{B}^{-1}(\Omega)\begin{pmatrix}\hat p_\alpha\\ \hat p_\beta\\ \hat p_\gamma\end{pmatrix}\\
&= \frac{1}{2I_2\sin^2\beta}\left[(\hat p_\alpha - \hat p_\gamma\cos\beta)\cos\gamma - \hat p_\beta\sin\beta\sin\gamma\right]^2\\
&\quad + \frac{1}{2I_3\sin^2\beta}\left[(\hat p_\alpha - \hat p_\gamma\cos\beta)\sin\gamma + \hat p_\beta\sin\beta\cos\gamma\right]^2 + \frac{\hat p_\gamma^2}{2I_1}.
\end{aligned} \tag{2.98}$$

Eq. (2.98) reveals that the rotational degrees of freedom are highly coupled. However, in the presence of a strong trapping field, the rotational motion decouples close to the potential minimum.

In this regime, the dynamics are *librational* rather than rotational, i.e. the angular coordinates perform small oscillations around their equilibrium position rather than full revolutions about any axis. In that case, the kinetic Hamiltonian becomes

$$\hat{H}_{\text{kin}} = \sum_q \frac{\hat{p}_q^2}{2m_q}, \tag{2.99}$$

where $m_x = m_y = m_z \equiv m$ and $m_\alpha = I_2$, $m_\beta = I_3$ and $m_\gamma = I_1$.
An harmonic approximation of the trapping potential $U_{\text{tw}} = -\frac{1}{2}\mathbf{E}_{\text{tw}}^* \cdot \alpha(\Omega)\mathbf{E}_{\text{tw}}$ leaves us with the problem of quantizing a 6D harmonic oscillator, which results in

$$\hat{H}_{\text{mech}} = \hbar \sum_q \Omega_q \hat{b}_q^\dagger \hat{b}_q \tag{2.100}$$

in complete analogy to eq. (2.27). As before, the trapping frequencies are obtained from the second-order coefficients in the expansion of the optical potential around the minimum $(\mathbf{r}, \Omega) = (\mathbf{r}_{\text{min}}, \Omega_{\text{min}})$, i.e.

$$\Omega_q = \sqrt{\frac{1}{m_q}\frac{\partial^2 U_{\text{tw}}}{\partial^2 q}\bigg|_{\mathbf{r}_{\text{min}},\Omega_{\text{min}}}}. \tag{2.101}$$

Interaction Hamiltonian

We are now ready to discuss the optomechanical interaction terms. For the contribution of the cavity field, we get

$$\hat{H}_{\text{cav}} = \frac{\hbar\omega_{\text{cav}}}{4\epsilon_0 V_{\text{cav}}}|f_{\text{cav}}(\mathbf{r})|^2 \sum_{j,j'\in\{1,2\}} \boldsymbol{\epsilon}_j^* \cdot \boldsymbol{\alpha}(\Omega)\boldsymbol{\epsilon}_{j'} \left(\hat{a}_j^\dagger \hat{a}_{j'} + \hat{a}_j \hat{a}_{j'}^\dagger\right), \tag{2.102}$$

where we have again applied the rotating wave approximation and the mode operators satisfy the canonical commutation relations $[\hat{a}_j, \hat{a}_{j'}^\dagger] = \delta_{jj'}$, $[\hat{a}_j, \hat{a}_{j'}] = 0$. We may hence rewrite eq. (2.102) in a more familiar form,

$$\begin{aligned}
\hat{H}_{\text{cav}} &= \frac{\hbar\omega_{\text{cav}}}{4\epsilon_0 V_{\text{cav}}}|f_{\text{cav}}(\mathbf{r})|^2 \sum_{j,j'=1,2} \boldsymbol{\epsilon}_j^* \cdot \boldsymbol{\alpha}(\Omega)\boldsymbol{\epsilon}_{j'} \left(\hat{a}_j^\dagger \hat{a}_{j'} + \hat{a}_{j'}^\dagger \hat{a}_j + \delta_{jj'}\right) \\
&= \frac{\hbar\omega_{\text{cav}}}{4\epsilon_0 V_{\text{cav}}}|f_{\text{cav}}(\mathbf{r})|^2 \Bigg[2\boldsymbol{\epsilon}_1^* \cdot \boldsymbol{\alpha}(\Omega)\boldsymbol{\epsilon}_1 \left(\hat{a}_1^\dagger \hat{a}_1 + \frac{1}{2}\mathbb{1}\right) \\
&\quad + 2\boldsymbol{\epsilon}_2^* \cdot \boldsymbol{\alpha}(\Omega)\boldsymbol{\epsilon}_2 \left(\hat{a}_2^\dagger \hat{a}_2 + \frac{1}{2}\mathbb{1}\right) + \boldsymbol{\epsilon}_1^* \cdot \boldsymbol{\alpha}(\Omega)\boldsymbol{\epsilon}_2 \left(\hat{a}_1^\dagger \hat{a}_2 + \hat{a}_2^\dagger \hat{a}_1\right) \\
&\quad + \boldsymbol{\epsilon}_2^* \cdot \boldsymbol{\alpha}(\Omega)\boldsymbol{\epsilon}_1 \left(\hat{a}_1^\dagger \hat{a}_2 + \hat{a}_2^\dagger \hat{a}_1\right)\Bigg] \\
&\approx \frac{\hbar\omega_{\text{cav}}}{2\epsilon_0 V_{\text{cav}}}|f_{\text{cav}}(\mathbf{r})|^2 \Big[\boldsymbol{\epsilon}_1^* \cdot \boldsymbol{\alpha}(\Omega)\boldsymbol{\epsilon}_1 \, \hat{a}_1^\dagger \hat{a}_1 + \boldsymbol{\epsilon}_2^* \cdot \boldsymbol{\alpha}(\Omega)\boldsymbol{\epsilon}_2 \, \hat{a}_2^\dagger \hat{a}_2 \\
&\quad + 2\,\mathrm{Re}(\boldsymbol{\epsilon}_1^* \cdot \boldsymbol{\alpha}(\Omega)\boldsymbol{\epsilon}_2) \left(\hat{a}_1^\dagger \hat{a}_2 + \hat{a}_2^\dagger \hat{a}_1\right)\Big],
\end{aligned} \tag{2.103}$$

where the cross terms $\hat{a}_1^\dagger \hat{a}_2$ and $\hat{a}_1 \hat{a}_2^\dagger$ refer, respectively, to the conversion of a photon in polarization mode 2 to a photon in polarization mode 1 and vice versa. We also omit the constant terms in the last approximation. From eq. (2.103) it is evident that the particle can couple to both polarization modes depending on its orientation.
What is left to write down is the interference term $\hat{H}_{\text{cav-tw}}$ proportional to $\hat{\mathbf{E}}_{\text{cav}} \cdot \boldsymbol{\alpha}(\Omega)\mathbf{E}_{\text{tw}}^* + \text{h.c.}$. In analogy to eq. (2.38), we obtain the expression

$$\hat{H}_{\text{cav-tw}} = -\frac{1}{2}\sqrt{\frac{\hbar\omega_{\text{cav}}}{2\epsilon_0 V_{\text{cav}}}} E_{\text{tw}} \sum_{j\in\{1,2\}} \mathrm{Re}(\boldsymbol{\epsilon}_j^* \cdot \boldsymbol{\alpha}(\Omega)\boldsymbol{\epsilon}_{\text{tw}}) \left(\hat{a}_j f_{\text{cav}}(\mathbf{r}) f_{\text{tw}}^*(\mathbf{r}) e^{-i\omega_{\text{cav}}t} + \text{h.c.}\right), \tag{2.104}$$

which is already in the rotating frame of reference. As we have done in sec. 2.2.1, we may then restrict ourselves to the *deep trapping regime*, in which the displacements of all ro-translational coordinates are sufficiently small to allow for the linearization the interaction Hamiltonian. This means that we also need to expand the polarizability tensor $\boldsymbol{\alpha}(\Omega)$ to first order, the result of which is presented in ref. [58], eq. (27c). By linearizing the Hamiltonian, we also neglect the couplings between the different mechanical modes, which appear only in the second order of the expansion.

2.3.3 Ro-translational Equations of Motion and Cooling

We are now interested in the dynamics of the mode operators. We have already outlined the way to do this in sec. 2.2.3, but we now need to account for the coupling between the two polarization modes as a result of the off-diagonal terms in the polarizability tensor. The equation of motion for the $\hat{a}_j$'s is thus most conveniently written as a matrix equation [58],

$$\dot{\hat{\boldsymbol{a}}} = \boldsymbol{M}(\mathbf{r}, \Omega)\hat{\boldsymbol{a}} + \boldsymbol{\zeta}(\mathbf{r}, \Omega), \tag{2.105}$$

where $\hat{\boldsymbol{a}} = (\hat{a}_1, \hat{a}_2)^T$, $\boldsymbol{\zeta}$ is the drive vector and the matrix $\boldsymbol{M}$ contains the effective detuning and the decay rate,

$$\boldsymbol{M}_{jj'} = -i[\boldsymbol{\Delta}_{\text{eff}}]_{jj'} - \frac{1}{2}[\boldsymbol{\kappa}_{\text{eff}}]_{jj'}, \tag{2.106}$$

where

$$[\boldsymbol{\Delta}_{\text{eff}}]_{jj'} = \Delta\delta_{jj'} + \frac{\omega_{\text{cav}}}{2\epsilon_0 V_{\text{cav}}}|f_{\text{cav}}(\mathbf{r})|^2 \,\text{Re}\big(\boldsymbol{\epsilon}_j^* \cdot \boldsymbol{\alpha}(\Omega)\boldsymbol{\epsilon}_{j'}\big) \tag{2.107a}$$

$$[\boldsymbol{\kappa}_{\text{eff}}]_{jj'} = \kappa\delta_{jj'} + 2\pi\frac{4\Delta\nu_{\text{FSR}}k^4}{3\epsilon_0^2\pi^2 w_0^2}|f_{\text{cav}}(\mathbf{r})|^2 \,\text{Re}\big(\mathbf{e}_j^* \cdot \boldsymbol{\alpha}^2(\Omega)\mathbf{e}_{j'}\big)\,. \tag{2.107b}$$

The effective decay rate κ_{eff} coincides with eq. (2.53) once the scalar polarizability, which is contained in the mode overlap η by virtue of eq. (2.45), is replaced by the corresponding tensorial expression. The components of the drive vector read

$$\begin{aligned}\zeta_j =& i\sqrt{\frac{\omega_{\text{cav}}}{2\hbar\epsilon_0 V_{\text{cav}}}}E_{\text{tw}} f_{\text{cav}}^*(\mathbf{r}) f_{\text{tw}}(\mathbf{r}) \text{Re}\big(\boldsymbol{\epsilon}_j^* \cdot \boldsymbol{\alpha}(\Omega)\boldsymbol{\epsilon}_{\text{tw}}\big) \\ &+ i\frac{\omega_{\text{cav}}}{2\epsilon_0 V_{\text{cav}}}|f_{\text{cav}}(\mathbf{r})|^2 \tilde{\alpha}_j \sum_{j'\in\{1,2\}} \text{Re}\big(\boldsymbol{\epsilon}_j^* \cdot \boldsymbol{\alpha}(\Omega)\boldsymbol{\epsilon}_{j'}\big)\,,\end{aligned} \tag{2.108}$$

where the first term stems from the overlap of the cavity and the trapping field and the second from the coherent offset of the cavity field. The equations of motion thus read

$$\dot{\hat{a}}_j = -\sum_{j'\in\{1,2\}}\left(i\,[\boldsymbol{\Delta}_{\text{eff}}]_{jj'} + \frac{1}{2}\,[\boldsymbol{\kappa}_{\text{eff}}]_{jj'}\right)\hat{a}_{j'} + \zeta_j \tag{2.109}$$

$$\dot{\hat{q}} = \frac{\hat{p}_q}{m_q}, \tag{2.110}$$

where $\hat{p}_q$ has been defined in eq. (2.89).

In order to solve these equations in Fourier space, we would like to eliminate the coupling between the optical modes. As is immediately obvious from eq. (2.107), the off-diagonal elements of $\boldsymbol{M}$ vanish when $|f_{\text{cav}}(\mathbf{r})|^2 = 0$, i.e. when the particle sits in a node of the cavity field.[8] If the particle is located at a different position, we may still define the polarization modes in such a way that

[8] Note that in this case, the cavity is unpopulated and the coupling to the rotational degrees of freedom as well as to the x-motion vanishes.

the optical modes are decoupled. Indeed, since $\boldsymbol{\Delta}_{\text{eff}}$ and $\boldsymbol{\kappa}_{\text{eff}}$ are both symmetric, their sum is also symmetric and $\boldsymbol{M}$ is hence diagonalizable.
In the case of a stably trapped particle, for example, we may treat both modes independently if we choose $\boldsymbol{\epsilon}_1$ to point in the tweezer direction and $\boldsymbol{\epsilon}_2$ in the y-direction. The linearized Hamiltonian then takes a form that is analogous to eq. (2.62) upon applying the transformation $\hat{a}_j \to \hat{a}_j + \tilde{\alpha}_j$,

$$\begin{aligned}\hat{H}_{\text{opt}} \approx{}& \hbar \sum_j \Delta^{(0)}_{\text{eff},j} \left(\hat{a}_j^\dagger \hat{a}_j + \hat{a}_j^\dagger \tilde{\alpha}_j + \hat{a}_j \tilde{\alpha}_j^*\right) + \hbar \sum_q \Omega_q \hat{b}_q^\dagger \hat{b}_q \\ &+ \hbar \sum_j G_j^{(0)} \left[\left(\hat{a}_j + \tilde{\alpha}_j\right) e^{-i\omega_{\text{cav}} t} + \left(\hat{a}_j^\dagger + \tilde{\alpha}_j^*\right) e^{i\omega_{\text{cav}} t}\right] \\ &+ \hbar \sum_{jq} G_{jq}^{(1)} \left(\hat{b}_q^\dagger + \hat{b}_q\right) \left[\left(\hat{a}_j + \tilde{\alpha}_j\right) e^{-i\omega_{\text{cav}} t} + \left(\hat{a}_j^\dagger + \tilde{\alpha}_j^*\right) e^{i\omega_{\text{cav}} t}\right] \\ &+ \hbar \sum_{jq} g_{jq}^{(1)} \left(\hat{b}_q^\dagger + \hat{b}_q\right) \left(\hat{a}_j^\dagger \hat{a}_j + \hat{a}_j^\dagger \tilde{\alpha}_j + \hat{a}_j \tilde{\alpha}_j^* + |\tilde{\alpha}_j|^2\right),\end{aligned} \tag{2.111}$$

where $\Delta^{(0)}_{\text{eff},j}$ is the zeroth-order term in the expansion of eq. (2.107a), $G_j^{(0)}$ pertains to the constant part of eq. (2.104) and the linear coupling rates $G_{jq}^{(1)}$ and $g_{jq}^{(1)}$ quantify the first-order optomechanical coupling induced by eqs. (2.104) and (2.103), respectively. We consequently obtain

$$\dot{\hat{a}}_j = -\left(i\Delta^{(0)}_{\text{eff},j} + \frac{\kappa^{(0)}_{\text{eff},j}}{2}\right)\hat{a}_j - i\sum_q \left(G_{jq}^{(1)} + g_{jq}^{(1)}\tilde{\alpha}_j\right)\left(\hat{b}_q^\dagger + \hat{b}_q\right) \tag{2.112}$$

$$\begin{aligned}\ddot{\hat{q}} = {}& -\Gamma_q \dot{\hat{q}} - \Omega_q^2 \hat{q} - \frac{\hbar}{m_q q_{\text{zpf}}} G_{jq}^{(1)} \left[\left(\hat{a}_j + \tilde{\alpha}_j\right) + \text{h.c.}\right] \\ & - \frac{\hbar}{m_q q_{\text{zpf}}} g_{jq}^{(1)} \left(\hat{a}_j^\dagger \tilde{\alpha}_j + \hat{a}_j \tilde{\alpha}_j^* + |\tilde{\alpha}_j|^2\right) + \frac{F^{(q)}_{\text{ext}}(t)}{m_q}.\end{aligned} \tag{2.113}$$

We omitted the sums over j because every degree of freedom couples to just one optical mode. The external force is to be understood in the generalized sense, i.e. it also includes torques acting on the angular coordinates.

We can now write down the equations of motion in Fourier space in complete analogy to the procedure outlined in sec. 2.2.3. We then get

$$\hat{\tilde{a}}_j(\Omega) = -i\tilde{\chi}_{a_j}(\Omega)\sum_q \left(G_{jq}^{(1)} + g_{jq}^{(1)}\tilde{\alpha}_j\right)\left(\hat{\tilde{b}}_q^\dagger(\Omega) + \hat{\tilde{b}}_q(\Omega)\right) \tag{2.114}$$

$$\begin{aligned}\frac{\hat{\tilde{q}}(\Omega)}{\tilde{\chi}_q(\Omega)} = {}& -\frac{\hbar}{m_q q_{\text{zpf}}}\left[G_{jq}^{(1)}\left(\hat{\tilde{a}}_j^\dagger(\Omega) + \hat{\tilde{a}}_j(\Omega)\right) + g_{jq}^{(1)}\left(\hat{\tilde{a}}_j^\dagger(\Omega)\tilde{\alpha}_j + \hat{\tilde{a}}_j(\Omega)\tilde{\alpha}_j^*\right)\right] \\ & + \frac{\tilde{F}^{(q)}_{\text{tot}}(\Omega)}{m_q},\end{aligned} \tag{2.115}$$

where

$$\tilde{\chi}_{a_j}(\Omega) = \frac{1}{\frac{\kappa^{(0)}_{\text{eff},j}}{2} + i\left(\Delta^{(0)}_{\text{eff},j} - \Omega\right)} \tag{2.116}$$

$$\tilde{\chi}_q(\Omega) = \frac{1}{\Omega_q^2 - \Omega^2 - i\Gamma_q\Omega}. \tag{2.117}$$

We henceforth omit the superscript (0) of the effective detuning and decay rate. According to eq. (2.114), the equations for the generalized coordinates are still indirectly coupled via the optical

modes. Given a sufficiently small linewidth of the mechanical resonances we may, however, evaluate $\tilde{\chi}_{a_j}(\Omega)$ at the mechanical resonance frequency and neglect the contributions from other degrees of freedom [58]. Putting all together, we consequently get

$$\hat{\tilde{q}}(\Omega_q) = \tilde{\chi}'_q(\Omega_q)\frac{\tilde{F}^{(q)}_{\text{tot}}(\Omega_q)}{m_q}, \tag{2.118}$$

where

$$\begin{aligned}\tilde{\chi}_q^{-1}(\Omega_q) &= -i\Omega_q\Gamma_q - \frac{\hbar}{m_q q_{\text{zpf}}^2}\frac{2\Delta_{\text{eff},j}\left|G^{(1)}_{jq} + g^{(1)}_{jq}\tilde{\alpha}_j\right|^2}{\left(\frac{\kappa_{\text{eff},j}}{2}\right)^2 + (\Delta_{\text{eff},j}+\Omega_q)(\Delta_{\text{eff},j}-\Omega_q) - i\kappa_{\text{eff,j}}\Omega_q} \\ &= -i\Omega_q\Gamma_q - \frac{4\Omega_q\Delta_{\text{eff},j}\left|G^{(1)}_{jq} + g^{(1)}_{jq}\tilde{\alpha}_j\right|^2\left[\left(\frac{\kappa_{\text{eff},j}}{2}\right)^2 + \Delta^2_{\text{eff},j} - \Omega_q^2 + i\kappa_{\text{eff},j}\Omega_q\right]}{\left[\left(\frac{\kappa_{\text{eff},j}}{2}\right)^2 + (\Delta_{\text{eff},j}+\Omega_q)^2\right]\left[\left(\frac{\kappa_{\text{eff},j}}{2}\right)^2 + (\Delta_{\text{eff},j}-\Omega_q)^2\right]}.\end{aligned} \tag{2.119}$$

The effective damping for the q-coordinate thus reads

$$\Gamma_{\text{eff},q} = \Gamma_q + \frac{4\Omega_q\kappa_{\text{eff},j}\Delta_{\text{eff},j}\left|G^{(1)}_{jq} + g^{(1)}_{jq}\tilde{\alpha}_j\right|^2}{\left[\left(\frac{\kappa_{\text{eff},j}}{2}\right)^2 + (\Delta_{\text{eff},j}+\Omega_q)^2\right]\left[\left(\frac{\kappa_{\text{eff},j}}{2}\right)^2 + (\Delta_{\text{eff},j}-\Omega_q)^2\right]}, \tag{2.120}$$

from which the effective temperature follows according to eq. (2.75).

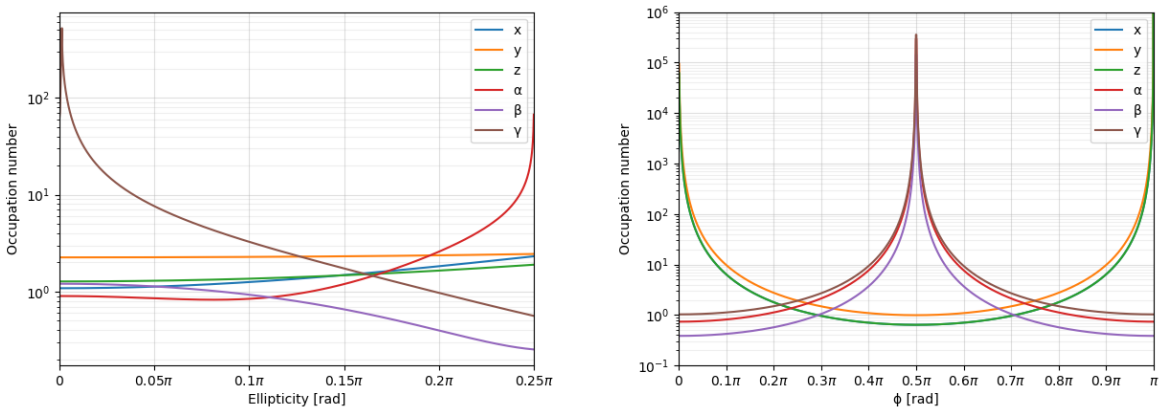

(a) **(b)**

Figure 2.4: Minimum mechanical occupation number as a function of (a) the ellipticity ψ at $\phi = 0.78\pi$, $\theta = 0.83\pi$, where ϕ denotes the phase of the cavity mode at the position of the particle and θ is the angle between the cavity axis and the minor axis of the elliptical tweezer cross section, (b) the phase ϕ at $\psi = 0.15\pi$, $\theta = 0.82\pi$. We assume a SiO_2 nanoparticle with principal diameters of (148, 150, 152)nm, a cavity with a length of L=18mm, a finesse of 295,000 and a waist of $w_0 = 97\mu$m, tweezer waists of $W_{x0} = 650$nm, $W_{y0} = 800$nm and a tweezer power of 250mW at a detuning of Δ = 2π·116kHz, a pressure of $p = 10^{-9}$mbar and room temperature. The simulation is based on the expressions for the coupling constants provided in ref. [58].

From the coupling rates, which we have not specified, but are stated in ref. [58][9], we can immediately see that choosing the axis of largest trapping beam intensity to align with the

[9]Note that the coupling rates in ref. [58] are with respect to a coordinate system defined by the propagation direction of the tweezer and the intensity main axes of its elliptical cross section. We continue use the same coordinate system as in sec. 2.2, which is related to the former by a rotation around the x-axis by the angle θ defined in ref. [58].

cavity axis would lead to zero coupling of the y-motion. A vanishing ellipticity would still allow coupling in all degrees of freedom. However, γ would then only be weakly coupled [58]. In order to be able to achieve simultaneous ground state cooling in all degrees of freedom, the separation between the respective trapping frequencies must be sufficiently small, which requires a particle asphericity at the percent level [55].
In fig. 2.4, we display the attainable occupation numbers (not including phase noise) for our current cavity parameters. As long as phase noise can be ignored, an improvement in the cavity waist from 97µm to 50µm would theoretically allow us to reach occupation numbers below unity in all degrees of freedom.

Chapter 3

Heating Mechanisms and Decoherence

Noise gives rise to adverse effects in the form of heating and, more generally, to decoherence. In this section, we will provide an overview over the various mechanisms, discuss their effect on our experiment and hint at possible ways to mitigate them.

3.1 Decoherence and Open System Dynamics

Suppose that we prepare a system in a pure quantum superposition state comprised of d linearly independent normalized vectors $\{|\psi_i\rangle\}_{i=1}^{d}$ in a suitable basis. Such a superposition state is characterized by a state vector $|\psi\rangle$ with

$$|\psi\rangle = \sum_{i=1}^{d} a_i |\psi_i\rangle, \qquad \sum_i |a_i|^2 = 1. \tag{3.1}$$

As any reputable introductory book on quantum mechanics (e.g. ref. [47]) will highlight, there is a clear distinction between such a state and a classical mixture of $\{|\psi_i\rangle\}_{i=1}^{d}$, which is described in terms of a density matrix of the form

$$\hat{\rho} = \sum_i |a_i|^2 |\psi_i\rangle\langle\psi_i|, \qquad \sum_i |a_i|^2 = 1. \tag{3.2}$$

The density matrix $\hat{\rho}' = |\psi\rangle\langle\psi|$ differs from eq. (3.2) by the presence of off-diagonal elements, termed *coherences*. These have a crucial consequence when it comes to the time evolution of the wave packet described by eq. (3.1). Restricting ourselves to a superposition of two distinct states ($d = 2$), the individual phases ϕ_1 and ϕ_2 that the two constituents acquire during their evolution bring about a sinusoidal variation in $\Delta\phi = \phi_2 - \phi_1$ of the probabilities to obtain $|\psi_1\rangle$ or $|\psi_2\rangle$ in a measurement. If the state were characterized by a classical mixture, those probabilities would remain constant and equal to $|a_1|^2$ and $|a_2|^2$ respectively.

The above scenario describes an idealized situation in which any interaction with the environment can be neglected. In reality, however, a quantum system can never be perfectly isolated, causing the environment to gain information on the particle's state. If it is then possible to reliably distinguish between the corresponding environmental states, the initial superposition state collapses into a classical mixture, i.e. it *decoheres*.

More formally, let us suppose that we manage to prepare our system in a well-defined quantum state (e.g. the motional ground state) at time $t = 0$. At this particular time, the system and the environment, represented by the state $|\Phi\rangle$, are decoupled,

$$|\Psi(0)\rangle = |\psi\rangle|\Phi_0\rangle. \tag{3.3}$$

Assuming an interaction Hamiltonian that is diagonal in the system of interest, the coupling causes the environmental state to evolve in a way that depends on the system state. For our

initial superposition, eq. (3.1), this means [59]

$$\left(\sum_i a_i|\psi_i\rangle\right)|\Phi_0\rangle \mapsto \sum_i a_i|\psi_i\rangle|\Phi_i(t)\rangle. \tag{3.4}$$

Provided that the environmental states are orthogonal, $\langle\Phi_i(t)|\Phi_j(t)\rangle = \delta_{ij}$, tracing over the environment destroys the coherences in the system density matrix, i.e.

$$\hat{\rho} \mapsto \sum_i |a_i|^2|\psi_i\rangle\langle\psi_i|, \tag{3.5}$$

which is just eq. (3.2).
While illustrative, the above argument is of limited practical relevance, because we cannot keep track of all environmental degrees of freedom. Instead, let us focus exclusively on the system's density matrix, but allow it to evolve non-unitarily in time. Specifically, we are looking for a superoperator $\mathcal{L}$ satisfying

$$\dot{\hat{\rho}} = \mathcal{L}\hat{\rho}. \tag{3.6}$$

To that end, we first make the *Markov approximation* and assume that the environment is memoryless at relevant timescales. This means that self-correlations present in the environment decay faster than the system of interest undergoes significant changes [60]. In addition, we suppose that the coupling between system and environment is weak enough such that the density matrix of the environment can be taken to be approximately constant and that the system and the environment remain separable [60]. It can then be shown that the time evolution of $\hat{\rho}$ takes the form of a Lindblad master equation[1] [60],

$$\dot{\hat{\rho}} = -\frac{i}{\hbar}\left[\hat{H}, \hat{\rho}(t)\right] + \sum_i \left(\hat{L}_i\hat{\rho}(t)\hat{L}_i^\dagger - \frac{1}{2}\left\{\hat{L}_i^\dagger\hat{L}_i, \hat{\rho}(t)\right\}\right), \tag{3.7}$$

which only depends on the instantaneous density matrix. A derivation of eq. (3.7) is outside the scope of this thesis and can be found elsewhere, e.g. in ref. [60].
We conclude by arguing that the jump operators $\hat{L}_i$ give rise to decoherence. Writing down the non-unitary part of eq. (3.7) explicitly for a Hermitian[2] jump operator of the form

$$\hat{L} = \sum_i \lambda_i|\psi_i\rangle\langle\psi_i|, \tag{3.8}$$

where $\lambda_i \in \mathbb{R}$, a straightforward calculation yields [59]

$$\dot{\rho}_{kl}\big|_{\text{non-unitary}} = -\frac{1}{2}(\lambda_k - \lambda_l)^2\rho_{kl}, \tag{3.9}$$

i.e. an exponential decay of the off-diagonal matrix elements. In the above equation, $\rho_{kl} = \langle\psi_k|\hat{\rho}|\psi_l\rangle$.

3.2 Master Equation for Ro-translational Cavity Cooling

We are now left with the task to identify the jump operators relevant to our system in order to write down the master equation and find an expression for the spatio-orientational localization rate (see sec. 3.3). Apart from the cavity decay, which is accounted for by the jump operator $\hat{L}_{\text{cav}} = \sqrt{\kappa}\hat{a}$ [61], we need to consider collisions with residual gas, Rayleigh scattering of tweezer photons and the scattering, emission and absorption of thermal photons.

[1] This is a special case of the more general Born-Markov master equation. It turns out, however, that the latter can always be written in the form of eq. (3.7) if one applies the rotating wave approximation [60].

[2] Assuming hermiticity is not a requirement for the conclusion to hold, but gives a more compact result.

3.2.1 Gas Collisions

The Lindblad operators pertaining to gas collisions may be inferred from the monitoring approach to decoherence [62], which is based on the assumption that "probe particles" colliding with the test particle at random times induce a fictitious measurement process. Alongside a correction to the system energy, which we will ignore in the following, this gives rise to incoherent evolution [63]. Denoting by $\mathbf{Q}$ the momentum transfer, by $\mathbf{p}$ the momentum of the test (or *tracer*) particle, by $\mathbf{r}$ its coordinates and by $\mathbf{p}_{\text{gas}}$ the momentum of the gas particle, it can be shown [63] that the resulting jump operators have the form

$$\hat{L}_{\mathbf{Q},\mathbf{p}_{\text{gas}}} = e^{i\mathbf{Q}\cdot\hat{\mathbf{r}}/\hbar}\hat{L}(\mathbf{p}_{\text{gas}},\mathbf{p};\mathbf{Q}), \tag{3.10}$$

where $e^{i\mathbf{Q}\cdot\hat{\mathbf{r}}}$ is just the translation operator in momentum space,

$$e^{i\mathbf{Q}\cdot\hat{\mathbf{r}}/\hbar}|\mathbf{p}\rangle = |\mathbf{p}+\mathbf{Q}\rangle, \tag{3.11}$$

and $\hat{L}(\mathbf{p}_{\text{gas}},\mathbf{p};\mathbf{Q})$ is a complicated expression [63, 64],

$$\begin{aligned}\hat{L}(\mathbf{p}_{\text{gas}},\mathbf{p};\mathbf{Q}) = \sqrt{\frac{n_{\text{gas}}m_{\text{gas}}}{Qm_*^2}}\mu\left(\mathbf{p}_{\text{gas},\perp\mathbf{Q}} + \left(1+\frac{m_{\text{gas}}}{m}\right)\frac{\mathbf{Q}}{2} + \frac{m_{\text{gas}}}{m}\hat{\mathbf{p}}_{\parallel\mathbf{Q}}\right)^{1/2} \\ \cdot f\left(\text{rel}(\mathbf{p}_{\text{gas},\perp\hat{\mathbf{Q}}},\hat{\mathbf{p}}_{\perp\mathbf{Q}}) - \frac{\mathbf{Q}}{2}, \text{rel}(\mathbf{p}_{\text{gas},\perp\mathbf{Q}},\hat{\mathbf{p}}_{\perp\mathbf{Q}}) + \frac{\mathbf{Q}}{2}\right),\end{aligned} \tag{3.12}$$

which incorporates the details of the scattering process and involves the gas number density n_{gas}, the mass of the gas particles m_{gas}, the reduced mass $m_* = m\cdot m_{\text{gas}}/(m+m_{\text{gas}})$, the momentum distribution of the gas $\mu(\mathbf{p})$, the elastic scattering amplitude $f(\mathbf{p}_f,\mathbf{p}_i)$ from an initial momentum $\mathbf{p}_i$ to a final momentum $\mathbf{p}_f$ as well as the components of the momenta orthogonal and parallel to $\mathbf{Q}$, $\mathbf{p}_{\perp\mathbf{Q}}$ and $\mathbf{p}_{\parallel\mathbf{Q}}$, respectively. The relative momentum $\text{rel}(\mathbf{p}_{\text{gas}},\mathbf{p})$ is defined as $\text{rel}(\mathbf{p}_{\text{gas}},\mathbf{p}) = (m\mathbf{p}_{\text{gas}} - m_{\text{gas}}\mathbf{p})/(m+m_{\text{gas}})$ [64].
Relevant to our experiment is the limit $m_{\text{gas}}/m \to 0$, since our particles are more massive than the molecules of the surrounding air by many orders of magnitude. In that case, the recoil of the test particle upon a gas collision can be neglected, $m_* \approx m_{\text{gas}}$ and $\text{rel}(\mathbf{p}_{\text{gas}},\mathbf{p}) \approx \mathbf{p}_{\text{gas}}$. Eq. (3.12) hence simplifies to [64]

$$\hat{L}(\mathbf{p}_{\text{gas}},\mathbf{p};\mathbf{Q}) \approx \sqrt{\frac{n_{\text{gas}}}{Qm_{\text{gas}}}}\mu\left(\mathbf{p}_{\text{gas},\perp\mathbf{Q}} + \frac{\mathbf{Q}}{2}\right)^{1/2} f\left(\mathbf{p}_{\text{gas},\perp\mathbf{Q}} - \frac{\mathbf{Q}}{2}, \mathbf{p}_{\text{gas},\perp\mathbf{Q}} + \frac{\mathbf{Q}}{2}\right). \tag{3.13}$$

Intuitively, eq. (3.10) describes the displacement of the test particle in momentum space upon a collision with a gas particle multiplied by the (operator-valued) rate at which the gas particle is scattered from an initial momentum $\mathbf{p}_{\text{gas},\perp\mathbf{Q}} + \mathbf{Q}/2$ to $\mathbf{p}_{\text{gas},\perp\mathbf{Q}} - \mathbf{Q}/2$. Note that eq. (3.13) does not depend on $\mathbf{p}$ anymore and that $\mathbf{p}_{\text{gas},\perp\mathbf{Q}}$ is conserved during the collision. We will see in sec. 3.3 how this gives rise to localization in position.
The Lindblad operator follows from eqs. (3.7) and (3.10) by integration over all momentum transfers and gas momenta in the plane perpendicular to $\mathbf{Q}$ [63], i.e.

$$\mathcal{L}_{\text{gas}} = \int \mathrm{d}\mathbf{Q}\int_{\mathbf{Q}_\perp}\mathrm{d}\mathbf{p}_{\text{gas}}\left(\hat{L}_{\mathbf{Q},\mathbf{p}_{\text{gas}}}\hat{\rho}\hat{L}^\dagger_{\mathbf{Q},\mathbf{p}_{\text{gas}}} - \frac{1}{2}\left\{\hat{L}^\dagger_{\mathbf{Q},\mathbf{p}_{\text{gas}}}\hat{L}_{\mathbf{Q},\mathbf{p}_{\text{gas}}},\hat{\rho}\right\}\right). \tag{3.14}$$

We would typically assume a Maxwell-Boltzmann distribution for the gas momenta. The exact form of the scattering amplitude depends on the type of potential one takes as a basis for the interaction (e.g. Van der Waals, hard sphere, charge-dipole, dipole-dipole etc.) and will not be treated in further detail here due to its limited relevance to the experiment.

3.2.2 Scattering of Tweezer Photons

Let us now investigate the effect of Rayleigh scattering of photons from the trapping beam. We assume that the incident wave is a plane wave[3], which is polarized in the $\boldsymbol{\epsilon}_{\text{tw}}$-direction, i.e. $\mathbf{E}_{\text{in}} = \boldsymbol{\epsilon}_{\text{tw}} E_{\text{tw}} e^{i\mathbf{k}\cdot\mathbf{r}}$. In the far-field limit, the electric field $\mathbf{E}_{\text{rad}}$ scattered by the particle is a spherical wave of the form

$$\mathbf{E}_{\text{rad}}(\mathbf{r}) = E_{\text{tw}} \frac{e^{i\mathbf{k}'\cdot\mathbf{r}}}{r} \mathbf{f}(\mathbf{k}', \mathbf{k}; \Omega), \tag{3.15}$$

where $\mathbf{k} = k\mathbf{n}$ and $\mathbf{k}' = k'\mathbf{n}'$ denote, respectively, the wave vectors of the incoming and scattered beams, and $|\mathbf{k}| = |\mathbf{k}'|$.
Comparing with eq. (2.44) and keeping in mind that the polarizability is a tensorial quantity as we are dealing with geometrically anisotropic particles, we arrive at the expression for the scattering amplitude $\boldsymbol{f}(\mathbf{k}', \mathbf{k}; \Omega)$

$$\mathbf{f}(\mathbf{k}', \mathbf{k}; \Omega) = \frac{k^2}{4\pi\epsilon_0} (\boldsymbol{n}' \times \boldsymbol{\alpha}(\Omega)\boldsymbol{\epsilon}_{\text{tw}}) \times \boldsymbol{n}' = \frac{k^2 \alpha_{\mathbf{p}}(\Omega)}{4\pi\epsilon_0} (\mathbf{n}' \times \mathbf{m}_{\mathbf{p}}(\Omega)) \times \mathbf{n}', \tag{3.16}$$

where $\mathbf{m}_{\mathbf{p}}(\Omega) = \boldsymbol{\alpha}(\Omega)\boldsymbol{\epsilon}_{\text{tw}}/\alpha_{\mathbf{p}}(\Omega)$ is the normalized polarization vector inside the dielectric.
Just like gas collisions, the scattering of photons displaces the state of the particle in momentum space. Multiplying the corresponding operator by the scattering amplitude and the square root of the incident photon flux $I_{\text{tw}}/(\hbar\omega)$ yields the sought-after jump operators for photon scattering [65]

$$\hat{B}_{\mathbf{k}'s'} = \sqrt{\frac{I_{\text{tw}}}{\hbar\omega}} e^{-i\Delta\mathbf{k}\cdot\hat{\mathbf{r}}} \boldsymbol{\epsilon}'_{s'} \cdot \mathbf{f}(\mathbf{k}', \mathbf{k}; \Omega), \tag{3.17}$$

where $\Delta\mathbf{k} = k(\mathbf{n}' - \mathbf{n})$ and $\boldsymbol{\epsilon}'_{s'}$ ($s' \in \{1, 2\}$) are the two orthogonal polarizations of the scattered radiation.
The tweezer photons are (to a good approximation) characterized by a sharp momentum distribution, i.e. $\mu(\mathbf{p}) = \delta(\mathbf{p} - \hbar\mathbf{k})$. Obtaining the total Lindblad operator still requires us to sum over the two polarization states and integrate over all propagation directions of the scattered wave. We hence obtain

$$\mathcal{L}_{\text{tw}} = \sum_{s' \in \{1,2\}} \int \mathrm{d}^2\mathbf{n}' \left(\hat{B}_{\mathbf{k}'s'} \hat{\rho} \hat{B}^\dagger_{\mathbf{k}'s'} - \frac{1}{2} \left\{ \hat{B}^\dagger_{\mathbf{k}'s'} \hat{B}_{\mathbf{k}'s'}, \hat{\rho} \right\} \right). \tag{3.18}$$

It is worth emphasizing that this decoherence channel obviously disappears when the particle is left to evolve freely with the trap switched off. However, residual light inside the cavity (due to the finite decay time) would give rise to a similar effect, albeit with enhanced scattering along the cavity axis (cf. sec. 2.2.2) and incident flux from both directions along the cavity axis.

3.2.3 Absorption, Scattering and Emission of Thermal Photons

The scattering of thermal photons can be treated in an analogous way as explained in the previous section. The main difference is that thermal photons impinge on the test particle isotropically and are distributed over a wide frequency range with the average occupation number at temperature T given by [60]

$$\langle n(k) \rangle = \frac{2}{e^{\frac{\hbar c k}{k_B T}} - 1}. \tag{3.19}$$

In addition, we need to take the wavelength-dependence of the polarizability into account, i.e. $\alpha_{\mathbf{p}}(\Omega) = \alpha_{\mathbf{p}}(k, \Omega)$. Integrating over all outgoing directions and averaging over all incident

[3] This is a valid approximation near the focus of the (Gaussian) tweezer beam as long as the finite extent of the field can be disregarded.

directions, polarization directions and wavenumbers, we get the expression for the Lindblad operator [66]

$$\mathcal{L}_{\text{scatt}} = \frac{c}{2} \sum_{s,s' \in \{1,2\}} \int_{S_2} \int_{S_2} \mathrm{d}^2\mathbf{n}' \, \mathrm{d}^2\mathbf{n} \int_0^\infty \mathrm{d}k \, k^2 \langle n(k) \rangle \left(\hat{S}_{\mathbf{k}\mathbf{k}'ss'} \hat{\rho} \hat{S}^\dagger_{\mathbf{k}\mathbf{k}'ss'} - \frac{1}{2} \left\{ \hat{S}^\dagger_{\mathbf{k}\mathbf{k}'ss'} \hat{S}_{\mathbf{k}\mathbf{k}'ss'}, \hat{\rho} \right\} \right), \tag{3.20}$$

where

$$\hat{S}_{\mathbf{k}\mathbf{k}'ss'} = e^{-i\Delta\mathbf{k}\cdot\hat{\mathbf{r}}} \boldsymbol{\epsilon}'_{s'} \cdot \mathbf{f}(\mathbf{k}', \mathbf{k}, \boldsymbol{\epsilon}_s; \Omega). \tag{3.21}$$

The actual photon distribution may deviate significantly from eq. (3.19) due to the finite emissivity of the surrounding walls. However, it may still serve as an indicator for the relevant wavelength range.

Similarly, absorption of thermal radiation gives rise to momentum kicks of $\hbar\mathbf{k}$. We may hence define the respective jump operator [67]

$$\hat{A}_{\mathbf{k}} = e^{i\mathbf{k}\cdot\hat{\mathbf{r}}}, \tag{3.22}$$

from which the Lindblad operator follows again by averaging over all incident directions and wavenumbers[4] as

$$\mathcal{L}_{\text{abs}} = c \int_{S_2} \mathrm{d}^2\mathbf{n} \int_0^\infty \mathrm{d}k \, k^2 \langle n(k) \rangle \sigma_{\text{abs}}(k) \left[\hat{A}_{\mathbf{k}} \hat{\rho} \hat{A}^\dagger_{\mathbf{k}} - \frac{1}{2} \left\{ \hat{A}^\dagger_{\mathbf{k}} \hat{A}_{\mathbf{k}}, \hat{\rho} \right\} \right], \tag{3.23}$$

where the absorption cross section σ_{abs} is given by [67]

$$\sigma_{\text{abs}}(k) = \frac{k}{\epsilon_0} \mathrm{Im}[\alpha(k)]. \tag{3.24}$$

At room temperature, the peak of the blackbody emission spectrum is at a wavelength of about 10µm. In this regime, the absorptivity of SiO_2 is substantial and we hence assume absorption of thermal photons to constitute a significant decoherence source.

A similar reasoning applies to the emission of thermal photons, in which case the particle receives a momentum kick of $-\hbar\mathbf{k}'$. In complete analogy to before, the jump operator now reads

$$\hat{E}_{\mathbf{k}'} = e^{-i\mathbf{k}'\cdot\hat{\mathbf{r}}} \tag{3.25}$$

and, consequently, the Lindblad operator

$$\mathcal{L}_{\text{em}} = \frac{c}{(2\pi)^3} \int_{S_2} \mathrm{d}^2\mathbf{n}' \int_0^\infty \mathrm{d}k \, k^2 \langle n(k) \rangle \sigma_{\text{em}}(k) \left[\hat{E}_{\mathbf{k}'} \hat{\rho} \hat{E}^\dagger_{\mathbf{k}'} - \frac{1}{2} \left\{ \hat{E}^\dagger_{\mathbf{k}'} \hat{E}_{\mathbf{k}'}, \hat{\rho} \right\} \right]. \tag{3.26}$$

While we may equate the particle's emission cross section σ_{em} with its absorption cross section σ_{abs}, we need to bear in mind that it is much hotter than its environment. This changes the number distribution, eq. (3.19), to $\langle n(k) \rangle = 2\exp(-\hbar ck/(k_{\text{B}}T))$ [68], which significantly reduces the probability of occupying low-energy modes. In addition, the factor of $1/(2\pi)^3$ accounts for the mode density. SiO_2 is virtually transparent across a broad frequency range from UV to mid-infrared and we do hence not expect significant contributions from thermal emission at wavelengths below 5µm.
Additional uncertainties concern possible surface effects and the potential non-uniformity of the temperature distribution. If the particle is unevenly heated in the optical trap, one may define an effective temperature [69]

$$T_{\text{eff}} = \left(\frac{1}{V} \int_V \mathrm{d}^3\mathbf{r} \, T^4(\mathbf{r}) \right)^{1/4}, \tag{3.27}$$

[4] Note that polarization does not play a role here.

which corresponds to the total emission spectrum. Locally, however, the emitted radiation might have a rather different distribution, which would lead to an anisotropy in the emission pattern, potentially allowing one to distinguish between particle orientations
Yet, we do not believe that this is an issue in our setup, since our particles are significantly smaller than the waist of the trapping beam, which we hence assume to heat our particles evenly [70].

3.3 Spatio-orientational Localization Rate

We will now examine how the master equation, eq. (3.7), is connected to the rate at which the various decoherence channels give rise to localization in position and orientation. We have already mentioned in sec. 3.1 that the coherences decay exponentially with time as expressed by the differential equation [65]

$$\dot{\rho}(\mathbf{r}\Omega, \mathbf{r}'\Omega'; t)\big|_{\text{non-unitary}} = \langle \mathbf{r}\Omega | \mathcal{L}\rho | \mathbf{r}'\Omega' \rangle = -\Lambda(\mathbf{r}\Omega, \mathbf{r}'\Omega')\rho(\mathbf{r}\Omega, \mathbf{r}'\Omega'; t), \tag{3.28}$$

where $\rho(\mathbf{r}\Omega, \mathbf{r}'\Omega'; t) = \langle \mathbf{r}\Omega | \hat{\rho}(t) | \mathbf{r}'\Omega' \rangle$. Note that if the environment exhibits spherical symmetry, the localization rate can only depend on the absolute distance of the orientations and positions [60, 66]. This may be assumed, for example, as far as collisions with air molecules are concerned, but not for scattering of tweezer photons,
Putting together eqs. (3.7) and (3.28), we can readily establish the relation between decoherence and the Lindblad master equation as

$$\dot{\rho}(\mathbf{r}\Omega, \mathbf{r}'\Omega'; t)\big|_{\text{non-unitary}} = \sum_i \langle \mathbf{r}\Omega | \hat{L}_i \hat{\rho} \hat{L}_i^\dagger - \frac{1}{2} \left\{ \hat{L}_i^\dagger \hat{L}_i, \hat{\rho} \right\} | \mathbf{r}'\Omega' \rangle. \tag{3.29}$$

For scattering of gas molecules, the form of the jump operators, eq. (3.10), implies that the decoherence rate Λ is given by the expression

$$\begin{aligned} \Lambda = \frac{n_{\text{gas}}}{m_{\text{gas}}} \int \frac{\mathrm{d}\mathbf{Q}}{Q} \int_{\mathbf{Q}_\perp} \mathrm{d}\mathbf{p}_{\text{gas}}\, \mu\left(\mathbf{p}_{\text{gas}} + \frac{\mathbf{Q}}{2}\right) \Bigg[& \frac{1}{2} \left| f_\Omega\left(\mathbf{p}_{\text{gas},\perp\mathbf{Q}} - \frac{\mathbf{Q}}{2}, \mathbf{p}_{\text{gas},\perp\mathbf{Q}} + \frac{\mathbf{Q}}{2}\right)\right|^2 \\ & + \frac{1}{2} \left| f_{\Omega'}\left(\mathbf{p}_{\text{gas},\perp\mathbf{Q}} - \frac{\mathbf{Q}}{2}, \mathbf{p}_{\text{gas},\perp\mathbf{Q}} + \frac{\mathbf{Q}}{2}\right)\right|^2 \\ & - e^{-i\mathbf{Q}\cdot(\mathbf{r}'-\mathbf{r})} f_\Omega\left(\mathbf{p}_{\text{gas},\perp\mathbf{Q}} - \frac{\mathbf{Q}}{2}, \mathbf{p}_{\text{gas},\perp\mathbf{Q}} + \frac{\mathbf{Q}}{2}\right) f^*_{\Omega'}\left(\mathbf{p}_{\text{gas},\perp\mathbf{Q}} - \frac{\mathbf{Q}}{2}, \mathbf{p}_{\text{gas},\perp\mathbf{Q}} + \frac{\mathbf{Q}}{2}\right) \Bigg], \end{aligned} \tag{3.30}$$

where the orientational degrees of freedom are accounted for by an angular dependence of the scattering amplitude [66] that appears in eq. (3.13). Eq. (3.30) reduces to eq. (93) in ref. [63] if the scattering amplitude does not depend on Ω.
The remaining decoherence rates are obtained in an analogous fashion. As illustrative examples, let us write down the ones pertaining to scattering of thermal radiation in the cases where, respectively, only the orientational or only the translational degrees of freedom are relevant. Using eq. (3.20), we get in the former case [66]

$$\Lambda = \frac{c}{4} \sum_{s,s' \in \{1,2\}} \int_{S_2} \int_{S_2} \mathrm{d}^2\mathbf{n}\, \mathrm{d}^2\mathbf{n}' \int_0^\infty \mathrm{d}k\, k^2 \langle n(k) \rangle \left| \boldsymbol{\epsilon}'_{s'} \cdot \left[\mathbf{f}(\mathbf{k}', \mathbf{k}, \boldsymbol{\epsilon}_s; \Omega) - \mathbf{f}^*(\mathbf{k}', \mathbf{k}, \boldsymbol{\epsilon}_s; \Omega') \right] \right|^2, \tag{3.31}$$

which has an intuitive interpretation in that the decoherence becomes stronger the more discriminable the scattering amplitudes are in the respective orientations. Likewise, in the second scenario, we have [66]

$$\Lambda = \frac{c}{2} \sum_{s,s' \in \{1,2\}} \int_{S_2} \int_{S_2} \mathrm{d}^2\mathbf{n}\, \mathrm{d}^2\mathbf{n}' \int_0^\infty \mathrm{d}k\, k^2 \langle n(k) \rangle \left(1 - e^{-i\Delta\mathbf{k}\cdot(\mathbf{r}'-\mathbf{r})}\right) \left| \boldsymbol{\epsilon}'_{s'} \cdot \mathbf{f}(\mathbf{k}', \mathbf{k}, \boldsymbol{\epsilon}_s) \right|^2. \tag{3.32}$$

It can be shown [60] that under the assumption of an ideal blackbody spectrum, the translational decoherence rate due to scattering of thermal photons scales with V^2T^9, highlighting the potential benefit in cryogenically cooling the environment. The orientational localization rate exhibits "only" a scaling with T^7 [66], which can make orientational superpositions an appealing alternative to spatial ones in a high-temperature environment.
To conclude the discussion, let us take another look at eq. (3.32). In the limit of very short (de Broglie-) wavelengths $\lambda_{\text{db}} = h/p$ as compared to the size of the spatial superposition, the phase factor does not contribute to the integral as it oscillates too rapidly. In that case, the localization rate is simply equal to the scattering rate and does not increase further with growing separation. This is called the *short-wavelength limit* [60]. Conversely, in the *long wavelength limit*, a single scattering event cannot fully resolve the particle's position and the respective decoherence rate scales with the square of the separation [60].
An ellipsoid that is orientationally delocalized by an angle of $\pi/2$ around an axis perpendicular to the longest half-axis a_1 has a tip-to-tip spatial separation of $\sqrt{2}a_1$. Setting $a_1 \approx 50$nm, the short wavelength limit applies, for example, to decoherence by collisions with ambient gas molecules due to their notably short de Broglie wavelength in the pm range.

3.4 Heating Mechanisms

In the previous section, we have described the dominant decoherence factors. Now we will take a closer look at the various heating mechanisms that we need to overcome in order to be able to prepare our system close to the ground state.
The rate of change in the mean phonon number obeys the equation [71]

$$\frac{\mathrm{d}}{\mathrm{d}t}\langle n\rangle = -\Gamma\langle n\rangle + \gamma_{\text{heat}}, \tag{3.33}$$

where γ_{heat} denotes the heating rate, i.e. the rate at which phonons are introduced into the system. In a steady state, the heating rate is proportional to the damping,

$$\gamma_{\text{heat}} = \langle n_0\rangle\Gamma \tag{3.34}$$

with the stationary mean phonon number $\langle n_0\rangle$. The system hence dissipates energy until heating and damping equilibrate. We have already said in sec. 2.1 that the final energy of the system is proportional to the area underneath the motional PSD, which, in turn, is the sum of the individual PSDs pertaining to each type of perturbance in the system. We will now quantify those contributions and discuss their origin.
To that end, we need to introduce photonic and mechanical noise operators $\hat{a}_{\text{in}}$ and $\hat{b}_{\text{in}}$, respectively, in accordance with the textbook formalism for the quantum Langevin equation [72]. They are essentially the operator analogue to the classical stochastic force encountered in eq. (2.1) and pertain to an external heat bath to which the system of interest is coupled. While we rather carelessly disregarded these operators in sec. 2, we now need to take them into account as they contain the correlations that explain the connection between the noise present in the system and the phononic occupation number.
In particular, we can make the Markovian approximation and assume delta-correlated mechanical input noise [73], which is justified when the relaxation time of the system is much larger than the relaxation time of the environment[5], i.e.

$$\langle \hat{b}^\dagger_{\text{in}}(t)\hat{b}_{\text{in}}(s)\rangle = n_b\delta(t-s), \tag{3.35}$$

where n_b is the occupation number of the thermal bath. In Fourier space, the above relation can be shown to read [73]

$$\langle \hat{\tilde{b}}^\dagger_{\text{in}}(\Omega)\hat{\tilde{b}}_{\text{in}}(\Omega')\rangle = n_b\delta(\Omega+\Omega'). \tag{3.36}$$

[5] In view of the large Q-factors attained in levitated optomechanical systems, this is a reasonable assumption.

At pressures above 10^{-7}mbar, the dominant contribution to the mechanical noise comes from gas damping, which we will now investigate.

3.4.1 Gas Damping

We assume that the motion of our particle is in thermal equilibrium with its surroundings, i.e. that there is no net flow of energy between the environment and the system. The thermal occupation of a mechanical modes of a given frequency Ω_0 is then specified by the temperature of the ambient gas T according to the familiar relation

$$\langle n \rangle = \frac{k_B T}{\hbar \Omega_0}. \tag{3.37}$$

We may then apply the fluctuation-dissipation theorem to relate the thermal damping rate Γ_{th} to the corresponding stochastic force F_{th}. Its autocorrelation function reads[6] [74]

$$\langle F_{\text{th}}(t) F_{\text{th}}(t') \rangle = 2\Gamma_{\text{th}} m k_{\text{B}} T \delta(t - t'). \tag{3.38}$$

We are only interested in the free molecular regime, in which the mean free path of the air molecules is large compared to our particle's characteristic length.[7] Under that condition, the damping rate that a spherical particle[8] experiences is proportional to the pressure p [76],

$$\Gamma = \frac{64}{3} \frac{p r^2}{m \bar{v}}. \tag{3.39}$$

Introducing the universal gas constant R and the molar mass of air M, the mean velocity of the gas $\bar{v}$ is given by

$$\bar{v} = \sqrt{\frac{8RT}{\pi M}}. \tag{3.40}$$

Fourier transforming eq. (3.38) yields a flat force PSD,

$$S_{FF}^{\text{th}}(\Omega) = S_{FF}^{\text{th}} = 2\Gamma_{\text{th}} m k_B T. \tag{3.41}$$

By virtue of eq. (2.11), the thermal contribution to the motional PSD reads

$$S_{zz}^{\text{th}}(\Omega) = \frac{k_B T}{m} \frac{2\Gamma_{\text{th}}}{(\Omega_z^2 - \Omega^2)^2 + \Gamma_{\text{th}}^2 \Omega^2}. \tag{3.42}$$

The procedure to integrate eq. (3.42) is outlined in ref. [77] and we only state the result

$$\frac{1}{2\pi} \int_{-\infty}^{\infty} \mathrm{d}\Omega \, S_{zz}^{\text{th}}(\Omega) = \frac{k_B T}{m \Omega_z^2}, \tag{3.43}$$

which does not depend on the pressure of the gas or the size of the particles. The maximum of the PSD, which occurs at $\Omega = \pm\Omega_z$, however, does scale with $1/\Gamma$ and hence with $1/p$. So, while the total thermal occupation stays constant (as it should according to the equipartition theorem), the PSD becomes more spread out as the pressure is reduced and the phononic occupation around the spectral peak at the resonance frequency becomes smaller.

[6] The delta-like correlation is, of course, an approximation, which accounts for the the large number of collisions on the timescale of the observation, rendering the environment effectively memoryless.

[7] At room temperature and a particle size of ∼100nm, this limit is already attained at modest pressures of a few tens of millibars.

[8] The corresponding rate for an ellipsoidal particle can be found with the help of surface integrals [75]. However, since the shape of the particles that can be efficiently cooled in all degrees of freedom by coherent scattering deviates only slightly from that of sphere, we expect eq. (3.39) to provide a suitable approximation.

The treatment thus far was purely classical. In the quantum domain, we must take the non-commutativity of the thermal noise operator into account. The Langevin equation for the mechanical mode operator in the absence of any coupling to photonic modes reads in Fourier space [73]

$$\hat{\tilde{b}}(\Omega) = -\frac{\sqrt{\Gamma}\hat{\tilde{b}}_{\text{in}}(\Omega)}{i(\Omega_z - \Omega) + \Gamma/2}, \tag{3.44}$$

from which the PSD for $\hat{\tilde{b}}(\Omega)$, $S_{bb}(\Omega)$, follows as

$$\begin{aligned} S_{bb}(\Omega) &= \int_{-\infty}^{\infty} \mathrm{d}\Omega' \, \langle \hat{\tilde{b}}^\dagger(\Omega)\hat{\tilde{b}}(\Omega')\rangle \\ &= \frac{\Gamma n_b}{(\Omega + \Omega_z)^2 + (\Gamma/2)^2}, \end{aligned} \tag{3.45}$$

where we used eq. (3.36). We can find $S_{b^\dagger b^\dagger}$ in an analogous way, which allows us to write down the expression for the PSD of the respective motional degree of freedom [73, 78],

$$\begin{aligned} S_{zz}(\Omega) &= z_{\text{zpf}}^2 \left(S_{bb}(\Omega) + S_{b^\dagger b^\dagger}(\Omega)\right) \\ &= z_{\text{zpf}}^2 \Gamma \left[\frac{n_b}{(\Omega + \Omega_z)^2 + (\Gamma/2)^2} + \frac{n_b + 1}{(\Omega - \Omega_z)^2 + (\Gamma/2)^2}\right]. \end{aligned} \tag{3.46}$$

Unlike the classical expression, eq. (3.46) is not symmetric with respect to frequency. Indeed, as one approaches the ground state, the Stokes peak (at the positive mechanical frequency) becomes more pronounced. This is the basis for *sideband asymmetry thermometry*, whereby one detects this imbalance as a sign for cooling down to the "quantum level". In particular, the negative frequency peak vanishes in the ground state, where $\langle n \rangle = 0$, as there are no more phonons to annihilate.

In the above treatment, we have neglected any possible accommodation of gas particles, i.e. we have assumed them to be reflected instantaneously and specularly upon impinging on the nanoparticle. This is, in fact, mostly not the case. For SiO_2 at room temperature, the larger part of the ambient gas is diffusely reflected as quantified by an accommodation coefficient of 0.77 [79]. This raises another complication as the gas particles can no longer be assumed to emerge from the particle at the same temperature as the impinging particles [70]. The (classical) thermal PSD of the center-of-mass motion, eq. (3.42), is hence modified to [70]

$$S_{zz}^{\text{th}}(\Omega) = \frac{k_B T_{\text{eff}}}{m} \frac{2\Gamma_{\text{eff}}}{(\Omega_z^2 - \Omega^2)^2 + \Omega^2 \Gamma_{\text{eff}}^2}, \tag{3.47}$$

where the effective temperature

$$T_{\text{eff}} = \frac{T_{\text{im}}\Gamma_{\text{im}} + T_{\text{em}}\Gamma_{\text{em}}}{\Gamma_{\text{em}} + \Gamma_{\text{im}}} \tag{3.48}$$

depends on the temperatures of the impinging an emerging gas particles T_{im} and T_{em}, respectively, as well as the associated damping rates Γ_{im} and Γ_{em}. The effective damping[9] is defined as [70]

$$\Gamma_{\text{eff}} = \Gamma_{\text{im}} + \Gamma_{\text{em}}. \tag{3.49}$$

Despite the negligible absorption of SiO_2 in the infrared, particle loss due to melting may occur as a result of small impurities alongside a large tweezer intensity and poor heat conductivity in mid- to high vacuum [70]. This substantiates the need to achieve a clean mode profile of the trapping beam in order to minimize the required optical power.

[9] Be aware that this "effective damping" has nothing to do with the one defined in eq. (2.74).

We may also invoke the fluctuation-dissipation theorem to relate the stochastic torque N_{th} acting on the particle to the thermal PSD. The analogue to eq. (3.38) reads [56]

$$\langle N_{\text{th}}(t)N_{\text{th}}(t')\rangle = 2\Gamma_{\text{th}} I k_B T \delta(t-t'), \tag{3.50}$$

with I denoting the moment of inertia. Equivalently to the discussion above, this equation leads to a thermal PSD of

$$S^{\text{th}}_{\gamma\gamma}(\Omega) = \frac{k_B T}{I\Omega^2}\frac{2\Gamma_{\text{th}}}{\Omega^2+\Gamma^2_{\text{th}}}, \tag{3.51}$$

where γ is some rotational degree of freedom. Eq. (3.51) holds e.g. for a particle that is rotationally accelerated around a well-defined axis inside a circularly polarized tweezer and hence decoupled from all other rotational degrees of freedom. The latter assumption does not hold for free motion. A more general treatment is outside the scope of this thesis and can be found e.g. in ref. [80].

3.4.2 Phase Noise

We have already mentioned that one of the main appeals of cooling by coherent scattering is the opportunity to avoid phase noise to a large extent. Indeed, the limit on the laser linewidth to achieve optomechanical cooling becomes more stringent in proportion to the number of photons inside the cavity [81] as we will now analyze.
Phase noise results from unavoidable spontaneous emission events inside the laser, which are characterized by random phases. After some time t, the sum of these individual contributions adds to the total phase of the light field according to [82]

$$\phi(t) = \phi_0 + \sum_i \frac{E^i_{\text{sp}}}{E_0}\sin\left(\phi^i_{\text{sp}}\right) = \phi_0 + \Delta\phi(t), \tag{3.52}$$

where E_0 and ϕ_0 are, respectively, the electric field amplitude of the laser beam and its phase in the absence of any perturbations, $E^i_{\text{sp}} \ll E_0$ is the field generated by the i-th spontaneously emitted photon and ϕ^i_{sp} is the corresponding phase. Since the spontaneous emission events are mutually independent and their number per unit time is large (with respect to reasonable sampling periods), the central limit theorem may be employed to demonstrate that the probability density function of the phase change acquired over a sufficiently large time interval approaches a Gaussian distribution [82]. It is unbiased in the sense that $\langle\Delta\phi(t)\rangle = 0$.
Phase fluctuations obviously do not play a role in trapping the particle, since we are then only interested in the average field. However, they are converted to amplitude and intensity noise inside a cavity [83]. To clarify this, let us suppose that the coherent amplitude α, which we defined in eq. (2.60)[10], features a time-dependent phase shift,

$$\alpha(t) = \alpha e^{i\phi(t)}. \tag{3.53}$$

It can be shown that as a consequence of the Gaussian nature of the noise process, the amplitude autocorrelation decays with time as [82]

$$\langle\alpha(t_2)\alpha^*(t_1)\rangle = |\alpha|^2 e^{-\Gamma_{\text{L}}|t_2-t_1|/2}. \tag{3.54}$$

According to eq. (2.10), this gives rise to a Lorentzian PSD, the width of which is just the laser linewidth Γ_{L},

$$S_{\alpha\alpha}(\Omega) = |\alpha|^2\frac{\Gamma_{\text{L}}}{\Omega^2+(\Gamma_{\text{L}}/2)^2}. \tag{3.55}$$

[10] We omit the tilde henceforth to avoid confusion with the Fourier transform. We also again operate within a frame of reference rotating at the trapping beam frequency, which is why the explicit time dependence of the coherent amplitude vanishes.

When the phase fluctuations are sufficiently small, we may expand the phase factor to first order, yielding [83]

$$\langle \alpha(t_2)\alpha^*(t_1)\rangle = |\alpha|^2\langle e^{i\phi(t_2)}e^{-i\phi(t_1)}\rangle \approx |\alpha|^2\left(1+\langle\phi(t_2)\phi(t_1)\rangle\right) \tag{3.56}$$

and, as a result,

$$S_{\alpha\alpha}(\Omega) = |\alpha|^2\left[2\pi\delta(\Omega)+S_{\phi\phi}(\Omega)\right]. \tag{3.57}$$

Eq. (3.56) only incorporates the instantaneous phase $\phi(t)$ and does not account for the change in detuning $\Delta \mapsto \Delta+\dot{\phi}$ and hence neither for the modulation of the coupling rate. The approximation is only valid if the variations in the phase occur over a timescale that is much larger than the cavity decay time [83], which we can safely assume as $\Gamma_\mathrm{L} \ll \kappa$ in our experimental setup.

We now again restrict ourselves to the motion along z. By virtue of eq. (2.60), assuming that the particle is located in an antinode of the cavity and approximating $\sqrt{\left(\frac{\kappa_\mathrm{eff}}{2}\right)^2+\Delta_\mathrm{eff}^2} \approx \Omega_\mathrm{z}$ [34], we can rewrite eq. (3.57) as

$$S_{\alpha\alpha}(\Omega) = \frac{E_\mathrm{d}^2}{\Omega_z^2}\left[2\pi\delta(\Omega)+S_{\phi\phi}(\Omega)\right]. \tag{3.58}$$

We may henceforth omit the term proportional to $\delta(\Omega)$ as we are only interested in the contribution in proximity to the mechanical resonance [73].

Let us now demonstrate that phase noise gives rise to a stochatic force on the particle that increases the mean phonon number by [84]

$$\langle n_\phi\rangle = S_{\dot{\phi}\dot{\phi}}(\Omega_z)\frac{|\alpha|^2}{\kappa_\mathrm{eff}}, \tag{3.59}$$

where $S_{\dot{\phi}\dot{\phi}}(\Omega_z)$ the frequency noise PSD at the mechanical frequency Ω_z. $S_{\dot{\phi}\dot{\phi}}$ is closely related to the phase noise PSD $S_{\phi\phi}$ by the relation $\Omega = \mathrm{d}\phi/\mathrm{d}t$, which gives [34]

$$S_{\dot{\phi}\dot{\phi}}(\Omega) = \Omega^2 S_{\phi\phi}(\Omega). \tag{3.60}$$

For the sake of the argument, we assume that phase noise is the only source of photonic noise.[11] The corresponding noise operators satisfy [73]

$$\langle \hat{\tilde{a}}_\mathrm{in}^\dagger(\Omega)\hat{\tilde{a}}_\mathrm{in}(\Omega')\rangle = \frac{\Omega_z^2}{\kappa_\mathrm{eff}}S_{\alpha\alpha}(\Omega)\delta(\Omega+\Omega'). \tag{3.61}$$

We have already seen in sec. 2.2.3 that the mechanical frequency, the detuning and the damping all shift due to the optomechanical interaction. In terms of these effective values Ω_eff, Δ_eff and Γ_eff, respectively, the Fourier transform of the mechanical mode operator (including the noise inputs) can be shown to read [73]

$$\begin{aligned}\hat{\tilde{b}}(\Omega) = &-\frac{\sqrt{\Gamma}\hat{\tilde{b}}_\mathrm{in}(\Omega)}{i(\Omega_\mathrm{eff}-\Omega)+\Gamma_\mathrm{eff}/2} + \frac{iG}{i(\Delta_\mathrm{eff}-\Omega)+\kappa_\mathrm{eff}/2}\frac{\sqrt{\kappa_\mathrm{eff}}\hat{\tilde{a}}_\mathrm{in}(\Omega)}{i(\Omega_\mathrm{eff}-\Omega)+\Gamma_\mathrm{eff}/2}\\ &+\frac{iG}{-i(\Delta_\mathrm{eff}+\Omega)+\kappa_\mathrm{eff}/2}\frac{\sqrt{\kappa_\mathrm{eff}}\hat{\tilde{a}}_\mathrm{in}^\dagger(\Omega)}{i(\Omega_\mathrm{eff}-\Omega)+\Gamma_\mathrm{eff}/2}.\end{aligned} \tag{3.62}$$

In our case, we have

$$G = E_\mathrm{d}kz_\mathrm{zpf}\mathrm{Re}(\boldsymbol{\epsilon}_\mathrm{cav}^*\cdot\boldsymbol{\epsilon}_\mathrm{tw})\sin(kz_0)+g_0\alpha\sin(2kz_0). \tag{3.63}$$

[11] The generalization to multiple noise sources is straightforward as it only requires the definition of the associated operators and the analysis of the correlations between them.

We may then use the input correlations, eqs. (3.36) and (3.61), to evaluate the PSD of the mechanical mode operator [73],

$$\begin{aligned} S_{bb}(\Omega) &= \int_{-\infty}^{\infty} \mathrm{d}\Omega' \, \langle \hat{b}^\dagger(\Omega)\hat{b}(\Omega')\rangle \\ &= \frac{\Gamma n_b}{(\Omega_{\text{eff}}+\Omega)^2 + (\Gamma_{\text{eff}}/2)^2} + \frac{|G|^2\kappa_{\text{eff}}\left[1+(\Omega_z^2/\kappa_{\text{eff}})S_{\alpha\alpha}(\Omega)\right]}{\left[(\Delta_{\text{eff}}-\Omega)^2+(\kappa_{\text{eff}}/2)^2\right]\left[(\Omega_{\text{eff}}+\Omega)^2+(\Gamma_{\text{eff}}/2)^2\right]} \\ &\quad + \frac{|G|^2\Omega_z^2 S_{\alpha\alpha}(\Omega)}{\left[(\Delta_{\text{eff}}+\Omega)^2+(\kappa_{\text{eff}}/2)^2\right]\left[(\Omega_{\text{eff}}+\Omega)^2+(\Gamma_{\text{eff}}/2)^2\right]}. \end{aligned} \tag{3.64}$$

According to eq. (3.46), the PSD of the z-motion is then given by

$$\begin{aligned} S_{zz}(\Omega) &= z_{\text{zpf}}^2 \left(S_{bb}(\Omega) + S_{b^\dagger b^\dagger}(\Omega)\right) \\ &= z_{\text{zpf}}^2 \left[\frac{1}{(\Omega_{\text{eff}}+\Omega)^2+(\Gamma_{\text{eff}}/2)^2} + \frac{1}{(\Omega_{\text{eff}}-\Omega)^2+(\Gamma_{\text{eff}}/2)^2}\right] \\ &\quad \cdot \left(\Gamma n_b + \frac{|G|^2\kappa_{\text{eff}}\left[1+(\Omega_z^2/\kappa_{\text{eff}})S_{\alpha\alpha}(\Omega)\right]}{(\Delta_{\text{eff}}-\Omega)^2+(\kappa_{\text{eff}}/2)^2} + \frac{|G|^2\Omega_z^2 S_{\alpha\alpha}(\Omega)}{(\Delta_{\text{eff}}+\Omega)^2+(\kappa_{\text{eff}}/2)^2}\right) \\ &\quad + z_{\text{zpf}}^2 \frac{\Gamma}{(\Omega_{\text{eff}}-\Omega)^2+(\Gamma_{\text{eff}}/2)^2}. \end{aligned} \tag{3.65}$$

Comparing with eq. (3.46), we see that the terms pertaining to the mechanical input noise operator are precisely the thermal contribution to the quantum PSD. Disregarding this part and evaluating the remaining one at $\Omega = \Omega_{\text{eff}} = \Delta_{\text{eff}}$ leaves us with

$$\begin{aligned} S_{zz}^{\text{phase}}(\Omega_{\text{eff}}) &= z_{\text{zpf}}^2 \left[\frac{1}{(2\Omega_{\text{eff}})^2+(\Gamma_{\text{eff}}/2)^2} + \frac{1}{(\Gamma_{\text{eff}}/2)^2}\right] \\ &\quad \cdot \left(\frac{|G|^2\left[1+(\Omega_z^2/\kappa_{\text{eff}})|\alpha|^2 S_{\phi\phi}(\Omega_{\text{eff}})\right]}{\kappa_{\text{eff}}/4} + \frac{|G|^2\Omega_z^2|\alpha|^2 S_{\phi\phi}(\Omega_{\text{eff}})}{(2\Omega_{\text{eff}})^2+(\kappa_{\text{eff}}/2)^2}\right). \end{aligned} \tag{3.66}$$

If we can additionally assume our system to be in the deeply sideband-resolved regime $\Omega_{\text{eff}} \gg \kappa_{\text{eff}}$[12], the equation simplifies further to

$$S_{zz}^{\text{phase}}(\Omega_{\text{eff}}) \approx z_{\text{zpf}}^2 \left[\frac{1}{(2\Omega_{\text{eff}})^2+(\Gamma_{\text{eff}}/2)^2} + \frac{1}{(\Gamma_{\text{eff}}/2)^2}\right] \frac{4|G|^2}{\kappa_{\text{eff}}} \left(1 + \frac{\Omega_z^2}{\kappa_{\text{eff}}}|\alpha|^2 S_{\phi\phi}(\Omega_{\text{eff}})\right). \tag{3.67}$$

Keeping in mind the relation between $S_{\phi\phi}$ and $S_{\dot{\phi}\dot{\phi}}$, eq. (3.60), the last term of the above equation is indeed proportional to eq. (3.59) as we wanted to show. In short, this result states that the phononic occupation number increases in proportion to the phase noise PSD $S_{\phi\phi}(\Omega)$ and the intracavity photon number $|\alpha|^2$, which, in turn, is maximal when the particle is placed in an antinode of the cavity (cf. eq. (2.60)).

3.4.3 Recoil Heating

Just like residual air molecules, photons also impart random momentum kicks to the particle, cf. sec. 3.2.2. The resulting recoil heating contributes significantly only at very low pressures, but will be the dominant factor in the regime below $\sim 10^{-7}$mbar [34]. To estimate its magnitude, we only need to take into account the scattering from the trapping beam. Despite the amplification of the scattered light by a factor of $\mathcal{F}/\pi$ inside the cavity, the fact that only a tiny fraction of the incoming light is scattered into the mode alongside the large ratio of the waists $w_0^2/(W_{x0}W_{y0}) \approx 10^5$ leads to an error at the sub-percent level.

[12] In our current setup, we only have $\Omega_{\text{eff}} > \kappa_{\text{eff}}$.

Recalling that the force exerted along the z-axis by the scattering of photons is just $F_z = P_z/c$, where P_z is the power scattered in the z-direction, the corresponding force PSD can be shown to read [85]

$$S_{FF}^{\text{rec}}(\Omega) = S_{FF}^{\text{rec}} = \frac{2}{5}\frac{\hbar\omega}{2\pi c^2}P_{\text{scatt}} \tag{3.68}$$

if z is perpendicular to the polarization axis and with the factor 2/5 replaced by 1/5 for the parallel direction. Note that even though the induced dipole does not radiate along its axis, the particle still feels a force in that direction, albeit only half as large. P_{scatt} denotes the total scattered power, which is given by eq. (2.42).
From eq. (2.11), the displacement PSD follows as

$$S_{zz}(\Omega) = \frac{2}{5}\frac{\hbar\omega}{2\pi m^2 c^2}\frac{P_{\text{scatt}}}{(\Omega_z^2 - \Omega^2)^2 + \Gamma^2\Omega^2}. \tag{3.69}$$

3.4.4 Displacement Noise

Finally, we need to mention displacement noise, which arises from fluctuations of the trapping center as a result of vibrations and may indeed render ground state cooling impossible if not mitigated [86]. The corresponding heating rate in terms of the motional PSD, which needs to be obtained experimentally, is given by [86]

$$\gamma_{\text{disp}} = \pi\frac{\Omega_z^2}{4z_{\text{zpf}}^2}S_{zz}(\Omega_z). \tag{3.70}$$

Eq. (3.70) exhibits a proportionality to $P_{\text{tw}}^{3/2}$, providing yet another reason why the optical trapping power needs to be limited even though the optomechanical coupling rate increases with larger tweezer intensity (cf. sec. 2.2.3).

Chapter 4

Experimental Realization

We will now provide a brief overview over the various tasks that we have been working on in preparation of ro-translational cooling. We will then explain our current experimental setup and discuss possible modifications that have yet to be implemented.

4.1 Experimental Steps

One of the more challenging experimental steps has proven to be the preparation of the optical tweezer in such a way that it allows to stably and reliably trap our particles. Secondly, we need to launch the latter in a clean and efficient manner, preferably under mid (or even high) vacuum conditions. Once a particle is captured, we must place it in the right position in the standing light wave of the cavity, which we have to lock to a suitably detuned frequency (cf. sec. 2.2.3). Finally, we need to keep track of the particle's motion employing various complementary detection schemes.

4.1.1 Trap Loading

A variety of mechanisms have been implemented by different groups to load optical traps, among them nebulization [34, 87], laser-induced acoustic desorption (LIAD) [88] and piezo loading [89]. Recently, direct loading through hollow-core fibers has also attracted interest [90]. Electrospray ionization (ESI) is another widely used technique to launch particles into the gas phase [91]. While typically applied for smaller species such as biomolecules, volatilization of nanoparticles in mass ranges up to GDa has also been demonstrated [92]. However, ESI produces highly charged ions and is thus more appropriate for use in combination with mass spectrometers or electrodynamic traps. As we will explain in further detail below, we have so far employed nebulization and LIAD in our setup.

Nebulization

Dispersing the particles in an aerosol is attractive because it is simple to implement and has proven to work reliably in our experiment. We use an ultrasonic nebulizer (Omron MicroAir U100), which creates ultrasonic sound waves by shaking a piezoelectric actuator. These waves subsequently travel to the surface of the colloidal particle solution, where they prompt the formation of droplets. A high frequency is generally favorable as it minimizes the droplet size [93]. A small droplet volume, in turn, lowers the probability of agglomeration and/or co-trapping of several nanoparticles at once.
We dilute the commercially available 100nm SiO_2-solution (Corpuscular), which comes at a concentration of 5%, in a ratio of 1:1000 in isopropanol, ultrasonicate it for 10 minutes to avoid agglomeration and fill about 5ml of the solution into the designated container. The nebulizer is

surrounded by a bell jar in which aerosol builds up within a few seconds upon switching on the device, leading to noticeable haze. We then manually open the valve connecting the bell jar and the vacuum chamber for about half a second to enable the inflow of gas [34].
This technique features some evident drawbacks. We estimate that we spray billions of particles into the chamber each time we open the valve. This would cause the cavity mirrors to get clogged immediately and – to a lesser extent – also degrade the tweezer lens over time. The large concentration of particles inside the chamber and their chaotic motion is also witnessed by the fact that we observe successful trapping even 10 minutes after turning off the source.
Moreover, particles can only be trapped once a sufficiently high pressure is attained. In practice, we capture no particles below 100mbar and find the largest success rate even above 500mbar. Trapping at lower pressures would, however, be preferable in order to avoid the risk of losing them while pumping down and because it would potentially allow us to instantly initiate feedback cooling, thereby reducing the experimental complexity.
While in particular the expected contamination of the optics prevents us from applying this technique systematically, we maintain that it allows us to quickly and reliably judge whether the quality and intensity of the tweezer beam suffice to trap particles.

Laser-Induced Acoustic Desorption

LIAD is a tempting alternative for launching nanoparticles as it is cleaner than the aforementioned nebulization in the sense that the particles are injected in a more directed manner, it works at lower pressures, does not add significant complexity to the setup and is also remarkably versatile. Indeed, it has already proven to work not only in desorbing inorganic nanoparticles [88] but also for biological particles in various size ranges from small amino acids [94], (functionalized) porphyrins [95] up to bacteria [96]. As visualized in fig. 4.1, the method works by irradiating an opaque, usually metallic foil, on which the particles are adsorbed, with short, intense laser pulses. In our case, we use 6ns pulses from a frequency-doubled Nd:YAG beam at a wavelength of 532nm and a pulse energy of a few mJ.
One major drawback of this technique is the fact that the particles may be ejected at high initial velocities within a range that appears to be strongly dependent on the type of foil [95]. Without complementary cavity cooling, particles launched by LIAD can only be optically trapped in the diffusive regime, i.e. if their motion is governed by random collisions with background gas rather than the directed expulsion from the substrate. Buffer gas cooling hence becomes a necessity. In addition, the alignment of the pulsed beam with respect to the tweezer is critical given that the particles can only be trapped within a region of a few μm^3 around its focus (cf. sec. 4.1.2).
While a systematic investigation of the relation between the particles' velocity distribution and the substance and thickness of the substrate has yet to be conducted, we expect that once available, these results will help us greatly in our endeavor to optimize the trapping efficiency.

To prepare the sample, we glue a piece of commercial aluminum foil, which has a thickness of about 15µm, onto a metallic frame with dimensions of 8x8mm, apply one to two droplets of the same particle solution that we have used for nebulization onto the substrate and let the solvent evaporate for about 15 minutes. We then insert the sample into a holder that is mounted on a SmarAct nanopositioning stage, which we can move along all three spatial axes.
The choice of foil was made for the purely pragmatic reason that we reliably obtained particle signals using it. Desorption from thicker aluminum foils (150 and 300µm) resulted in a significantly lower yield. We also tested Teflon-coated glass slides, but noticed that substantial amounts of Teflon fragments were ejected alongside our nanoparticles.

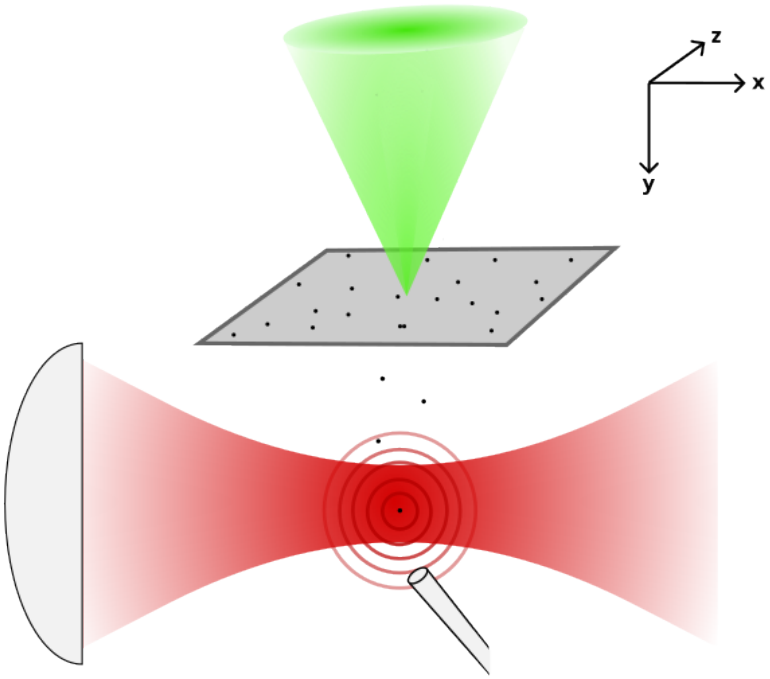

Figure 4.1: Sketch of laser-induced acoustic desorption (not to scale). The sample foil is irradiated with a focused 532nm laser pulse upon which particles are ejected and decelerated by ambient gas. Under the condition of adequate alignment and sufficient slowing, they are captured by the trapping beam and the scattered light is picked up by a multimode fiber.

So far, we have only witnessed successful trapping of particles when we placed the sample at a distance of about 7-7.5mm from the focus of the tweezer at a pressure of 15mbar.[1] This is rather peculiar, since our time-of-flight measurements conducted at around 10^{-4}mbar, where gas friction is virtually absent, point towards a mean initial velocity of 40m/s. If this were accurate, the particles would already thermalize after less than 700µm as is shown in fig. 4.2a.[2] The simulation is based on a simple elastic collision model and does not account for possible accommodation, i.e. any exchange of energy between the particle and the gas molecules. The damping rates Γ_{bg} obtained from an exponential fit of the curves shown in fig. 4.2b agree with the analytical expression [80]

$$\Gamma_{\mathrm{bg}} = \frac{8pr^2}{3m}\sqrt{\frac{2\pi m_{\mathrm{gas}}}{k_{\mathrm{B}}T}} \tag{4.1}$$

to within 5%.
It is not only crucial to carefully select the sample height to meet the required stopping distance, but also to avoid cutting off the highly divergent tweezer beam, as this would deteriorate the focus quality.

For practical reasons, we place the sample on top of the tweezer and irradiate it from above such that the particles are ejected in the downward direction. Given the short timescale of the particles' time-of-flight, which is on the order of hundreds of µs, we do not expect the gravitational force to affect the trapping probability in a significant way. Still, placing the tweezer focus on top of

[1] The cavity was not inserted while conducting these tests and we were thus able to freely choose the distance to the tweezer focus.

[2] The particles reach terminal velocities on the order of cm/s.

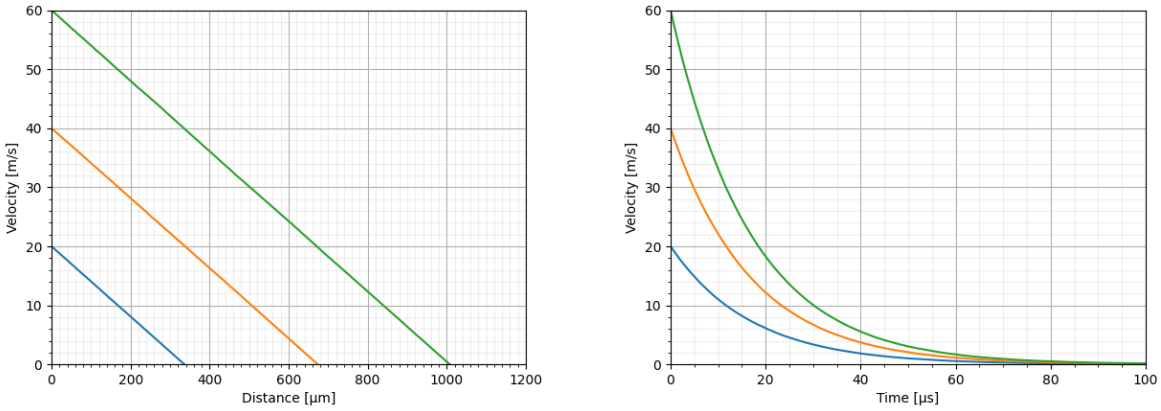

(a) (b)

Figure 4.2: Simulated velocities of SiO_2-particles with a diameter of 100nm as function of (a) distance from the sample and (b) flight time given initial velocities of 20m/s (blue), 40m/s (orange) and 60m/s (green) at a pressure of 15mbar.

the substrate and shooting from the bottom constitutes a viable alternative [29].

While we have succeeded in trapping particles at much lower pressures than what was feasible using the nebulization technique, the need for buffer gas cooling still makes LIAD incompatible with high vacuum. In addition, the particles' diffusive motion again raises the concern of contaminating the cavity mirrors. Indeed, preliminary trials indicate that the finesse may drop significantly after a few dozen to a hundred shots.
Depending on the trapping efficiency that we can ultimately attain, combining LIAD with the cavity might hence require us to spatially separate the trapping region from the latter. Once we have captured a particle, we would move the focus back to the intended position. We have already witnessed that our particles remain stably trapped when moving the lens back and forth at speeds of a few mm/s.

The exact mechanism by which the particles are eventually ejected from their substrate is not yet fully understood. Huang et al. [97], for example, deem an explanation based on the transfer of momentum from an acoustic shock wave incompatible with their experimental data and view it more in line with a surface stress model. Importantly, they found the laser fluence to not significantly affect the particles' forward velocity and observed that the expulsion events do not occur at a single instant in time but are temporally distributed [97].
The latter point in particular is remarkable because it means that velocity measurements based on the particles' time-of-flight (with respect to the laser pulse) need to be interpreted with care as they do not account for the delayed expulsion. This is all the more significant, the smaller the distance between the sample and the detection region. Consider, for example, the delay time distribution displayed in fig. 4.3. If the results were governed predominantly by the desorption time, this would cause us to underestimate the initial velocity and might hence provide an explanation for the discrepancy between the calculated aerodynamic stopping distance and the actual distance required to trap, which, as mentioned previously, appears to be several times larger in our setup.
Alternatively, one can calculate the particle velocity from its passage time through the tweezer, i.e. from the width of the corresponding peak in the scattering signal. The applicability of this method is, however, limited in our case as the beam's small Rayleigh length of approximately 2µm brings about a large measurement uncertainty. Still, if the time-of-flight measurement provided a reliable estimate of the initial velocity (which we can currently not assume for aforementioned reasons), comparing the average delay to the average flythrough time would allow us to narrow

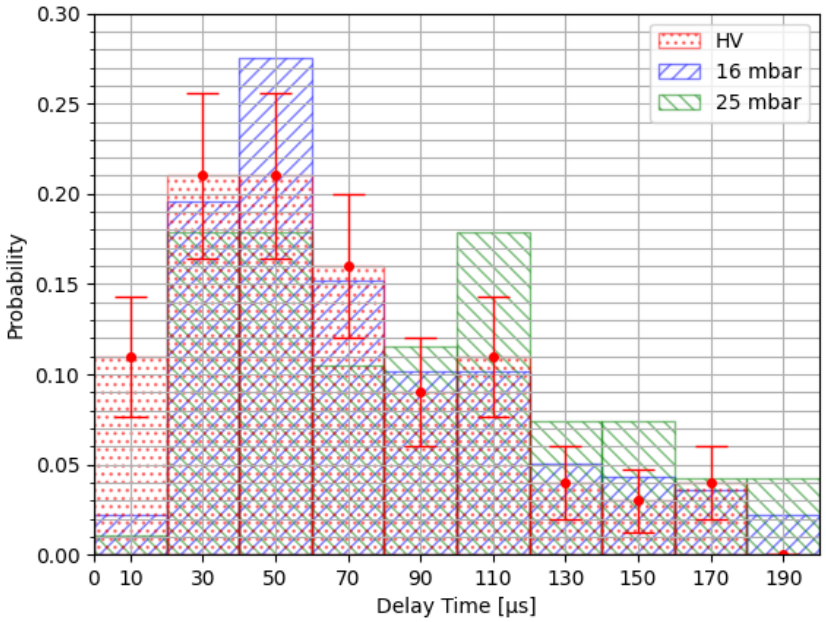

Figure 4.3: Distribution of the time delay between the LIAD pulse and the detection signal for 100nm SiO_2 particles desorbed from conventional aluminum foil at a sample distance of 2.5mm. The data are obtained from 100 detected events in high vacuum (red), 138 events at 16mbar (blue) and 95 events at 25mbar (green), respectively. For the sake of clarity, error bars are displayed only for the HV measurement.

down the range of distances from the focus at which the particles pass the tweezer and hence to exclude potential alignment errors.

The (actual) particle size is another possible source of error as we cannot entirely rule out the possibility of agglomeration despite the heavy dilution of the sample and the prior ultrasonification. In view of the fact that the damping rate scales linearly with the inverse of the particle diameter, cf. eq. (4.1), clusters would require a larger stopping distance at a given initial velocity. We seek to avoid misinterpretation by only taking signals into account that have a certain minimum prominence and distance from each other (in case there are more peaks in one trace) to filter out potentially anisotropic particles.

Lastly, we emphasize that we expect the ejected particles to carry a significant number of charges [98], which we have yet to characterize. In order to avoid interactions with stray fields, we possibly need to implement a neutralization mechanism [99]. While this would allow us to get rid of charges on the surface, an intrinsic dipole moment may remain, which can cause decoherence, cf. sec. 3.

4.1.2 Particle Trapping

We trap our particles using an optical tweezer as pioneered by Arthur Ashkin [100]. The electric field of the tightly focused laser beam induces a dipole moment in the dielectric, which consequently experiences a gradient force F_{grad} towards the point of the largest intensity, i.e.

$$\boldsymbol{F}_{\text{grad}} = -\nabla U_{\text{tw}}, \tag{4.2}$$

where U_{tw} was defined in eq. (2.25).
Particles inside an optical field are, however, also subject to non-conservative radiation pressure, which originates from the momentum transfer of photons that are either absorbed or scattered.

For our purposes, we may neglect the contribution due to absorption as silica features hardly any extinction in the near-infrared. As far as the contribution due to scattering is concerned, applying once again the Rayleigh approximation readily yields the expression for the radiation pressure force F_{rad}

$$F_{\text{rad}} = I_{\text{tw}} \sigma_{\text{scatt}} / c, \tag{4.3}$$

where σ_{scatt} is the scattering cross section integrated over the whole solid angle

$$\sigma_{\text{scatt}} = \frac{8\pi}{3} k^4 r^6 \left(\frac{n^2 - 1}{n^2 + 2} \right)^2 . \tag{4.4}$$

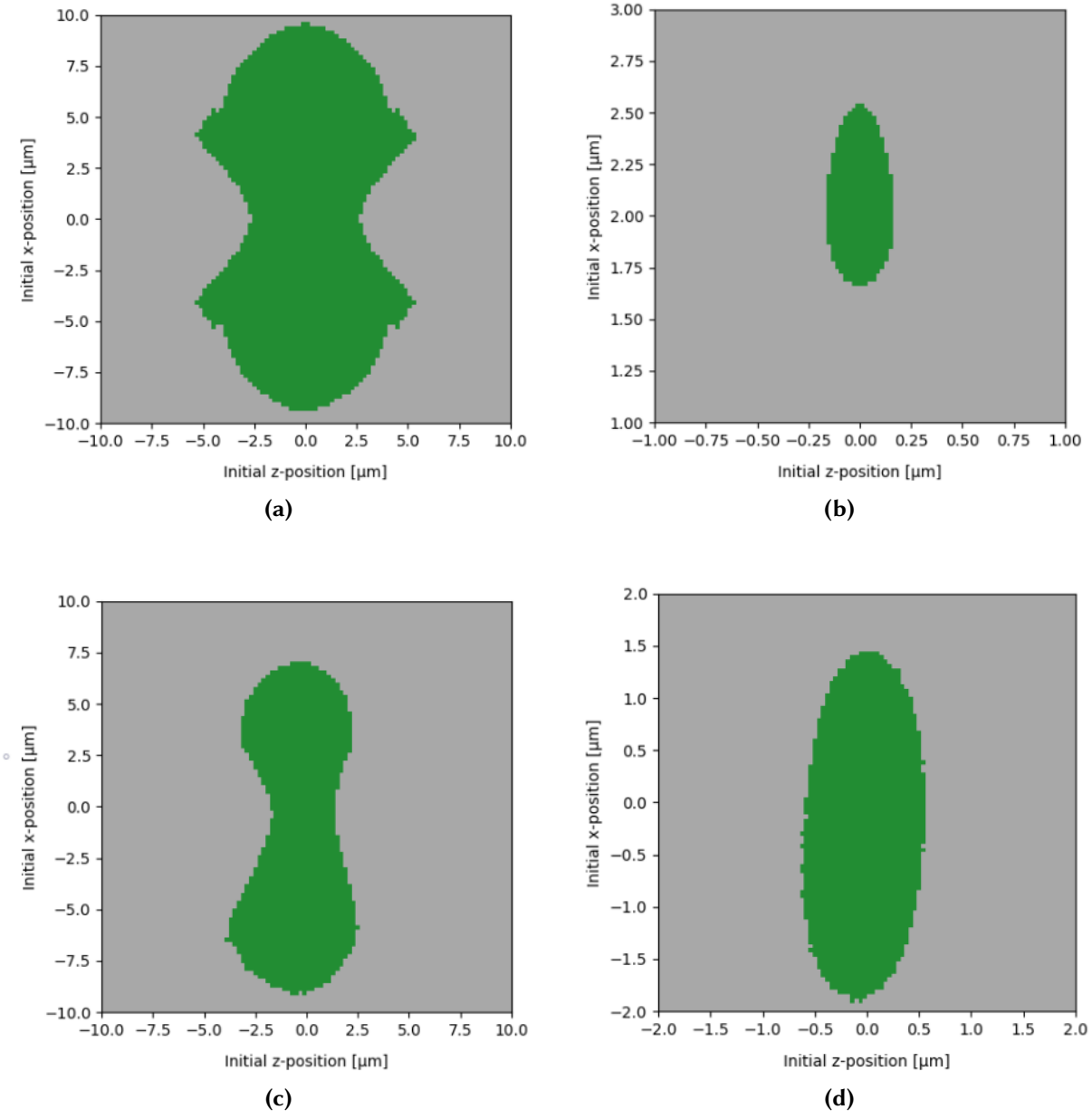

Figure 4.4: The area in green is the region in the plane orthogonal to gravity ($y = 0$), in which a spherical SiO_2 particle of (a) 100nm, (b) 435nm diameter can be stably trapped at a pressure of 15mbar, a tweezer waist of 1µm and a wavelength of 1550nm under the idealized assumption that it is initially at rest, while (c) and (d) display the respective regions for a 100nm particle with initial velocities of (-0.1, 0.3, 0.1)m/s and (-0.5, 0.8, 0.5)m/s, respectively. The tweezer axis is the x-axis. There is no position at which trapping is possible above a particle diameter of 435nm, in accordance with eq. (4.8).

The presence of radiation pressure displaces the particle's equilibrium position inside the tweezer slightly downstream and restricts both the region in phase space in which a particle can be stably trapped and the admissible size range. These limits are independent of laser power, which enters linearly both in the gradient force and in the radiation pressure.

We can estimate the maximum radius r_{max} a particle can have to be in principle trappable. The intensity distribution of a Gaussian beam is given by the expression

$$I_{\text{tw}}(\mathbf{r}) = I_0 \frac{W_0}{W(x)} e^{-\frac{2(y^2+z^2)}{W(x)^2}}, \tag{4.5}$$

where

$$I_0 = \frac{2P_{\text{tw}}}{\pi W_0^2} \tag{4.6}$$

and, remembering the definition of the Rayleigh length x_R, eq. (2.24),

$$W(x) = W_0 \sqrt{1 + \left(\frac{x}{x_R}\right)^2}. \tag{4.7}$$

We can now set $y = z = 0$ and evaluate the two forces at $x = x_R$, where the ratio $F_{\text{grad}}/F_{\text{rad}}$ is maximized. Imposing the condition that the gradient force has to dominate over the radiation pressure at least at that point, we obtain the equation

$$r_{\text{max}} = \left(\frac{3\lambda^5}{32\pi^5 W_0^2} \frac{n^2+2}{n^2-1}\right)^{1/3}. \tag{4.8}$$

This results in $r_{\text{max}} \approx 218\text{nm}$ for a waist of $W_0 = 1\mu\text{m}$ and a wavelength of 1550nm, which agrees with our simulation (see fig. 4.4). Trapping large particles is, however, demanding as the requirements imposed on initial positions and velocities become increasingly strict with growing size. This is because the optical potential scales linearly with polarizability (and hence volume), while, according to eq. (4.4), the radiation pressure grows in proportion to the polarizability squared. Even for our 100nm particles we find the trapping region to be only a few cubic micrometers large.

As eq. (4.8) reveals, the gradient force can only dominate over the radiation pressure if the beam waist is sufficiently small. We hence require the spot size to be diffraction-limited, in which case the waist is related to the numerical aperture (NA) of the lens by the equation

$$W_0 = \frac{\lambda}{\pi \cdot \text{NA}}. \tag{4.9}$$

Given our NA of 0.81, this yields a theoretical limit of $W_0 \approx 610\text{nm}$ at $\lambda = 1550\text{nm}$.
In order to come close to that value in the experiment, it has proven crucial to precisely align the tweezer beam with respect to the lens. Even a slight deviation of a few mrad from orthogonal incidence impairs the focus quality to such an extent that trapping becomes infeasible. This is due to significant comatic aberration as depicted in fig. 4.5. Since the lens is glued onto its holder, which we can only move along the three spatial axes, we need to compensate for any tilt by adapting the direction of the incident beam.
To that end, we illuminate the flat side of the lens from the backside of the vacuum chamber using a laser diode with a wavelength of 405nm, for which the lens is not anti-reflection coated. We make sure that the beam is reflected into itself by placing a pinhole directly in front of the collimator of the diode, at a distance of about 80cm from the lens. We subsequently place a mirror into the beam path and adjust it until the reflected light passes again through the same pinhole. Finally, we move the lens out of the way and align the trapping beam with respect to that very

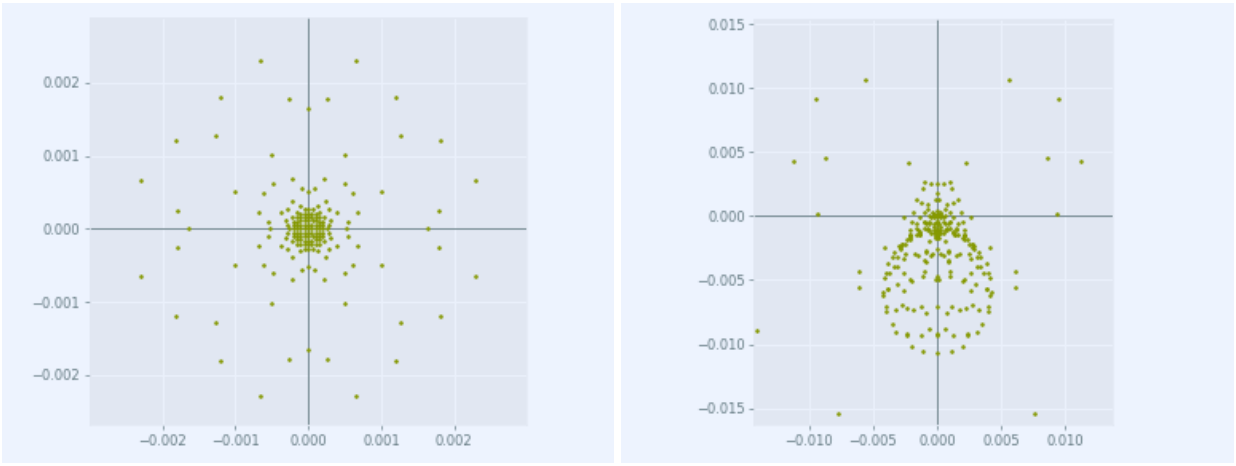

(a) **(b)**

Figure 4.5: Theoretical spot diagrams obtained for our custom Thorlabs aspheric tweezer lens at an angle of incidence of 0° and 1°, respectively (values are in mm). The figures were created using the RayOptics library for Python.

mirror until the incident field and the backreflex from the tweezer again overlap. We estimate that this technique allows us to reduce the angular imprecision to well below 5mrad.

When we loaded the trap using the nebulization technique and hence started at pressures of a few 100mbar as discussed in sec. 4.1.1, we lost the particle as soon as we opened the valve to evacuate the vacuum chamber. While we have now replaced our original isolation valve with a continuously adjustable one, which alleviates this issue, the complication is avoided altogether by loading the trap at about 15mbar using LIAD. However, even though the particle does not get sucked up by the pump immediately, we have still consistently been losing it as we reduced the pressure to the range between 1 and 5mbar.
As we have already alluded to in sec. 3.4.1, it is possible that this has been a consequence of the large tweezer intensity, which we required to be on the order of tens of MW/cm^2 for successful trapping due to an unsatisfactory beam profile. Indeed, as noted by Millen et al. [70], this may already be too much for the particle to "survive", depending on the presence of contaminants.

The latter point together with the fact that we have been facing difficulties in resolving the mechanical frequencies in the Fourier transform of our trapping signal highlights the need for the tweezer to feature a clean Gaussian mode profile. We now achieve this by letting the beam pass through a single-mode fiber, which filters out the undesired field components. Despite the modest coupling efficiency of 30% that we currently attain, we expect significant improvement in the quality of the signal. As a first step in that direction, we have recently managed to reduce the trapping power to 200mW without losing the particle.
In the near future, feedback cooling will assist us in keeping the particle trapped during the transition to high vacuum [101, 102], cf. sec. 4.1.5. This will, for example, counteract photophoretic forces, which occur as a result of a non-uniform surface temperature [103]. While a vertical trap setup, where the tweezer propagates antiparallel to gravity, in combination with a high-NA lens can circumvent the need for feedback cooling [104], we expect that it is indispensable in our setup.

In the medium term, we will also have to consider electrodynamic traps as a possible extension to our current method. While optical tweezers are in principle simpler to implement and exhibit higher trapping frequencies, ion traps feature larger trapping volumes and depths [14] and allow for direct capture in high vacuum [98]. This is particularly relevant if we want to investigate particles of smaller mass, which diffuse more easily. In addition, fragile species might not survive direct irradiation with an intense optical trapping field.

4.1.3 Cavity Locking and Finesse Measurement

As we have already argued in sec. 2.2.3, eq. (2.74), the coherent scattering cooling scheme requires the optical tweezer to be detuned with respect to the cavity resonance by an appropriate amount. If not compensated for by a feedback mechanism, unavoidable thermal and mechanical drifts would cause fluctuations in the detuning over time and thus render cooling impossible. We choose to stabilize the laser frequency with respect to the cavity mode rather than the other way around and have so far successfully locked to the cavity resonance. The experimental demonstration of the required frequency shift is still outstanding, but we discuss the implementation in our setup in sec. 4.2.2.

Very generally speaking, locking the laser frequency onto the cavity resonance requires an active feedback from the cavity response, which can originate either from the reflected or transmitted light. From that, an *error signal* is derived, which a PID (proportional-derivative-differential) controller subsequently converts to a *control signal*. This signal is fed to the laser and prompts it to adjust the output frequency in a way that counteracts drifts away from the desired value.
One might feel tempted to obtain the error signal directly from the cavity transmission by defining a setpoint at half the maximum of the corresponding peak. Subtracting this value from the original signal yields a negative voltage when the transmission is lower than the setpoint and a positive one when it is higher. This is called *side-of-fringe* locking. While it is simple to implement, this method suffers multiple drawbacks. The most obvious one is that the error signal is symmetric about the transmission maximum, which precludes the ability to lock directly onto the maximum of the transmission. This inevitably compromises the intracavity optical power and acquisition range [105].
A more sophisticated approach is *top-of-fringe* locking. In short, this scheme employs a (very small) modulation of the laser. The modulation input is then multiplied with the transmission signal, yielding an error signal that is antisymmetric about the resonance and features a zero-crossing [106]. However, the locking frequency is ultimately limited by the laser's modulation frequency, which in our case is at most 100kHz. This is merely about three times larger than the cavity decay rate and hence not sufficient to ensure a stable lock.

We consequently choose to employ the more elaborate *Pound-Drever-Hall* technique. We will only explain the basic concept here and refer the reader to ref. [107] for a detailed treatment of the mathematical background. In simple terms, the error signal used in this scheme stems from the interference between light at the (near-)resonant carrier frequency and a sideband, which is separated from the latter by an RF frequency that is much larger than the cavity linewidth. The carrier enters the cavity and eventually leaks out again with a phase shift that depends on the detuning and is equal to π in case of perfect resonance, while the sideband is rejected by the cavity and reflected from the first mirror without phase shift.
The power of the total reflected field is subsequently detected by a photodiode. The term of interest is the interference term of this signal, which oscillates at the RF frequency and contains the phase relation between the carrier and the sideband [107]. Importantly, the relative phase is not symmetric about the cavity resonance. In order to get rid of the fast oscillation, the electrical signal from the detector is then mixed with the (appropriately phase-shifted) RF signal that generated the sideband and passed through a low-pass filter before it enters the PID. We discuss the practical implementation in our setup in sec. 4.2.2.

Resonance Detection

Before we can activate the PID, we have to find the resonance frequency. We drive the cavity at the lowest possible laser output power of 20mW, which we then attenuate by 25dB to avoid

instabilities due to thermal lensing. In order to automize the search for the resonance, we write a Python script that establishes communication with the laser (using the software development kit provided by NKT Photonics), prompts it to modulate the output wavelength at the maximum range using an externally generated triangular signal, and gradually increases the wavelength offset. The laser accomplishes the latter by adapting its temperature and hence the length of its internal cavity. This procedure continues until a transmission signal from our cavity is detected. The driving signal has an amplitude of 1V, which is shifted by two 1.5V batteries for technical reasons, and a frequency of 300mHz.

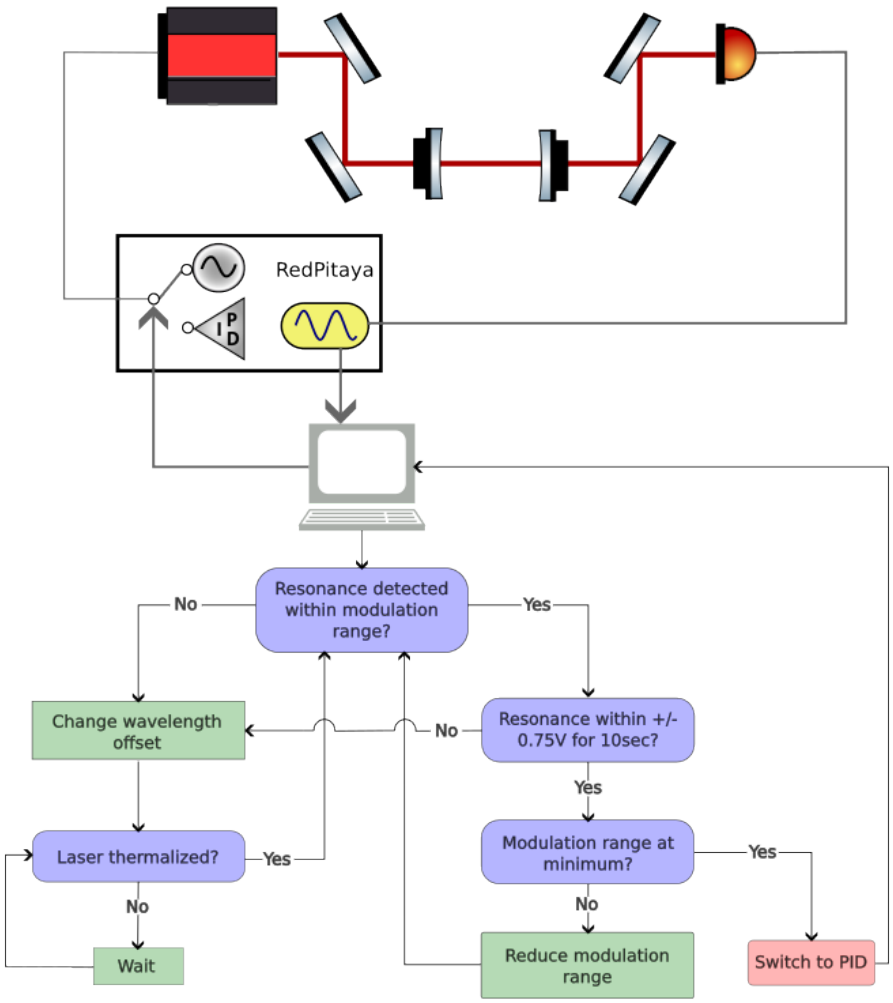

Figure 4.6: Simplified illustration of the resonance detection and PID activation procedure. The laser wavelength is modulated by an externally generated RF signal with an amplitude of 1V. The wavelength offset is then gradually increased until the oscilloscope triggers on the presence of a resonance. At that point, the script aims to keep the transmission signal within a range of ± 0.75V of the RF signal and to continuously reduce the modulation range. At the lowest range, the modulation signal is turned off and the PID is enabled.

Once a signal in transmission has been obtained, we still need to narrow down the modulation range of our laser in order for the PID controller to work. To that end, we complement the script by a basic custom PID, which seeks to maintain the resonance at the zero-crossing of the modulation signal. If the transmission maximum occurs at a negative voltage, we increase the wavelength and vice versa. As soon as we keep the resonance within ± 0.75V for more than 10 seconds, we reduce the modulation range by 20% until we are down to the smallest one possible. At that point,

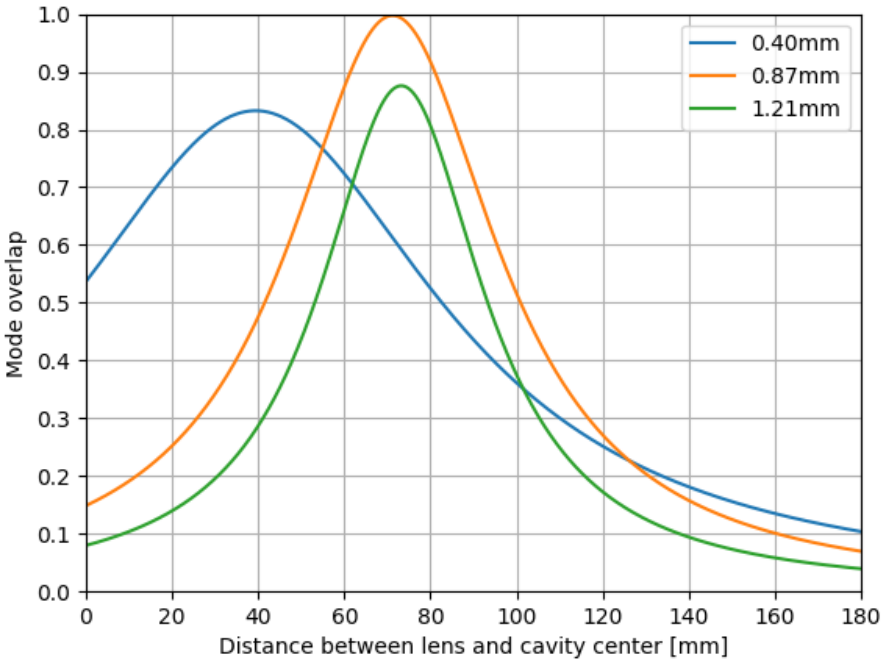

Figure 4.7: Overlap of the cavity mode and the ingoing beam as a function of distance between the coupling lens and the center of the cavity for initial beam diameters of 0.4mm (blue), 0.87mm (orange) and 1.21mm (green). We currently use a collimator with a beam diameter of 0.87mm. The light is focused by a plano-convex lens with a beam focal length of 75mm, which is also approximately the distance to the cavity center. The cavity length is assumed to be 18mm, the width of the mirrors 3mm and their radius of curvature 5cm, cf. sec. 4.2.2.

the transmission signal is limited by the cavity decay time and the PID is switched on, which, provided a suitable choice of parameters, keeps the cavity locked. The (simplified) procedure is illustrated in fig. 4.6.
The Pound-Drever-Hall technique only works under the condition of efficient coupling to the cavity mode as measured by the dip in the backreflex from the mirrors. We get a maximal value of about 70%, which is satisfactory for our purposes. The theoretically achievable coupling efficiency as a function of distance between the lens and the center of the cavity is displayed in fig. 4.7 for different diameters of the ingoing collimated beam.
We use a RedPitaya as a function generator for the modulation signal, as an oscilloscope to measure the cavity transmission and transfer the data to our script and as PID controller, the working principle of which we will now clarify.

PID Controller

A PID controller takes an error signal $e(t)$ as an input and generates a control signal $c(t)$ by applying a proportional (P), integral (I) and derivative (D) correction with the aim of counteracting any deviation of $e(t)$ from zero, i.e.

$$c(t) = K_p e(t) + K_i \int_0^t \mathrm{d}\tau\, e(\tau) + K_d \frac{\mathrm{d}e(t)}{\mathrm{d}t}. \tag{4.10}$$

A large K_p-parameter increases the sensitivity as it causes even minor changes in the input to stimulate a pronounced response by the PID, but also entails the risk of overcorrection. The integral term adds up the values of the error signal over time. This is meant to counteract drifts

that occur over a larger timescale. If, on the other hand, positive and negative values of the error signal consistently cancel each other out, the integral term in the control signal vanishes.
The derivative term acts on the rate of change of the error signal and has predictive character. A large positive (negative) slope at a specific point in time indicates a higher (smaller) value of the error signal in the future, which the PID controller seeks to prevent. Applying the derivative correction is, however, only constructive if the noise in the error signal is very low. Since this does not hold in our case, we set K_d to zero.

Finesse Measurement

In order to measure the cavity's finesse, we first have to determine its free spectral range. To that end, we modulate the beam using an electro-optic modulator (see sec. 4.2.2) and vary the modulation frequency until the cavity transmission peaks corresponding to the carrier and the sidebands overlap. When this is the case, they fulfill the resonance condition at the same time, indicating that they are separated by exactly one FSR.
Thereafter, we imprint sidebands at 200kHz as a reference. They fulfill the resonance condition at a different point in time as the laser scans over a range of frequencies. A Python script then detects the transmission peaks pertaining to the carrier and the sidebands and fits them to Lorentzian curves. From the full widths at half-maximum, the separation of the peaks in time and the modulation frequency, it computes the cavity's linewidth and, by virtue of eq. (2.51), the finesse. We find the FSR at 8.22GHz and measure a finesse of 295,000, which is only slightly lower than the 314,000 that we would theoretically expect invoking eq. (2.48) at a nominal reflectivity of 99.999%.
Obtaining a valid result requires the width of the transmission curve to be limited by the cavity decay rather than the frequency at which the laser modulates its wavelength. Secondly, the sideband frequency has to be chosen wisely, i.e. significantly larger than the cavity's decay rate to prevent the carrier and sideband peaks from overlapping, but small enough to avoid drifts in the resonance during the modulation.

4.1.4 Detection

We will now provide an overview over the different detection schemes that we currently (or are planning to) employ to keep track of the particle's motion.

Direct Scattering

As a simple first step, we insert a multimode scattering fiber with a numerical aperture of 0.5 at a 45° angle with respect to the tweezer-cavity plane as illustrated in fig. 4.1. In order to avoid picking up any green light scattered from the LIAD beam, we place a longpass filter with a cutoff wavelength of 1500nm in front of the photodiode.
It is worthwhile to estimate how close we should position the focus of the trapping beam to the tip of the scattering fiber. This consideration is contingent upon whether the detection efficiency is limited by the fiber's active diameter or its numerical aperture. The latter holds whenever the distance D between the scattering center (which we can assume to be located in the focus of the tweezer) and the fiber tip satisfies

$$D < \frac{d}{2 \cdot \tan(\arcsin(\mathrm{NA})/2)}, \tag{4.11}$$

where d is the diameter of the fiber core, which in our case is 600µm. Under that condition, the cone of the scattered light that is picked up by the fiber is fully contained within its active cross sectional area. As a consequence, we can move the tip close to the focus (and hence maximize the signal) without becoming more sensitive to alignment as long as $D \lesssim 1.1$mm. In order not

to cut off the highly divergent tweezer beam, we choose a distance of 200µm as a reasonable compromise.
As for the alignment, we first position the lens such that the beam is focused onto the fiber tip, which we verify by observing the shadow of the fiber with an InGaAs infrared camera (Xenics Bobcat 320). The fiber is inside the focus when the upright and inverted shadows overlap. We then displace the lens diagonally (i.e. parallel to the fiber) by the desired distance.

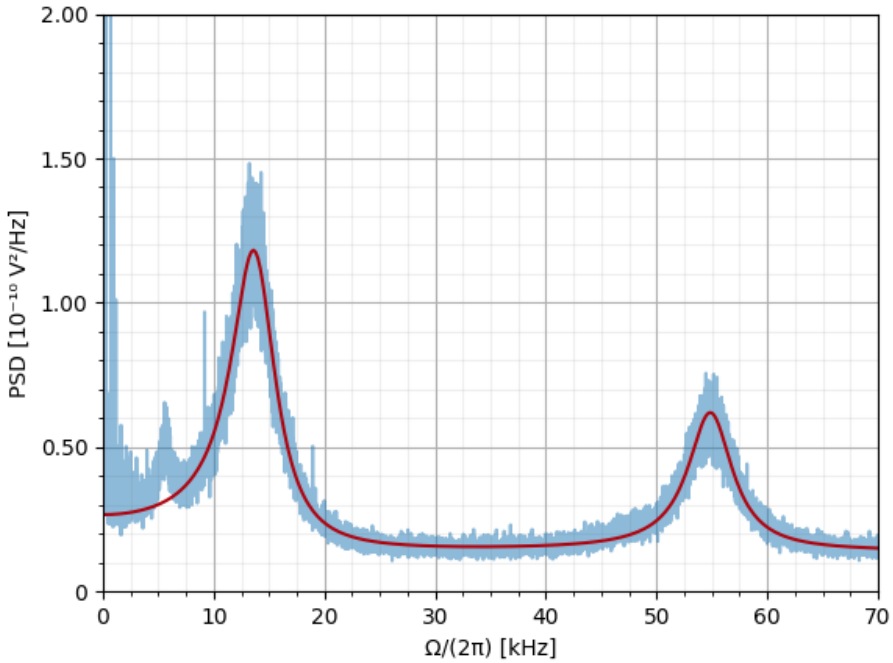

Figure 4.8: Motional PSD of a trapped SiO_2 nanoparticle at a pressure of 12.2mbar. The first peak at a frequency of 2π·14.0kHz corresponds to the oscillation in the x-direction (along the tweezer axis), while the second one at 2π·55.0kHz pertains to the motion along y and z. The red curve indicates a fit with eq. (3.42).

In fig. 4.8, we show the PSD of a trapped nanoparticle at 12.2mbar obtained from the scattering fiber. However, a fit with eq. (3.42) indicates a particle radius of (164.6 ± 0.6)nm compared to the expected 75nm. Further data are required to determine whether this disparity is a matter of coincidence or of a systematic issue.

Alternatively, one may detect the light that is scattered in the forward or the backward direction of the tweezer beam. We choose the latter option and employ a balanced detection scheme, which we will now explain.

Balanced Backscattering Detection

By detecting the light scattered in the opposite direction of the incident beam, we benefit from the larger numerical aperture of the tweezer lens as well as from the fact that the direction of observation is guaranteed to be perpendicular to the polarization axis. The latter point ensures that the scattering intensity is maximized, cf. eq. (2.44).
More concretely, we can estimate the total scattered power for a SiO_2 nanoparticle of 100nm diameter, a tweezer power of 200mW, a wavelength of 1550nm and a waist of 1µm to be about 310nW according to the relation

$$P_{\text{scatt}} = \sigma_{\text{scatt}} I_{\text{tw}}, \tag{4.12}$$

where σ_{scatt} is given by eq. (4.4). Out of that, the tweezer lens would pick up 60nW and the scattering fiber between 900pW when the polarization axis is parallel to the fiber and 23nW when it is orthogonal.
In addition to the above considerations, the backscattered light allows us to employ a balanced detection scheme [34] in order to differentiate between the mechanical oscillations along the two spatial axes perpendicular to the propagation direction of the tweezer. To that end, we first split the beam of the scattered light into two equal parts, cut one beam in the horizontal and the other one in the vertical direction using D-shaped mirrors and detect both halves of each beam using balanced photodetectors (Thorlabs PDB440C-AC). Those detectors subtract the two input signals from each other and generate a corresponding RF output at a bandwidth of 15MHz.
The difference in the incident power is given by

$$\Delta P_{\text{in}} = \frac{c\epsilon_0}{2}\left[\int_{\pi/2}^{3\pi/2} \mathrm{d}\phi \int_0^\infty \mathrm{d}r\, r\, |E_{\text{in}}(r,\phi)|^2 - \int_{3\pi/2}^{\pi/2} \mathrm{d}\phi \int_0^\infty \mathrm{d}r\, r\, |E_{\text{in}}(r,\phi)|^2\right], \tag{4.13}$$

where (r, ϕ) denote the polar coordinates in the plane perpendicular to the propagation direction of the light and E_{in} the incident field. Naively, one might suspect that the imbalance in the respective powers is due to a spatial displacement of the beam as a result of the particle's motion. However, given the small amplitude of the oscillations, which is only on the order of hundreds of nanometers even prior to cooling, this effect would be unobservably small.
Instead, the detection method relies on the difference in the phases acquired by the scattered spherical wave as it travels from the location of the particle to the tweezer lens [76]. When the particle is displaced from the center of the focal spot, those phases are asymmetric about the optical axis. Upon overlapping the scattered light with a reference beam, this gives rise to an observable shift in the intensity distribution. While we ultimately aim to enhance its power using the reflection from a glass plate, a faint reference is always present due to the non-zero reflection of the lens and the other elements inside the optical path. In that sense, the detection constitutes a self-homodyne measurement as we will explain in further detail below.

Homodyne Detection

By superimposing a probe signal with a strong local oscillator, one can measure either of the quadratures of the light field under investigation (or a combination of both). What is observed in the end is determined by the phase of the reference. Balanced homodyne detection, which we have already alluded to in the previous section, is a special case of this technique, whereby light from both outputs is collected to generate the difference signal. This effectively eliminates common noise from the local oscillator.
The reference can either be obtained by splitting off a fraction of the ingoing tweezer beam, which is then recombined with the backscattered light at a beamsplitter, or, as mentioned before, we may exploit the light that is retroreflected at normal incidence by a glass plate. We perceive the latter as the more stable and hence preferable option. In a more sophisticated approach [108], one could also use the light reflected by a mirror downstream of the focus. This would, however, also influence the trapping potential and hence bring about additional complications.
Irrespective of how we obtain the reference, the key point is that this detection scheme is sensitive to the particle's ro-translational motion, which is encoded in the phase of the scattered light, i.e. $\phi_{\text{sig}} = \phi_{\text{sig}}(\mathbf{r}(t), \Omega(t))$. In particular, this is also true for the axial degree of freedom along the propagation axis of the tweezer. To see this, note that the total electric field is given by the sum of reference and signal,

$$E_{\text{tot}} = E_{\text{ref}} e^{i(\phi_{\text{ref}}+\omega t)} + E_{\text{sig}} e^{i(\phi_{\text{sig}}(\mathbf{r}(t),\Omega(t))+\omega t)}. \tag{4.14}$$

The intensity is hence proportional to

$$|E_{\text{tot}}|^2 = |E_{\text{ref}}|^2 + |E_{\text{sig}}|^2 + 2E_{\text{ref}}E_{\text{sig}} \cos\big(\phi_{\text{ref}} - \phi_{\text{sig}}(\mathbf{r}(t),\Omega(t))\big). \tag{4.15}$$

Since $|E_{\text{ref}}| \gg |E_{\text{sig}}|$, the amplitude of the last term is substantially larger than $|E_{\text{sig}}|^2$. Restricting ourselves to the motion along the z-axis and assuming that we can expand $z(t)$ harmonically, we can write [76]

$$\begin{aligned}\cos\big(\phi_{\text{ref}} - \phi_{\text{sig}}(z(t))\big) &\approx \cos(\phi_{\text{ref}} - \phi_0\cos(\Omega_z t)) \\ &= \cos(\phi_{\text{ref}})\cos(\phi_0\cos(\Omega_z t)) + \sin(\phi_{\text{ref}})\sin(\phi_0\cos(\Omega_z t)) \\ &= \cos(\phi_{\text{ref}})\left(J_0(\phi_0) + 2\sum_{n=1}^{\infty}(-1)^n J_{2n}(\phi_0)\cos(2n\Omega_z t)\right) \\ &\quad - 2\sin(\phi_{\text{ref}})\sum_{n=1}^{\infty}(-1)^n J_{2n-1}(\phi_0)\cos[(2n-1)\Omega_z t],\end{aligned} \tag{4.16}$$

where $J_n(z)$ are the Bessel functions of the first kind. Getting rid of the first term of eq. (4.16) by imposing $\phi_{\text{ref}} = -\pi/2$ [76] ensures that the dominant contribution comes from the oscillation at the mechanical frequency Ω_z. Filtering out the constant terms in eq. (4.15) by means of the balanced detection yields a signal that varies sinusoidally with Ω_z at a strength that is proportional to the amplitudes of the reference and the scattered field as well as to the amplitude of the mechanical oscillation provided that $\phi_0 \ll 1$.

Heterodyne Detection

Heterodyne detection is conceptually similar to the homodyne scheme, but assumes the two fields to oscillate at distinct frequencies ω_{ref} and ω_{sig}, respectively. We will employ this technique in order to differentiate between the Stokes and Anti-Stokes photons that the particle scatters into the cavity mode and eventually leak out through the mirrors. This will allow us to extract the motional temperature via sideband asymmetry thermometry, cf. sec. 3.4.1.
As we will discuss in further detail in sec. 4.2.1, we couple a small fraction of the tweezer beam into a polarization-maintaining fiber and use this as a reference. In analogy to the previous calculation, the modulus squared of the total field incident on the detector reads

$$|E_{\text{tot}}|^2 = |E_{\text{ref}}|^2 + |E_{\text{sig}}|^2 + 2E_{\text{ref}}E_{\text{sig}}\cos\big(\phi_{\text{ref}} - \phi_{\text{sig}}(\mathbf{r}(t), \Omega(t)) + (\omega_{\text{ref}} - \omega_{\text{sig}})t\big). \tag{4.17}$$

Defining $\Delta\omega = \omega_{\text{ref}} - \omega_{\text{sig}}$ and again regarding only the motion along z, we can expand

$$\begin{aligned}\cos\big(\phi_{\text{ref}} - \phi_{\text{sig}}(z(t)) + \Delta\omega t\big) &\approx \cos(\phi_{\text{ref}} + \Delta\omega t)\left(J_0(\phi_0) + 2\sum_{n=1}^{\infty}(-1)^n J_{2n}(\phi_0)\cos(2n\Omega_z t)\right) \\ &\quad - 2\sin(\phi_{\text{ref}} + \Delta\omega t)\sum_{n=1}^{\infty}(-1)^n J_{2n-1}(\phi_0)\cos[(2n-1)\Omega_z t].\end{aligned} \tag{4.18}$$

Setting the phase of the reference equal to zero results in

$$\begin{aligned}\cos\big(\Delta\omega t - \phi_{\text{sig}}(z(t))\big) &\approx J_0(\phi_0)\cos(\Delta\omega t) + \sum_{n=1}^{\infty}(-1)^n J_{2n}(\phi_0)\Big\{\cos[(\Delta\omega - 2n\Omega_z)t] \\ &\quad + \cos[(\Delta\omega + 2n\Omega_z)t]\Big\} - \sum_{n=1}^{\infty}(-1)^n J_{2n-1}(\phi_0) \\ &\quad \Big\{\sin[(\Delta\omega - (2n-1)\Omega_z)t] + \sin[(\Delta\omega + (2n-1)\Omega_z)t]\Big\}.\end{aligned} \tag{4.19}$$

The spectrum hence features a peak at the difference frequency and sidebands at the harmonics of the mechanical frequency. Their signal strength is proportional to the modulus squared of the corresponding cavity transfer function, eq. (2.70), at the given detuning [34]. A large $\Delta\omega$ is generally preferable due to a lower noise floor [76], but it must not exceed the detector bandwidth, which, as we have said previously, is 15MHz in our case.

4.1.5 Optical Feedback Cooling

As we have already mentioned, optical feedback cooling [25] will allow us to go to high vacuum without losing the particle as we traverse the intermediate pressure regime [102].
To that end, we place an acousto-optic modulator (AOM, Brimrose) in the beam path and drive it at an RF frequency of 85MHz using a signal generator (Tabor LS3084B). We optimize the alignment until the efficiency of diffraction into the first order is maximal and reduce the RF power to 160mW, at which point the diffraction efficiency amounts to about 20%. This is sufficient for our purposes, since we expect the required modulation depth to be on the order of a few percent [109].
We aim to keep the power of the electrical signal as low as possible in order to minimize degradation of the beam shape due to thermal lensing. As we are only interested in intensity modulation, we henceforth only use the zeroth diffraction order and dump the first. Upon switching on the signal generator, we let the AOM heat up for 15 minutes in order to stabilize the output beam.

The next step that we will need to undertake is to lock on the frequencies in the FFT, cf. fig. 4.8, using a lock-in amplifier (Zurich Instruments HF2LI). This device extracts the phase and amplitude of a specific frequency in a noisy input signal, yielding a clean output that is in phase with the particle's motion and drives the amplitude modulation. To that end, the lock-in amplifier employs a phase-locked loop (PLL), whereby it mixes (i.e. multiplies) the noisy signal with a reference of a known phase and frequency. This procedure generates a spectrum featuring the sum and the difference frequency of the two inputs. The latter is extracted by passing the signal through a low-pass filter. A PID controller subsequently creates a feedback signal, which is fed to a voltage-controlled oscillator and converted to a frequency modification of the reference to close the loop.
If the scattering signal is sensitive to the particle's position rather than its absolute distance from the trap center (as is the case in balanced detection, cf. sec. 4.1.4), the modulation must be at twice the frequency of the feedback signal. However, if we use the signal from the scattering fiber, which is only dependent on the particle's displacement, the modulation frequency must match that of the detected signal.

4.2 Setup

Our basic setup is displayed in fig. 4.9. The cornerstone of our experiment is the Koheras Adjustik E15 laser from NKT photonics, which is connected to a Koheras Boostik E15 fiber amplifier. The laser operates at a wavelength of 1550nm and features an ultra-narrow linewidth of <1kHz as well as exceptionally low phase noise of 0.4µrad/(m$\sqrt{\text{Hz}}$) at 10kHz.[3] The maximum output power is 10W. The wavelength is a sensible choice as both SiO_2 and Si[4] exhibit extremely low absorption in the near-infrared regime.
We place an isolator (IO-5-1550-HP) right behind the (pre-installed) collimator terminating the optical fiber of the laser, followed by a $\lambda/2$-plate and a polarizing beamsplitter (PBS). The combination of the waveplate and the PBS allows us to continuously tune the effective optical power even below the minimal output power of the amplifier, which is about 500mW. We keep the transmitted (p-polarized) beam as it features a more satisfactory beam profile and dump the s-polarized contribution that is reflected by the PBS.
The beam is then divided into two branches by a beam sampler, which for p-polarized light and at a 45° angle reflects about 0.6% of the incident radiation.

[3] This is based on the specifications and has not yet been tested.
[4] We might want to use Si instead of SiO_2 in the future due to its higher polarizability.

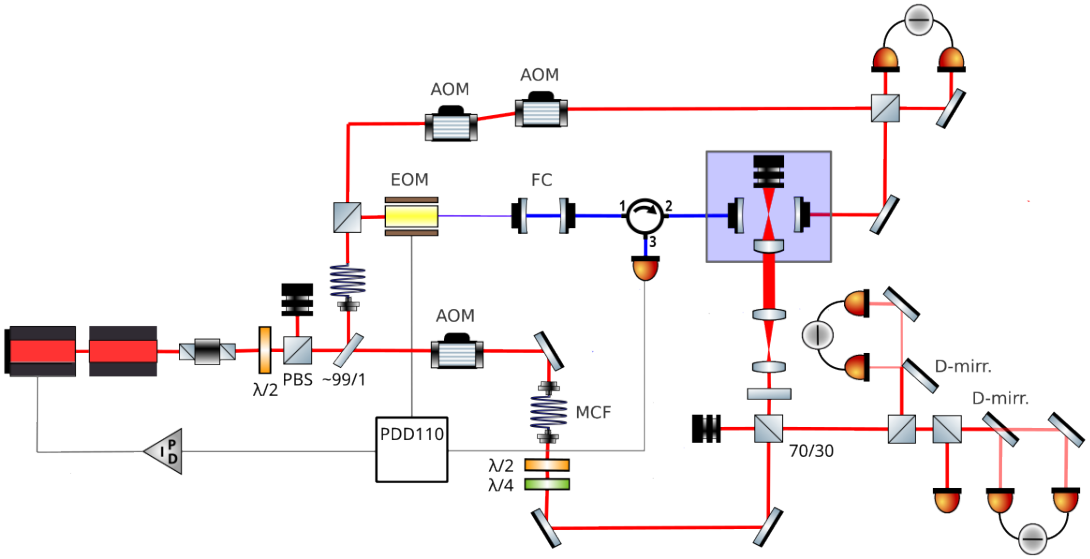

Figure 4.9: Simplified sketch of our current setup. The tweezer beam passes an AOM, a mode cleaning fiber (MCF), a $\lambda/2$ and a $\lambda/4$-plate, a 70:30 beamsplitter and a telescope before it enters the vacuum chamber (shaded in blue). A small fraction of the beam is split off by a beam sampler and coupled into a polarization-maintaining fiber. Half of that light passes an EOM and a filtering cavity (FC) and is used for locking the cavity, while the other half serves to perform heterodyne detection.

We will now separately discuss those two parts of the setup. The major part of the optical power is dedicated to the tweezer, while the rest is coupled into an optical fiber and used for cavity locking and for heterodyne detection as explained in secs. 4.1.3 and 4.1.4, respectively.

4.2.1 Tweezer Preparation

After the beam sampler, the tweezer passes through the AOM and is subsequently coupled into a single-mode fiber for mode cleaning. We detect a small portion of the light with the help of a fiber-based 95:5 beamsplitter to keep track of the coupling efficiency and employ a circulator to detect the particle's motion along the tweezer axis. Since we eventually require the beam to be elliptically polarized as we have argued in sec. 2.3, we insert a $\lambda/2$ and a $\lambda/4$-plate upon recollimation.
After that, the beam is guided through a 70:30 beamsplitter, which serves the purpose of deflecting the backscattered beam. As we have said previously, we are then planning to insert an uncoated glass plate with a reflectivity of about 3% at normal incidence to derive the reference. We estimate that the reflected power exceeds that of the backscattered light by a factor of 10^5.
The transmitted beam is subsequently expanded tenfold with a telescope, which consists of an aspheric lens with 10mm focal length and an achromatic doublet with a focal length of 100mm. Thereby, we completely fill the aspheric tweezer lens (custom-made by Thorlabs) after the beam enters the vacuum chamber via two periscope mirrors. The large beam diameter alongside the lens' high NA of 0.81 ensures a diffraction-limited spot size, which we require both for successful trapping (see sec. 4.1.2) and to enhance the optomechanical coupling. The tweezer lens is mounted on a SmarAct nanopositioning stage, which can be moved along all three spatial axes.
Backscattering detection using the D-shaped mirrors and the balanced photodetectors has also already been set up.

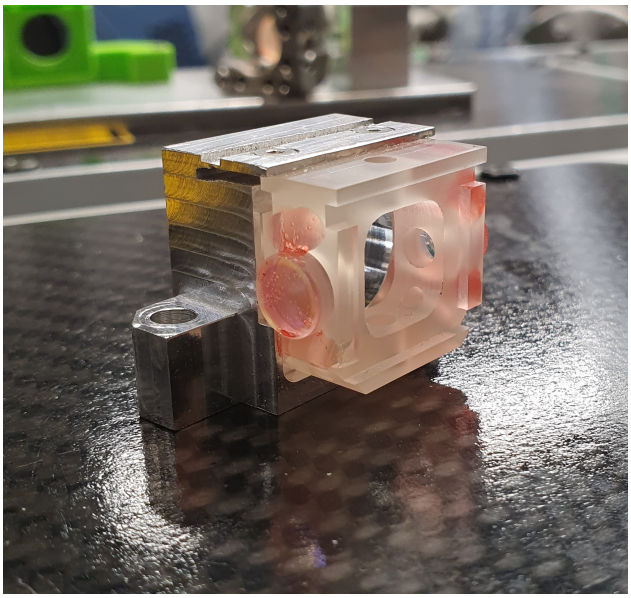

Figure 4.10: The current version of our optical cavity. The mirror holder, which is clamped onto an aluminum block, is made out of Zerodur to reduce thermal perturbations and features a hole on the top through which the particles are injected. The mirrors are separated by a distance of about 18mm. Design by Stephan Troyer.

4.2.2 Cavity and Cavity Locking

Our optical cavity, which is shown in fig. 4.10, is formed by two spherical mirrors (FiveNine Optics) with a diameter of 7.75mm, a nominal reflectivity of 99.999% and a radius of curvature (RoC) of 5cm. They are separated by a distance of approximately 18mm, which means that we are operating far away from the border of the stability zone. This results in an undesirably large beam waist of about 100µm inside the cavity as follows from the relation [110]

$$w_0^2 = \frac{\lambda}{2\pi}\sqrt{d(2\mathrm{RoC} - d)}, \tag{4.20}$$

where d is the distance between the mirrors.
While a smaller waist would be preferable, early attempts to obtain a transmission signal using mirrors with an RoC of 1cm, which would reduce the waist to about 38µm, have failed due to complications regarding the alignment. While we still intend to eventually employ the 1cm mirrors, we for now content ourselves with the 5cm counterparts.
The alignment of the cavity is then facilitated by visually preadjusting the beam using a laser diode with a wavelength of 1370nm. There, the cavity mirrors are transmissible enough to observe the outgoing light with an infrared detector card but still sufficiently reflective for the light of three to four cavity roundtrips to be visible. Overlapping them provides a valuable indication of the required beam direction and position.
In order to counteract drifts in the cavity resonance due to thermal fluctuations, we resort to a cavity holder made out of Zerodur®, a special glass-ceramic by Schott, which features an exceptionally low thermal expansion coefficient of 0 ± 0.1ppm/K. The cavity mirrors are glued into the holder, implying that the in- and outcoupling mirrors constitute the only degrees of freedom for alignment.

As far as the locking is concerned, we have already mentioned that we couple a tiny fraction of the tweezer beam into a polarization-maintaining fiber. We then maximize the power in the horizontal polarization direction by rotating the fiber collimator until the signal in the vertical output port of a fiber-based PBS drops to zero. We let half of the light pass through an electro-optic modulator (EOM), which is driven by a signal generator (Rohde & Schwarz SMA100B) with a frequency

range of 8kHz to 12.75GHz. The EOM exploits the Pockels effect, i.e. a variation in the refractive index of a material as a result of an applied voltage, to modulate the phase of the electric field according to

$$E_0 e^{i\omega t} \mapsto E_0 e^{i\omega t + i\beta \sin(\omega_{\text{mod}} t)}, \tag{4.21}$$

where ω_{mod} is the modulation frequency. Following a similar argument as outlined in sec. 4.1.4 for homodyne detection, it can be shown that this modulation imprints sidebands at the integer multiples of the modulation frequency with weights that are determined by the Bessel functions.

While we have only driven the cavity resonantly so far, we eventually need to add an offset corresponding to the desired detuning (cf. sec. 2.2.2) plus one free spectral range. The latter shift is required in order to distinguish the locking signal from the light scattered by the particle. This means that we need to isolate the first sideband, which we will do with the help of a fiber-based filtering cavity (Luna Innovations) with a low finesse of 100.
For manufacturing reasons, the filtering cavity is connected to non-polarization-maintaining fibers, which requires us to add polarization paddles in front of it. Rotating them by an appropriate amount gives rise to (controlled) stress-induced birefringence, allowing us to attain the desired output polarization. We will verify the polarization state using another fiber-based polarizing beamsplitter. We then let the beam pass through a circulator and couple it into the cavity. In order to do so efficiently, the beam diameter, the focal length of the lens and the distance from the lens to the center of the cavity must be chosen in such a way that the mode overlap is maximized as shown in fig. 4.7.
For the locking itself, we use a Toptica PDH detection module (PDD 110). This device contains a signal generator with a frequency of 10MHz and adjustable amplitude, an amplifier for the error signal as well as a phase shifter. We drive the EOM with the (amplified) RF signal from the PDH module and detect the backreflex of the cavity using the circulator. The corresponding photodiode is connected to the error signal input of the module. The resulting PDH signal is then passed through a low-pass filter and directed to the RedPitaya, whereupon the PID converts it to the servo signal, see sec. 4.1.3.

We also pick up the light that the particle scatters into the cavity to perform heterodyne detection, cf. sec. 4.1.4. The reference is provided by the remaining half of the beam, which is not used for locking. The required frequency shift is accomplished by means of two fiber-based Fiber-Q® AOMs (Gooch & Housego) with an operating frequency of 200MHz.

Chapter 5

Rotational Quantum Phenomena and Applications

Gaining control over rotational degrees of freedom and exploring their quantum behavior is a critical task for several reasons, a concise summary of which is provided by ref. [111]. Apart from the elemental interest in generalizing proven concepts to more complex forms of motion, it constitutes a promising pathway towards ultrasensitive pressure [13] and torque [13, 112, 113] sensing, which may not only allow to experimentally verify the existence of Casimir torques [114] and the closely related vacuum friction [115, 116], but also highlights the potential for commercial applicability provided that questions of scalability and integrability are addressed.
On the more fundamental side, the nonlinearity of rotations gives rise to peculiar effects that are worth studying in the quantum domain such as precession [117] and the *tennis racket effect* [118]. The latter refers to the periodic flipping of the axis of medium moment of inertia – the *mid-axis* – in an extended object featuring three distinct moments of inertia in the frame of reference that diagonalizes the inertial tensor. While the period of the flipping diverges as the initial conditions approach perfect mid-axis rotation [118] and the tennis racket flips of particles inside an ensemble with probabilistically distributed rotational states hence quickly average out to zero, Ma et al. found [118] that quantum tunneling between rotations in opposite directions may render the flips persistent given that the temperature is sufficiently low.
As we will discuss in further detail below, the quantization of angular momentum opens up a novel route towards high-mass interferometry [10]. In addition, several proposals have been put forward advocating levitated nanoparticles as ideal testbeds in the search for physics beyond the standard model [119] and even hinting at the possibility to utilize them as qubits [120]. While it is (as of now) at least doubtful that levitated mesoscopic objects offer any notable technological advantage over more established systems such as trapped ions [121] or superconducting qubits [122] in the field of quantum information processing, the experimental methods that have been and still need to be developed in order to conduct even proof-of-principle demonstrations will allow for some valuable insights into how the quantum world unfolds in settings that are closer to our intuitive perception of reality, for example in complex (bio-)molecules and ultimately perhaps even in living organisms [123].
In the present section, we will summarize a few of the existing proposals and experiments with the aim of providing a compelling argument for further research in this field.

5.1 Orientational Quantum Revivals

In view of our group's background, one of our main interests lies in the prospect of conducting interferometric experiments with rotational quantum states [10] in the foreseeable future. When a particle is initially prepared in a well-defined orientation and then released from its trapping potential to evolve freely, the wave packet disperses into a rotational superposition comprising (in the ideal case) all possible angular momentum states.
Given the system's initial state $|\psi(0)\rangle$ and Hamiltonian $\hat{H}$, which we assume to be time-independent, its state after some time t reads

$$|\psi(t)\rangle = e^{-i\hat{H}t/\hbar}\,|\psi(0)\rangle. \tag{5.1}$$

In the case of a quantized free rotor, we have $\hat{H} = \hat{L}^2/(2I)$, where $\hat{L}^2$ is the squared total angular momentum operator. Unlike the Hamiltonian of a harmonic oscillator, the free rotor Hamiltonian features unequally spaced eigenvalues $E_j = \hbar^2 j(j+1)/(2I)$, $j \in \{0, 1, 2, ...\}$. Assuming a perfectly well-defined initial orientation, $|\psi(0)\rangle$ is a balanced superposition when written in the angular momentum basis $\{|j\rangle\}$. We therefore get for $|\psi(t)\rangle$ the expression[1]

$$|\psi(t)\rangle \propto \sum_{j=0}^{\infty} e^{-i\frac{\hbar}{2I}j(j+1)t}\,|j\rangle. \tag{5.2}$$

This superposition eventually returns to the original localized state whenever $\hbar t/(2I)$ is an integer multiple of π, i.e. after integer multiples of the *revival time* τ,

$$\tau = \frac{2\pi I}{\hbar}. \tag{5.3}$$

Orientational quantum revivals constitute a direct test of angular momentum quantization in massive objects as they critically rely on the fact that the quantum number j can only take integer values.
Furthermore, this scheme does not require the particles to be prepared in a spatial superposition [8, 124], which is challenging to implement in practice. Near-field interferometry based on the Talbot effect [9], for example, would require flight times amounting to at least the Talbot time

$$\tau_{\mathsf{T}} = \frac{md^2}{2\pi\hbar}, \tag{5.4}$$

where d is the grating period. Inserting the expression for the moment of inertia of a solid sphere[2],

$$I_{\text{sphere}} = \frac{2}{5}mr^2, \tag{5.5}$$

into eq. (5.3), we observe that τ/τ_{T} scales with $(r/d)^2$. When the grating period of the Talbot interferometer is larger than about twice the particle diameter, we have $\tau < \tau_{\mathsf{T}}$. This is a significant advantage of the orientational revival approach because the shorter evolution time relaxes complications imposed by gravity – most notably the required height of the interferometer – and decoherence. Another valuable feature is the fact that it allows the same particle to be used again after each run. This is crucial due to the lack of loading mechanisms with high repetition rates and, in addition, prevents experimental errors caused by variations in the particle shape.

[1] We note that this state is not normalizable. This is because – for the sake of intuitiveness – we took the initial wave function to be infinitely sharply peaked in orientation space, which is not a physical assumption. For a proper treatment under realistic conditions, we refer the reader to ref. [10].

[2] This assumption is made for simplicity and because our particles would in the end only slightly deviate from a perfectly spherical shape.

The protocol [10] consists of an initial alignment stage, whereby the nanorotor is oriented by means of two counterpropagating linearly polarized laser beams, followed by a free evolution upon releasing the particle from the trap, detection of the orientational quantum revival by the light it scatters as a function of time around $t = \tau$, and switching the optical potential back on to repeat the experimental run.
For an (almost) spherical silica particle with a diameter of 50nm, which is roughly the size that we aim for in our cooling experiment, the revival time is on the order of seconds. An experimental realization hence does not seem entirely out of the question once the rotational degrees of freedom can be reliably cooled. However, in order to minimize the revival time (and hence the distance of free fall) and to facilitate the initial orientation, thin, light nanorods are probably best suited for this task.

5.2 Ultrasensitive Sensing

Considering the excellent isolation of optically levitated nanoparticles in ultra-high vacuum, their small mass (or moment of inertia) in comparison to macroscopic objects, the ability to couple their ro-translational motion to optical fields and their versatility in that they are responsive to various types of interactions, it does not come as a surprise that they have found application as ultrasensitive detectors of forces and torques. Ultimately, this could even allow to beat the standard quantum limit [125, 126], which bounds the product of measurement imprecision and backaction and may only be overcome using specially tailored states such as squeezed states [127] or involved noise-cancelling techniques like backaction evasion [128]. Still, even the most sophisticated approach will fail if thermal fluctuations, which constitute an independent and ever-present source of noise (cf. sec. 3.4), are not mitigated by cooling.
As hinted at previously, levitated nanosensors may even open the way to observe Casimir torques [114], the rotational analogue to the more extensively studied Casimir force, which arises as a consequence of vacuum fluctuations when an object is placed in close proximity to a surface [129]. In their paper, Xu and Li [114] propose to levitate a nanorod inside a linearly polarized tweezer near a birefringent plate. The Casimir torque is expected to change the particle's orientation provided that the long axis of the rod is neither parallel nor perpendicular to the plate's optic axis [114].
Experimentally, the rotational motion of a silicon nanorod has successfully been locked to an external clock [13]. The phase lag between the driving force and the rotation provides a direct measure of the external torque exerted on the test particle and the damping induced by collisions with gas molecules. The latter, in turn, is directly proportional to the pressure when the mean free path of the particles is large compared to the size of the object. The force sensitivities attained with optically levitated nanoparticles have improved significantly in a short period of time with state-of-the-art experiments now operating within zepto- [130] and even yoctonewton [131] ranges. At this level, it is already possible to measure the rate of heating caused by photons scattering off the probe particle [85]. This is a formidable task as the photonic recoil can only dominate over collisions with background gas in the limit of extremely strong isolation from the environment.

5.3 Search for Beyond-Standard Model Physics

Levitated nanoparticles have repeatedly been suggested as promising candidates in the search for beyond-standard model physics [119]. As the more traditional collision experiments become exceedingly demanding with increasing collision energy thresholds, improvements in the measurement sensitivity that enable the direct observation of tiny couplings gain further attraction. As alluded to in sec. 5.2, nanoparticles have the potential to serve this purpose.

Some of those detection schemes rely on narrow wavepackets and/or non-trivial quantum states, the preparation of which necessitates efficient cooling and control. This is the case, for example, in the proposed investigation of short-range gravitational forces by the shift of the interference fringes in a Talbot interferometer located in close proximity to a wall of varying density [132] or in the search for ultralight dark matter by its decohering effect on a spatial superposition of a massive object [133], where a broad distribution of motional states would degrade the visibility of the interference fringes.
In the future, it may be possible to extend the latter proposal to include (and potentially benefit from) rotational decoherence. More specifically, one of the biggest obstacles standing in the way of observing dark matter-induced decoherence is the expected rarity of collision events and the large mass of the test particle that is hence required. Preparing such particles in a spatial superposition is challenging, in particular if a large separation is required in order to operate within the short-wavelength limit (cf. sec. 3).
In the context of orientational superpositions, the relevant length parameter is not the delocalization distance but the dimensions of the particle itself, which can in principle be scaled up much more easily. Because larger particles tend to scatter preferentially in the forward direction, it may even be favorable to operate within the long-wavelength limit in the search for light dark matter. The short-wavelength limit would then still apply to collisions with ambient gas molecules because they are much more massive than the particles that one seeks to detect.
In the long-wavelength regime and assuming a spheroidal particle with two identical main axes such that $\alpha_1 = \alpha_2 \neq \alpha_3$, the decoherence rate is proportional to the squared sine of the angular distance between the respective orientations [66]. Observing such a dependence together with the right choice of particle size would allow to constrain the range of possible de Broglie wavelengths of the decoherence source. While this would, of course, not imply the presence of hitherto unknown types of matter and the experimental challenges still remain, it may constitute another way of characterizing the underlying process. It is also noteworthy that the ratio between the rotational and translational decoherence rates scales with the inverse of the mass of the colliding particle [134]. In view of the rivaling scattering of ambient gas, light dark matter may thus have a higher chance of decohering a rotational superposition than a spatial one.

Another proposed experiment seeks to reveal potential modifications to Newton's law of gravity by measuring the displacement of a cooled microsphere trapped inside an optical cavity close to an oscillating source mass of varying density behind a mirror surface [135]. While only spherical particles were originally considered, such a test might as well benefit from the consideration of rotational degrees of freedom via the torque an oscillating mass distribution exerts on the particle.
However, not only possible modifications to the inverse-square law but the nature of the gravitational force itself largely remains a mystery as a unifying theory of gravity and quantum mechanics does still not exist. This is (partly) due to the elusiveness of the graviton. An idea by Bose et al. [136] addresses the latter issue based on their argument that gravity is only able to generate entanglement if the force is mediated by a quantized field. Unfortunately, their proposal relies on the simultaneous creation of spatial superpositions of two micron-sized particles over distances on the order of 100µm [136], which is highly unlikely to be experimentally feasible in the near future.
Still, gravitational entanglement can not only be established between two spatial superpositions but potentially also between a translationally and a rotationally delocalized particle. In fact, as Carlesso et al. argue [137], even a single "quantum torsion balance" composed of two nanospheres that are connected by a rigid rod of negligible mass can serve to test the "quantumness" of gravity. To that end, the particle needs to be prepared in an orientational superposition state and one would detect the change in the separation angle after a sufficient time of free evolution. On the experimental side, silica nanodumbbells, which geometrically resemble the aforementioned

nanomechanical torsion balance, have successfully been synthesized, optically trapped and driven to GHz rotations [138].

5.4 Quantum Information Processing

The fact that quantum systems can exist in superposition states has ushered in a new era of information processing. Bearing in mind the linearity of the unitary operators that represent the time evolution of a closed quantum system, performing a single quantum operation on such a state is equivalent to applying a classical function to multiple inputs at once. This gives rise to a massive speed-up in certain computational tasks as compared to what a classical computer is able to achieve. Perhaps most famously, this is true for the problem of boson sampling [139].
The most basic non-trivial carriers of quantum information are two-dimensional systems, termed *qubits*. A profound discussion of the criteria a specific system needs to satisfy in order to make a suitable qubit for quantum information processing goes beyond the scope of thesis and may be found elsewhere [140]. We may, however, still ask ourselves whether levitated nanoparticles can in principle serve this purpose.
Indeed, Romero-Isart et al. [123] propose a protocol to create a phononic superposition of the type $|\psi\rangle = \frac{1}{\sqrt{2}}(|0\rangle + |1\rangle)$ by injecting a single-photon state into an optical cavity in which the particle is harmonically trapped and cooled to the ground state. The pulse can be tailored in such a way that the photonic and phononic excitations are swapped with a probability of 1/2, generating a maximally entangled state between the two systems. A balanced homodyne detection of the output mode then leaves the particle in a superposition of the ground and first excited state [123].
The question remains whether such systems are scalable and if (and how) it is possible to apply a universal set of quantum gates.
The latter requires a way to make the qubits interact with each other in a controlled and coherent manner and indeed, there has been progress on how to achieve that in multi-particle systems [141, 142]. Of particular importance in that regard are entangling gates, which are capable of generating non-classical correlations given *certain* input states. An example for such an operation is the CZ-gate, which is defined by the transformation $\mathrm{CZ}|i\rangle|j\rangle = (-1)^{ij}|i\rangle|j\rangle$, where $i, j \in \{0, 1\}$. The CZ-gate together with all single-qubit operations constitutes a universal set of gates for quantum computing [143]. Exploiting the optical binding [142] between particles in separate optical tweezers with individually tunable phases, it would be conceivable to implement a CZ-gate in a way similar to the Cirac-Zoller scheme [143]. Such a protocol would require cooling the center-of-mass normal mode of two coupled mechanical oscillators to the ground state and the ability to individually address the particles and excite their motional states.
It must be noted, however, that the energy levels of a quantum harmonic oscillator are not suitable as qubits because they are equally spaced and can hence not be individually addressed. Luckily, optical potentials are highly tunable, which permits the introduction of anharmonicities [144] that give rise to a more complex level structure. This will likewise affect the orientational degrees of freedom since, as we have seen in sec. 2.3, they also feel a harmonic potential generated by the trapping beam.
It is well-known that entanglement provides a valuable resource not only in the field of quantum computation, but also in quantum cryptography and communication. Different techniques have been suggested to create and certify entanglement with levitated nanoparticles. One promising idea is based on coherent scattering and requires only modest modifications from our current setup [40]: If two particles are trapped in separate tweezers, the power of which (and hence the respective mechanical frequencies) may be individually controlled, and the cavity is detuned by the average of those frequencies, the detection of a Stokes photon leaves the oscillators in a maximally entangled Bell state $|\Psi^+\rangle = \frac{1}{\sqrt{2}}(|01\rangle + |10\rangle)$, provided that both were initially prepared in the ground state. This technique would also allow to entangle different degrees of freedom pertaining to the same particle [40], but care needs to be taken as their couplings to

the light field exhibit a distinct dependence on the phase of the standing wave. On the other hand, the use of a single particle instead of two avoids issues associated with imperfections in their shape and mass. Entangling the rotational with the translational motion may eventually turn out to find intriguing applications as those are affected by distinct kinds of interactions and decoherence mechanisms.
A potentially more robust scheme [41], which does not require individual photon counting, subjects the particles to oppositely detuned tweezers and introduces additional dispersive coupling. This allows to cool down the joint Bogoliubov mode,

$$\hat{\beta} = \frac{1}{\sqrt{\lambda_1^2 + \lambda_2^2}} \left(\lambda_1 \hat{b}_1 + \lambda_2 \hat{b}_2^\dagger \right), \tag{5.6}$$

where $\lambda_{1,2}$ denote the optomechanical coupling rates of the respective particles, to the ground state and to generate a Gaussian entangled two-mode squeezed state [41] as certified by a violation of the Duan criterion of separability for continuous-variable systems [145],

$$\Delta^2(\hat{x}_1 + \hat{x}_2) + \Delta^2(\hat{p}_1 - \hat{p}_2) \geq 2. \tag{5.7}$$

While we have focused on optical means of preparing and manipulating the motional states of particles in the above discussion, this is not the only option. An all-electrical alternative [120], which comprises initial cooling as well as the generation of superpositions and entanglement, relies on the confinement of a charged nanoparticle in a quadrupole ion trap, which is coupled to a superconducting charge qubit via the charge induced on the endcaps by the particle's ro-translational motion. Preparing the superconducting qubit in a superposition of charge states [146] allows to entangle the mechanical motion with the qubit state [120].

Chapter 6

Conclusion and Outlook

The previous section hinted at the indisputable disparity between the multiple ideas and proposals that have been brought forward and the experimental progress to date. By acquainting ourselves with the theoretical framework, estimating the expected cooling efficiency for a range of parameters, demonstrating stable and semi-automated locking of a high-finesse cavity, detecting and trapping SiO_2 nanoparticles with diameters of 100 and 150nm in intermediate vacuum and measuring the motional PSD of the latter, we have laid the groundwork to further pursue our final goal and demonstrate cooling of a levitated nanoparticle in all ro-translational degrees of freedom. While this is a demanding task in its own right as we have experienced first hand, it would only pave the way for a profound examination of the "quantum behavior" of large particles.

Until then, we are still faced with a plethora of challenges. One of the most critical ones is trap loading. Ultimately, we would wish for a particle source that is reasonably simple to implement, versatile, clean, highly repetitive, reliable and compatible with high vacuum in combination with an optical trap. LIAD only satisfies the first two criteria and – to a very limited extent – the third. While we have shown the method to be in principle applicable for our purpose, cf. sec. 4.1.1, there is ample room for improvement. Optimizing the current source and testing new ones will thus become a top priority.
Advancing our current detection capabilities will also be at the forefront of our efforts. We are very optimistic that the interferometrically enhanced detection of either forward or backward scattered light as discussed in sec. 4.1.4 will allow us to further improve our sensitivity and facilitate the observation of spectrally resolved peaks in the power spectral densities pertaining to both translational and rotational degrees of freedom.
At a later stage in our experiment, we will also need to gain a better understanding of the various decoherence sources that might stand in the way of observing genuine quantum phenomena. We have already said in sec. 3 that we expect thermal decoherence to be one of the most difficult to overcome as it requires us to minimize the absorption and emission of blackbody radiation.

The latter point is obviously closely related to the particle's internal temperature. A more mundane reason for which we need to limit internal heating is the possible disintegration of our particles. As alluded to in sec. 4.1.2, melting is a potential concern even for our nominally transparent SiO_2 spheres. This will become all the more serious as we aim to extend our research towards controlling the ro-translational motion of complex biological entities such as viruses or bacteriophages.
Indeed, while those tend to be less massive than the nanoparticles that we are currently looking into[1], seemingly in contradiction with the endeavor pursued by large parts of the community to demonstrate quantum phenomena at ever-increasing mass scales, there are several reasons why it is worthwhile to study them nonetheless. Firstly, there is obviously a philosophical appeal to the notion of biologically active systems, perhaps one day even living organisms, appearing in a

[1]This is just a rule of thumb, which does not apply to all species. There are viruses containing hundreds of kilobase pairs [147], corresponding to dimensions of several hundreds of nm.

quantum superposition state. However, even on a more pragmatic note, particle masses on the order of 10^6amu would correspond to orientational revival times on the order of ms, cf. eq. (5.3), thus easing complications associated with gravitational free-fall. In addition, quantum-enhanced sensing, for example in the form of single-photon recoil spectroscopy [148], may reveal biologically relevant properties of the particles in the absence of any surrounding medium that may perturb them.
While the coherent scattering technique is in principle very general in that it does not rely on any specific intrinsic property of the particles other than their polarizability, the potential fragility of biological specimens may render it unavoidable to shield them from direct irradiation with intense laser light. In that case, the concept of sympathetic cooling [149] may come to the rescue. This would require an ion trap, which is yet another update to our current setup that we are planning to incorporate in the intermediate term. Even if sympathetic cooling is not required (or, indeed, possible), their comparatively large trapping regions [108] will facilitate capturing particles at lower pressures, ideally even in ultra-high vacuum if temporal control is applied [98]. It is hence not a surprise that hybrid traps [150], which combine the benefits of both optical and electrodynamic trapping potentials, become increasingly attractive.
On the other hand, a smaller particle mass goes along with a reduced optomechanical coupling, cf. eq. (2.56), which must be counteracted by decreasing the cavity mode volume. This will require us to employ microfabricated cavities [37].

In this outlook, we have deliberately outlined two paths to proceed that appear rather distinct at first glance. However, as we have argued, there are plenty of synergies to benefit from. While ground-state cooling of a tailored nanoparticle remains a desirable goal for us, we would like our setup to eventually provide a general framework for further studies, allowing us to pursue a top-down approach in mass, but a bottom-up approach in structural complexity.

But what would we expect to find out? After all, there has not been any evidence of quantum physics breaking down at any point so far and the notion of biologically active complexes to follow (to whatever extent) different laws of nature than "dead matter" seems rather preposterous. Still, it is an essential part of our jobs as (aspiring) scientists to not take anything for granted, to remain curious and to continuously challenge the way we perceive things to work. In this spirit, I will not conclude by making an excessively bold promise, nor by attempting one last time to convince the reader of the significance of our work, but by making a plea to both the scientific community and the public to appreciate not only the great discoveries that have shaken our world view, but to some degree also the tiny surprises and yes, even the failures along the way that not rarely have ultimately led to breakthroughs in the first place.

Bibliography

1. Stenger, V. J. Quantum quackery. *The Skeptical Inquirer* **21**(1), 37–40 (1997).
2. Brezger, B. *et al.* Matter-wave interferometer for large molecules. *Physical Review Letters* **88**(10), 100404. arXiv: quant-ph/0202158 (2002).
3. Fein, Y. Y. *et al.* Quantum superposition of molecules beyond 25 kDa. *Nature Physics* **15**(12), 1242–1245 (2019).
4. Toroš, M., Gasbarri, G. & Bassi, A. Colored and dissipative continuous spontaneous localization model and bounds from matter-wave interferometry. *Physics Letters, Section A: General, Atomic and Solid State Physics* **381**(47), 3921–3927. arXiv: 1601.03672 (2017).
5. Bahrami, M., Paternostro, M., Bassi, A. & Ulbricht, H. Proposal for a noninterferometric test of collapse models in optomechanical systems. *Physical Review Letters* **112**(21), 210404. arXiv: 1402.5421v2 (2014).
6. Vinante, A. *et al.* Upper bounds on spontaneous wave-function collapse models using millikelvin-cooled nanocantilevers. *Physical Review Letters* **116**(9), 090402. arXiv: 1510.05791 (2016).
7. Carlesso, M., Paternostro, M., Ulbricht, H., Vinante, A. & Bassi, A. Non-interferometric test of the continuous spontaneous localization model based on rotational optomechanics. *New Journal of Physics* **20**(8), 083022. arXiv: 1708.04812 (2018).
8. Yin, Z. Q., Li, T., Zhang, X. & Duan, L. M. Large quantum superpositions of a levitated nanodiamond through spin-optomechanical coupling. *Physical Review A - Atomic, Molecular, and Optical Physics* **88**(3), 033614. arXiv: 1305.1701 (2013).
9. Bateman, J., Nimmrichter, S., Hornberger, K. & Ulbricht, H. Near-field interferometry of a free-falling nanoparticle from a point-like source. *Nature Communications* **5,** 4788. arXiv: 1312.0500 (2014).
10. Stickler, B. A. *et al.* Probing macroscopic quantum superpositions with nanorotors. *New Journal of Physics* **20,** 122001. arXiv: 1803.01778 (2018).
11. Weiss, T., Roda-Llordes, M., Torrontegui, E., Aspelmeyer, M. & Romero-Isart, O. Large quantum delocalization of a levitated nanoparticle using optimal control: Applications for force sensing and entangling via weak forces. *Physical Review Letters* **127**(2), 023601. arXiv: 2012.12260 (2021).
12. Tebbenjohanns, F., Mattana, M. L., Rossi, M., Frimmer, M. & Novotny, L. Quantum control of a nanoparticle optically levitated in cryogenic free space. *Nature* **595**(7867), 378–382. arXiv: 2103.03853 (2021).
13. Kuhn, S. *et al.* Optically driven ultra-stable nanomechanical rotor. *Nature Communications* **8,** 1670. arXiv: 1702.07565 (2017).
14. Dania, L., Bykov, D. S., Knoll, M., Mestres, P. & Northup, T. E. Optical and electrical feedback cooling of a silica nanoparticle levitated in a Paul trap. *Physical Review Research* **3**(1), 013018. arXiv: 2007.04434 (2021).

15. Hofer, J. *et al.* High-Q magnetic levitation and control of superconducting microspheres at millikelvin temperatures. [Preprint]. arXiv: 2211.06289 (2022).

16. Thalhammer, G. *et al.* Combined acoustic and optical trapping. *Biomedical Optics Express* **2**(10), 2859 (2011).

17. Kamba, M., Kiuchi, H., Yotsuya, T. & Aikawa, K. Recoil-limited feedback cooling of single nanoparticles near the ground state in an optical lattice. *Physical Review A* **103**(5), L051701. arXiv: 2011.12507 (2021).

18. Pontin, A., Fu, H., Toroš, M., Monteiro, T. S. & Barker, P. F. Simultaneous cooling of all six degrees of freedom of an optically levitated nanoparticle by elliptic coherent scattering. *Nature Physics* [in press]. arXiv: 2205.10193 (2023).

19. Delić, U. *et al.* Cooling of a levitated nanoparticle to the motional quantum ground state. *Science* **367**(6480), 892–895 (2020).

20. Piotrowski, J. *et al.* Simultaneous ground-state cooling of two mechanical modes of a levitated nanoparticle. *Nature Physics* [in press]. arXiv: 2209.15326 (2023).

21. Wineland, D. J., Drullinger, R. E. & Walls, F. L. Radiation-pressure cooling of bound resonant absorbers. *Physical Review Letters* **40**(25), 1639–1642 (1978).

22. Lett, P. D. *et al.* Observation of atoms laser cooled below the doppler limit. *Physical Review Letters* **61**(2), 169–172 (1988).

23. Salomon, C., Dalibard, J., Phillips, W. D., Clairon, A. & Guellati, S. Laser cooling of cesium atoms below 3μK. *Europhysics Letters* **12**(8), 683–688 (1990).

24. Kasevich, M. & Chu, S. Laser cooling below a photon recoil with three-level atoms. *Physical Review Letters* **69**(12), 1741–1744 (1992).

25. Gieseler, J., Deutsch, B., Quidant, R. & Novotny, L. Subkelvin parametric feedback cooling of a laser-trapped nanoparticle. *Physical Review Letters* **109**(10), 103603. arXiv: 1202.6435 (2012).

26. Tebbenjohanns, F., Frimmer, M., Militaru, A., Jain, V. & Novotny, L. Cold damping of an optically levitated nanoparticle to micro-Kelvin temperatures. *Physical Review Letters* **122**(22), 223601. arXiv: 1812.09875 (2019).

27. Vijayan, J. *et al.* Scalable all-optical cold damping of levitated nanoparticles. *Nature Nanotechnology* **18,** 49–54. arXiv: 2205.04455 (2023).

28. Vovrosh, J. Parametric feedback cooling and squeezing of optically levitated particles. PhD thesis. University of Southampton (2018).

29. Asenbaum, P., Kuhn, S., Nimmrichter, S., Sezer, U. & Arndt, M. Cavity cooling of free silicon nanoparticles in high vacuum. *Nature Communications* **4,** 2743. arXiv: 1306.4617 (2013).

30. Horak, P., Hechenblaikner, G., Gheri, K. M., Stecher, H. & Ritsch, H. Cavity-induced atom cooling in the strong coupling regime. *Physical Review Letters* **79**(25), 4974–4977 (1997).

31. Maunz, P. *et al.* Cavity cooling of a single atom. *Nature* **428,** 50–52 (2004).

32. Kuhn, S. *et al.* Full rotational control of levitated silicon nanorods. *Optica* **4**(3), 356–360. arXiv: 1608.07315 (2017).

33. Vuletić, V. & Chu, S. Laser cooling of atoms, ions, or molecules by coherent scattering. *Physical Review Letters* **84**(17), 3787–3790 (2000).

34. Delić, U. Cavity cooling by coherent scattering of a levitated nanosphere in vacuum. PhD thesis. University of Vienna (2019).

35. Delić, U. *et al.* Cavity cooling of a levitated nanosphere by coherent scattering. *Physical Review Letters* **122**(12), 123602. arXiv: 1812.09358 (2019).

36. Windey, D. *et al.* Cavity-based 3D cooling of a levitated nanoparticle via coherent scattering. *Physical Review Letters* **122**(12), 123601. arXiv: 1812.09176 (2019).

37. Wachter, G. *et al.* Silicon microcavity arrays with open access and a finesse of half a million. *Light: Science and Applications* **8,** 37. arXiv: 1904.01106 (2019).

38. Ojanen, T. & Børkje, K. Ground-state cooling of mechanical motion in the unresolved sideband regime by use of optomechanically induced transparency. *Physical Review A - Atomic, Molecular, and Optical Physics* **90**(1), 013824. arXiv: 1402.6929 (2014).

39. Mansouri, D., Rezaie, B., Ranjbar, A. N. & Daeichian, A. Cavity-assisted coherent feedback cooling of a mechanical resonator to the ground-state in the unresolved sideband regime. *Journal of Physics B: Atomic, Molecular and Optical Physics* **55**(16), 165501 (2022).

40. Rudolph, H., Hornberger, K. & Stickler, B. A. Entangling levitated nanoparticles by coherent scattering. *Physical Review A* **101**(1), 011804. arXiv: 2001.05769 (2020).

41. Chauhan, A. K., Černotík, O. & Filip, R. Stationary Gaussian entanglement between levitated nanoparticles. *New Journal of Physics* **22**(12), 123021. arXiv: 2006.03342 (2020).

42. Loudon, R. The quantum theory of light. 3rd edition. Oxford University Press, Oxford (2000).

43. Milonni, P. W. & Eberly, J. H. Laser physics. Wiley, Hoboken, NJ (2010).

44. Coffey, W. T. & Kalmykov, Y. P. The Langevin equation: With applications to stochastic problems in physics, chemistry and electrical engineering. 3rd edition. In: *World Scientific Series in Contemporary Chemical Physics* **27**. World Scientific, Singapore (2012).

45. Bowen, W. P. & Milburn, G. J. Quantum optomechanics. CRC Press, Boca Raton, FL (2016).

46. Gea-Banacloche, J. Emergence of classical radiation fields through decoherence in the Scully-Lamb laser model. *Foundations of Physics* **28**(4), 531–548 (1998).

47. Sakurai, J. J. & Napolitano, J. Modern quantum mechanics. Cambridge University Press, Cambridge (2020).

48. Jackson, J. D. Klassische Elektrodynamik. 5th edition. Edited by: Diestelhorst, M., Müller, K. & Witte, C. In: *De Gruyter Studium*. De Gruyter, Berlin (2014).

49. Grimm, R., Weidemüller, M. & Ovchinnikov, Y. B. Optical dipole traps for neutral atoms. In: *Advances In Atomic, Molecular, and Optical Physics* **42**, 95–170. Edited by: Bederson, B. & Walther, H. B. T. Academic Press, San Diego, CA (2000).

50. Meystre, P. Quantum optics: Taming the quantum. In: *Graduate Texts in Physics*. Springer International Publishing, Cham (2021).

51. Van de Hulst, H. C. Light scattering by small particles. Dover Publications, New York, NY (1981).

52. Purcell, E. M. Spontaneous emission probabilities at radio frequencies. *Physical Review* **69**(11-12), 681 (1946).

53. Vuletić, V., Chan, H. W. & Black, A. T. Three-dimensional cavity Doppler cooling and cavity sideband cooling by coherent scattering. *Physical Review A. Atomic, Molecular, and Optical Physics* **64**(3), 033405 (2001).

54. Gardiner, C. W. & Collett, M. J. Input and output in damped quantum systems: Quantum stochastic differential equations and the master equation. *Physical Review A* **31**(6), 3761–3774 (1985).

55. Schäfer, J., Rudolph, H., Hornberger, K. & Stickler, B. A. Cooling nanorotors by elliptic coherent scattering. *Physical Review Letters* **126**(16), 163603. arXiv: 2006.04090 (2021).

56. Van der Laan, F. Rotational Levitodynamics. PhD thesis. ETH Zürich (2022).

57. Cline, D. Variational Principles in Classical Mechanics. 3rd edition. University of Rochester River Campus Libraries, Rochester, NY (2021).

58. Rudolph, H., Schäfer, J., Stickler, B. A. & Hornberger, K. Theory of nanoparticle cooling by elliptic coherent scattering. *Physical Review A* **103**(4), 043514. arXiv: 2104.13134 (2021).

59. Joos, E. Decoherence through interaction with the environment. In: *Decoherence and the appearance of a classical world in quantum theory*, 35–136. Edited by: Giulini, D. *et al.* Springer, Berlin Heidelberg (1996).

60. Schlosshauer, M. Decoherence: And the quantum-to-classical transition. In: *The Frontiers Collection*. Springer, Berlin Heidelberg (2007).

61. Nimmrichter, S., Hammerer, K., Asenbaum, P., Ritsch, H. & Arndt, M. Master equation for the motion of a polarizable particle in a multimode cavity. *New Journal of Physics* **12,** 083003. arXiv: 1004.0807 (2010).

62. Hornberger, K. Introduction to decoherence theory. *Lecture Notes in Physics* **768,** 221–276. arXiv: quant-ph/0612118 (2009).

63. Hornberger, K. & Vacchini, B. Monitoring derivation of the quantum linear Boltzmann equation. *Physical Review A - Atomic, Molecular, and Optical Physics* **77**(2), 022112. arXiv: 0711.3109 (2008).

64. Hornberger, K. Master equation for a quantum particle in a gas. *Physical Review Letters* **97**(6), 060601. arXiv: quant-ph/0607085 (2006).

65. Stickler, B. A., Papendell, B. & Hornberger, K. Spatio-orientational decoherence of nanoparticles. *Physical Review A* **94**(3), 033828. arXiv: 1607.04508 (2016).

66. Zhong, C. & Robicheaux, F. Decoherence of rotational degrees of freedom. *Physical Review A* **94**(5), 052109. arXiv: 1605.03160 (2016).

67. Nimmrichter, S. Macroscopic matter-wave interferometry. PhD thesis. University of Vienna (2013).

68. Hackermüller, L., Hornberger, K., Brezger, B., Zeilinger, A. & Arndt, M. Decoherence of matter waves by thermal emission of radiation. *Nature* **427,** 711–714. arXiv: quant-ph/0402146 (2004).

69. Kim, H., Han, M.-S., Perello, D. & Yun, M. Effective temperature of thermal radiation from non-uniform temperature distributions and nanoparticles. *Infrared Physics and Technology* **60,** 7–9 (2013).

70. Millen, J., Deesuwan, T., Barker, P. & Anders, J. Nanoscale temperature measurements using non-equilibrium Brownian dynamics of a levitated nanosphere. *Nature Nanotechnology* **9,** 425–429. arXiv: 1309.3990 (2014).

71. Gieseler, J. *et al.* Optical tweezers: A comprehensive tutorial from calibration to applications. *Advances in Optics and Photonics* **13**(1), 74–241. arXiv: 2004.05246 (2021).

72. Meystre, P & Sargent, M. Elements of quantum optics. 4th edition. Springer, Berlin Heidelberg (2007).

73. Safavi-Naeini, A. H. *et al.* Laser noise in cavity-optomechanical cooling and thermometry. *New Journal of Physics* **15,** 035007. arXiv: 1210.2671 (2013).

74. Gardiner, C. & Zoller, P. Quantum noise: A handbook of Markovian and non-Markovian quantum stochastic methods with applications to quantum optics. 2nd edition. In: *Springer Series in Synergetics*. Springer, Berlin Heidelberg (2020).

75. Halbritter, J. Torque on a rotating ellipsoid in a rarefied gas. *Zeitschrift für Naturforschung - Section A Journal of Physical Sciences* **29**(12), 1717–1722 (1974).

76. Gieseler, J. Dynamics of optically levitated nanoparticles in high vacuum. PhD thesis. The Institute of Photonic Sciences, Castelldefels (2014).

77. Hauer, B. D., Maciejko, J. & Davis, J. P. Nonlinear power spectral densities for the harmonic oscillator. *Annals of Physics* **361,** 148–183. arXiv: 1502.02372 (2015).

78. Clerk, A. A., Devoret, M. H., Girvin, S. M., Marquardt, F. & Schoelkopf, R. J. Introduction to quantum noise, measurement, and amplification. *Reviews of Modern Physics* **82**(2), 1155–1208. arXiv: 0810.4729 (2010).

79. Ganta, D., Dale, E. B., Rezac, J. P. & Rosenberger, A. T. Optical method for measuring thermal accommodation coefficients using a whispering-gallery microresonator. *Journal of Chemical Physics* **135**(8), 084313 (2011).

80. Martinetz, L., Hornberger, K. & Stickler, B. A. Gas-induced friction and diffusion of rigid rotors. *Physical Review E* **97**(5), 052112. arXiv: 1802.08302 (2018).

81. Diósi, L. Laser linewidth hazard in optomechanical cooling. *Physical Review A - Atomic, Molecular, and Optical Physics* **78**(2), 021801. arXiv: 0803.3760 (2008).

82. Franz, J. H. & Jain, V. K. Optical communications: Components and systems: Analysis–design–optimization–application. CRC Press, Boca Raton, FL (2000).

83. Rabl, P., Genes, C., Hammerer, K. & Aspelmeyer, M. Phase-noise induced limitations on cooling and coherent evolution in optomechanical systems. *Physical Review A - Atomic, Molecular, and Optical Physics* **80**(6), 063819. arXiv: 0903.1637 (2009).

84. Meyer, N. *et al.* Resolved-sideband cooling of a levitated nanoparticle in the presence of laser phase noise. *Physical Review Letters* **123**(15), 153601. arXiv: 1907.02741 (2019).

85. Jain, V. *et al.* Direct measurement of photon recoil from a levitated nanoparticle. *Physical Review Letters* **116**(24), 243601. arXiv: 1603.03420 (2016).

86. Gonzalez-Ballestero, C. *et al.* Theory for cavity cooling of levitated nanoparticles via coherent scattering: Master equation approach. *Physical Review A - Atomic, Molecular, and Optical Physics* **100**(1), 013805. arXiv: 1902.01282 (2019).

87. Summers, M. D., Burnham, D. R. & McGloin, D. Trapping solid aerosols with optical tweezers: A comparison between gas and liquid phase optical traps. *Optics Express* **16**(11), 7739–7747 (2008).

88. Nikkhou, M., Hu, Y., Sabin, J. A. & Millen, J. Direct and clean loading of nanoparticles into optical traps at millibar pressures. *Photonics* **8**(11), 458. arXiv: 2109.10316 (2021).

89. Khodaee, A., Dare, K., Johnson, A., Delić, U. & Aspelmeyer, M. Dry launching of silica nanoparticles in vacuum. *AIP Advances* **12**(12), 125023. arXiv: 2209.00482 (2022).

90. Rieser, J. Towards optical levitation in UHV: Loading using hollow-core photonic crystal fibers. Master's thesis. University of Vienna (2020).

91. Fenn, J. B., Mann, M., Meng, C. K., Wong, S. F. & Whitehouse, C. M. Electrospray ionization for mass spectrometry of large biomolecules. *Science* **246**(4926), 64–71 (1989).

92. Howder, C. R., Bell, D. M. & Anderson, S. L. Optically detected, single nanoparticle mass spectrometer with pre-filtered electrospray nanoparticle source. *Review of Scientific Instruments* **85**(1), 014104 (2014).

93. Kooij, S., Astefanei, A., Corthals, G. L. & Bonn, D. Size distributions of droplets produced by ultrasonic nebulizers. *Scientific Reports* **9,** 6128 (2019).

94. Huang, Z., Horke, D. & Küpper, J. Laser-induced acoustic desorption of thermally stable and unstable biomolecules. [Preprint]. arXiv: 1811.05925v1 (2018).

95. Sezer, U. *et al.* Laser-induced acoustic desorption of natural and functionalized biochromophores. *Analytical Chemistry* **87**(11), 5614–5619 (2015).

96. Peng, W.-P. *et al.* Laser-induced acoustic desorption mass spectrometry of single bioparticles. *Angewandte Chemie - International Edition* **45**(9), 1423–1426 (2006).

97. Huang, Z. *et al.* Development and characterization of a laser-induced acoustic desorption source. *Analytical Chemistry* **90**(6), 3920–3927. arXiv: 1710.06684 (2018).

98. Bykov, D. S., Mestres, P., Dania, L., Schmöger, L. & Northup, T. E. Direct loading of nanoparticles under high vacuum into a Paul trap for levitodynamical experiments. *Applied Physics Letters* **115**(3), 034101. arXiv: 1905.04204 (2019).

99. Frimmer, M. *et al.* Controlling the net charge on a nanoparticle optically levitated in vacuum. *Physical Review A - Atomic, Molecular, and Optical Physics* **95**(6), 061801. arXiv: 1704.00169 (2017).

100. Ashkin, A, Dziedzic, J. M., Bjorkholm, J. E. & Chu, S. Observation of a single-beam gradient force optical trap for dielectric particles. *Optics Letters* **11**(5), 288–290 (1986).

101. Ranjit, G., Atherton, D. P., Stutz, J. H., Cunningham, M. & Geraci, A. A. Attonewton force detection using microspheres in a dual-beam optical trap in high vacuum. *Physical Review A - Atomic, Molecular, and Optical Physics* **91**(5), 051805. arXiv: 1503.08799 (2015).

102. Monteiro, F. *et al.* Force and acceleration sensing with optically levitated nanogram masses at microkelvin temperatures. *Physical Review A - Atomic, Molecular, and Optical Physics* **101**(5), 053835. arXiv: 2001.10931 (2020).

103. Ashkin, A. & Dziedzic, J. M. Optical levitation in high vacuum. *Applied Physics Letters* **28**(6), 333–335 (1976).

104. Jin, Y. *et al.* 6 GHz hyperfast rotation of an optically levitated nanoparticle in vacuum. *Photonics Research* **9**(7), 1344–1350. arXiv: 2012.09693 (2021).

105. Fox, R. W., Oates, C. W. & Hollberg, L. W. Stabilizing diode lasers to high-finesse cavities. In: *Experimental Methods in the Physical Sciences* **40**, 1–46. (2003).

106. Neuhaus, R. Toptica: Diode laser control electronics diode laser locking and linewidth narrowing. Online. URL: https://www.toptica.com/fileadmin/Editors_English/03_products/11_Isolators_Photonicals/02_photonicals/toptica_Laser_Locking_and_Linewidth_Narrowing.pdf. Accessed on 02 June 2023.

107. Black, E. D. An introduction to Pound–Drever–Hall laser frequency stabilization. *American Journal of Physics* **69**(1), 79–87 (2001).

108. Dania, L. *et al.* Position measurement of a levitated nanoparticle via interference with its mirror image. *Physical Review Letters* **129**(1), 013601. arXiv: 2112.14990 (2022).

109. Penny, T. W., Pontin, A. & Barker, P. F. Performance and limits of feedback cooling methods for levitated oscillators. A direct comparison. *Physical Review A - Atomic, Molecular, and Optical Physics* **104**(2), 023502. arXiv: 2102.01060 (2021).

110. Bennett, C. A. Principles of physical optics. 2nd edition. Wiley, Hoboken, NJ (2022).

111. Stickler, B. A., Hornberger, K. & Kim, M. S. Quantum rotations of nanoparticles. *Nature Reviews Physics* **3,** 589–597. arXiv: 2102.00992 (2021).

112. Ahn, J. *et al.* Ultrasensitive torque detection with an optically levitated nanorotor. *Nature Nanotechnology* **15,** 89–93. arXiv: 1908.03453 (2020).

113. Van der Laan, F. *et al.* Optically levitated rotor at its thermal limit of frequency stability. *Physical Review A - Atomic, Molecular, and Optical Physics* **102**(1), 013505. arXiv: 2003.10812 (2020).

114. Xu, Z. & Li, T. Detecting Casimir torque with an optically levitated nanorod. *Physical Review A - Atomic, Molecular, and Optical Physics* **96**(3), 033843. arXiv: 1704.08770 (2017).

115. Manjavacas, A. & García de Abajo, F. J. Vacuum friction in rotating particles. *Physical Review Letters* **105**(11), 113601. arXiv: 1009.4107 (2010).

116. Zhao, R., Manjavacas, A., García de Abajo, F. J. & Pendry, J. B. Rotational quantum friction. *Physical Review Letters* **109**(12), 123604. arXiv: 1208.4232 (2012).

117. Rashid, M., Toroš, M., Setter, A. & Ulbricht, H. Precession motion in levitated optomechanics. *Physical Review Letters* **121**(25), 1–10. arXiv: 1805.08042 (2018).

118. Ma, Y., Khosla, K. E., Stickler, B. A. & Kim, M. S. Quantum persistent tennis racket dynamics of nanorotors. *Physical Review Letters* **125**(5), 053604. arXiv: 2007.10065 (2020).

119. Moore, D. C. & Geraci, A. A. Searching for new physics using optically levitated sensors. *Quantum Science and Technology* **6**(1), 014008. arXiv: 2008.13197 (2021).

120. Martinetz, L., Hornberger, K., Millen, J., Kim, M. S. & Stickler, B. A. Quantum electromechanics with levitated nanoparticles. *npj Quantum Information* **6,** 101. arXiv: 2005.14006 (2020).

121. Häffner, H., Roos, C. F. & Blatt, R. Quantum computing with trapped ions. *Physics Reports* **469**(4), 155–203. arXiv: 0809.4368 (2008).

122. You, J. Q. & Nori, F. Superconducting circuits and quantum information. *Physics Today* **58**(11), 42–47. arXiv: quant-ph/0601121 (2005).

123. Romero-Isart, O., Juan, M. L., Quidant, R. & Cirac, J. I. Toward quantum superposition of living organisms. *New Journal of Physics* **12**(3), 033015. arXiv: 0909.1469 (2010).

124. Romero-Isart, O. *et al.* Large quantum superpositions and interference of massive nanometer-sized objects. *Physical Review Letters* **107**(2), 020405. arXiv: 1103.4081 (2011).

125. Kim, P. H., Hauer, B. D., Doolin, C., Souris, F. & Davis, J. P. Approaching the standard quantum limit of mechanical torque sensing. *Nature Communications* **7,** 13165. arXiv: 1607.00069 (2016).

126. Mason, D., Chen, J., Rossi, M., Tsaturyan, Y. & Schliesser, A. Continuous force and displacement measurement below the standard quantum limit. *Nature Physics* **15,** 745–749. arXiv: 1809.10629 (2019).

127. Xiao, M., Wu, L.-A. & Kimble, H. J. Precision measurement beyond the shot-noise limit. *Physical Review Letters* **59**(3), 278–281 (1987).

128. Clerk, A. A., Marquardt, F. & Jacobs, K. Back-action evasion and squeezing of a mechanical resonator using a cavity detector. *New Journal of Physics* **10,** 095010. arXiv: 0802.1842 (2008).

129. Casimir, H. On the attraction between two perfectly conducting plates. *Proceedings of the Koninklijke Nederlandse Akademie van Wetenschappen* **51,** 793–795 (1948).

130. Ranjit, G., Cunningham, M., Casey, K. & Geraci, A. A. Zeptonewton force sensing with nanospheres in an optical lattice. *Physical Review A - Atomic, Molecular, and Optical Physics* **93**(5), 053801. arXiv: 1603.02122 (2016).

131. Liang, T. *et al.* Yoctonewton force detection based on optically levitated oscillator. *Fundamental Research* **3**(1), 57–62 (2023).

132. Geraci, A. & Goldman, H. Sensing short range forces with a nanosphere matter-wave interferometer. *Physical Review D - Particles, Fields, Gravitation and Cosmology* **92**(6), 062002. arXiv: 1412.4482 (2015).

133. Riedel, C. J. Direct detection of classically undetectable dark matter through quantum decoherence. *Physical Review D - Particles, Fields, Gravitation and Cosmology* **88**(11), 116005. arXiv: 1212.3061 (2013).

134. Carlesso, M., Naeij, H. R. & Bassi, A. Perturbative algorithm for rotational decoherence. *Physical Review A - Atomic, Molecular, and Optical Physics* **103**(3), 032220. arXiv: 1912.08159 (2021).

135. Geraci, A. A., Papp, S. B. & Kitching, J. Short-range force detection using optically cooled levitated microspheres. *Physical Review Letters* **105**(10), 101101. arXiv: 1006.0261 (2010).

136. Bose, S. *et al.* Spin entanglement witness for quantum gravity. *Physical Review Letters* **119**(24), 240401. arXiv: 1707.06050 (2017).

137. Carlesso, M., Paternostro, M., Ulbricht, H. & Bassi, A. When Cavendish meets Feynman: A quantum torsion balance for testing the quantumness of gravity. [Preprint]. arXiv: 1710.08695 (2017).

138. Ahn, J. *et al.* Optically levitated nanodumbbell torsion balance and GHz nanomechanical rotor. *Physical Review Letters* **121**(3), 033603. arXiv: 1804.06570 (2018).

139. Tillmann, M. *et al.* Experimental boson sampling. *Nature Photonics* **7,** 540–544. arXiv: 1212.2240 (2013).

140. DiVincenzo, D. P. The physical implementation of quantum computation. *Fortschritte der Physik* **48**(9-11), 771–783. arXiv: quant-ph/0002077 (2000).

141. Arita, Y., Wright, E. M. & Dholakia, K. Optical binding of two cooled micro-gyroscopes levitated in vacuum. *Optica* **5**(8), 910–917 (2018).

142. Rieser, J. *et al.* Tunable light-induced dipole-dipole interaction between optically levitated nanoparticles. *Science* **377**(6609), 987–990. arXiv: arXiv:2203.04198v2 (2022).

143. Cirac, J. I. & Zoller, P. Quantum computations with cold trapped ions. *Physical Review Letters* **74**(20), 4091–4094 (1995).

144. Ciampini, M. A. *et al.* Experimental nonequilibrium memory erasure beyond Landauer's bound. [Preprint]. arXiv: 2107.04429 (2021).

145. Duan, L.-M., Giedke, G., Cirac, J. I. & Zoller, P. Inseparability criterion for continuous variable systems. *Physical Review Letters* **84**(12), 2722–2725 (2000).

146. Bouchiat, V., Vion, D., Joyez, P., Esteve, D. & Devoret, M. H. Quantum coherence with a single cooper pair. *Physica Scripta* **T76,** 165–170 (1998).

147. National Center for Biotechnology Information (NCBI). Bethesda (MD): National Library of Medicine (US), National Center for Biotechnology Information. 1988. Online. URL: https://www.ncbi.nlm.nih.gov/labs/virus/. Accessed on 02 June 2023.

148. Nimmrichter, S., Hornberger, K., Ulbricht, H. & Arndt, M. Absolute absorption spectroscopy based on molecule interferometry. *Physical Review A - Atomic, Molecular, and Optical Physics* **78**(6), 063607. arXiv: 0811.1141 (2008).

149. Bykov, D. S., Dania, L., Goschin, F. & Northup, T. E. 3D sympathetic cooling and detection of levitated nanoparticles. *Optica* **10**(4), 438–442. arXiv: 2210.07583 (2023).

150. Conangla, G. P., Rica, R. A. & Quidant, R. Extending vacuum trapping to absorbing objects with hybrid Paul-optical traps. *Nano Letters* **20**(8), 6018–6023. arXiv: 2005.05486 (2020).